

**ELECTRODE EFFECTS ON ELECTRON EMISSION AND GAS
BREAKDOWN FROM NANO TO MICROSCALE**

by

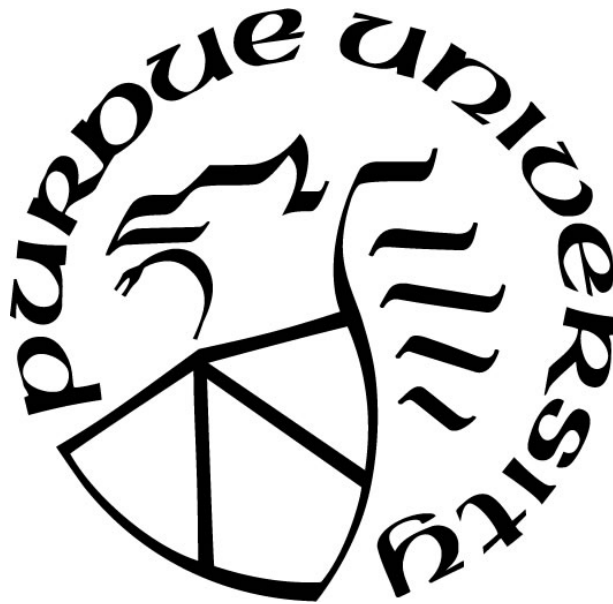
Russell Scott Brayfield II

A Dissertation

Submitted to the Faculty of Purdue University

In Partial Fulfillment of the Requirements for the degree of

Doctor of Philosophy



School of Agricultural and Biological Engineering

West Lafayette, Indiana

August 2020

**THE PURDUE UNIVERSITY GRADUATE SCHOOL
STATEMENT OF COMMITTEE APPROVAL**

Dr. Allen Garner, Chair

School of Nuclear Engineering

Dr. Sally P. Bane

School of Aeronautics and Astronautics

Dr. Robert S. Bean

School of Nuclear Engineering

Dr. Bernard Y. Tao

School of Agricultural and Biological Engineering

Approved by:

Dr. Nathen S. Mosier

Dedicated to my family, friends, and mentors who have supported me through all the trials that have come to pass, without whom this would not be possible.

ACKNOWLEDGMENTS

We gratefully acknowledge funding from the Office of Naval Research (Grant No. N00014-17-1-2702). Amanda M. Loveless also gratefully acknowledges funding from a graduate scholarship from the Directed Energy Professional Society. We thank Sean Dinn for valuable discussions on applying statistical analyses to our data; and we would like to thank Dr. Ayyaswamy Venkttraman for his assistance with the XPDP1 simulations and analysis. I would like to thank Dr. Bernard Y. Tao and Dr. Sally P. Bane for their insights, advice, and guidance as I progressed through my PhD work. We also thank Dr. Robert Bean for allowing the use of his facilities and equipment for performing many of the experiments. Robert Bean has been a mentor both in life and academia that I will forever be thankful for. I would also like to acknowledge the mentorship and guidance from Dr. Allen Garner over the past seven years. He has taught me more than just how to do research but also how to live life as an academic, teacher, and mentor. Finally, I would like to thank my wife, Rebecca Brayfield, for her years of unwavering support even when things seemed bleak. With her support the weight of graduate school was possible to bare.

TABLE OF CONTENTS

LIST OF TABLES	7
LIST OF FIGURES	8
ABSTRACT	12
1. INTRODUCTION	14
1.1 Advantageous Breakdown Applications	14
1.1.1 Biological and Medical Applications	14
1.1.2 Electrical Systems and Aerospace Applications.....	19
1.2 Adverse Breakdown Applications	22
1.2.1 Biological and Medical Applications	22
1.2.2 Electrical Systems and Aerospace Applications.....	25
1.3 Gas Breakdown and Electron Emission Physics	28
1.3.1 Paschen’s Law	29
1.3.2 Field Emission Driven Microscale Gas Breakdown.....	31
1.3.3 Space Charge Limited Emission in Vacuum	34
1.3.4 Space Charge Limited Emission with Collisions	37
1.3.5 Streamer Discharges	38
1.3.6 Overview of Dissertation.....	39
2. THE IMPACT OF CATHODE SURFACE ROUGHNESS AND MULTIPLE BREAKDOWN EVENTS ON MICROSCALE GAS BREAKDOWN AT ATMOSPHERIC PRESSURE.....	41
2.1 Background and Motivation	41
2.2 Materials and Methods.....	43
2.2.1 Materials	43
2.2.2 Methods	44
2.3 Experimental Results	45
2.3.1 Cathode Surface Changes	45
2.3.2 Changes in Breakdown Voltage	48
2.4 Theoretical Assessment	53
2.5 Conclusion	59

3. THE IMPACT OF CATHODE – ANODE GAP ON ELECTRON EMISSION AT ATMOSPHERIC PRESSURE	61
3.1 Background and Motivation	61
3.2 Materials and Methods.....	62
3.3 Results.....	68
3.4 Conclusion	75
4. COMPUTATIONAL ASSESSMENT OF IONIZATION COEFFICIENT	78
4.1 Background and Motivation	78
4.2 Methods.....	81
4.3 Results.....	83
4.4 Conclusion	87
5. FUTURE WORK AND CONCLUSION	89
5.1 Summary	89
5.2 Future Work	91
APPENDIX A. NANOSCALE DATA PROCESSING	96
APPENDIX B. PIC/MCC SIMULATION PARAMETERS	102
APPENDIX C. PIC/MCC SIMULATION SAMPLE CODES	106
REFERENCES	129
VITA.....	135

LIST OF TABLES

Table 2.1: Average surface features before breakdown tests.	47
Table 2.2: Depth of the observed craters at the breakdown voltage for the cathodes polished at each grit where measurable ablation occurred.....	48
Table 2.3: Adjusted p-values from Tukey tests comparing breakdown voltage for 5 μm and 1 μm gaps, 10 μm and 1 μm gaps, and 10 μm and 5 μm gaps for the fifth through tenth breakdown events. Conditions undergoing a statistically significant change are denoted with *. Generally, breakdown events after the fifth event yield a statistically significant breakdown voltage between the 1 μm gap and the other gap distance while no statistically significant difference arises between the 5 μm and 10 μm gaps.....	51
Table 2.4: Average crater depth and breakdown voltage after the tenth breakdown event.....	53
Table 2.5: Summary of parameters used in the theoretical analysis.....	54
Table 3.1: Parameter space used to fabricate devices.....	65
Table 3.2: Estimated breakdown voltage from FN plots for each case presented.....	70
Table 3.3: Summary of upper limit estimates for mobility μ , area A , and the resulting relative error σ between the current and the FN current for the three different gap distances considered.	75
Table 4.1 ²⁶ : Values for A_p and B_p from Ref. [27] , and the E/p and E/N ranges for which they are valid. The E/p range is from Ref. [27] and the E/N range is calculated from (4.3) considering room temperature Ref [28]. Reprinted from A. M. Loveless and A. L. Garner, “A Universal Theory for Gas Breakdown from Microscale to the Classical Paschen Law,” <i>Phys. Plasmas</i> 24 , 113522 (2017), with Permission from AIP Publishing.	79
Table 4.2: Calculated scaling parameters from (4.7) for argon, nitrogen, neon, xenon, and helium.	82
Table 5.1: Parameter space for variable listed in Figure 3.1.	94
<i>Table A.B.1: Parameter space used to create argon simulations and nondimensional constants.</i>	102
<i>Table A.B.2: Parameter space used to create argon simulations and nondimensional constants.</i>	104

LIST OF FIGURES

Figure 1.1: Plasma jet setup (left) and resulting cell cultures (right) showing reduced cell colonies after culturing and plasma jet treatment ⁵ ©[2012] IEEE..... 15

Figure 1.2: Microplasma array schematic (left) with wound healing progress (right) at day 7 showing a 9% reduction in wound size when treated for 20 s ⁹ © IOP Publishing. Reproduced with permission. All rights reserved 16

Figure 1.3: Microplasma pipette setup for applying a plasma to a single LEC, creating various layers of reactive species in the liquid¹² Reproduced with permission CC BY..... 18

Figure 1.4: Stem cell differentiation after 60 s of plasma jet treatment with (a) being the control cells that differentiated on their own, (b) showing no to little growth, and (c) showing a different type of cell growing after treatment ¹³ Copyright (2014), with permission from Elsevier..... 18

Figure 1.5: Spectroscopic scan showing species generated out to 440 nm with the N2 second positive (C-B) and N2 first negative (B-X) bands observed¹⁴ ©[2019] IEEE 19

Figure 1.6: Ignition temperature vs time for conventional heating apparatus and pulsed discharge ignition showing a decreased ignition temperature for the pulsed application and an observed delay in ignition when the same ignition temperate is desired¹⁵© IOP Publishing. Reproduced with permission. All rights reserved 21

Figure 1.7: PI uptake showing cell membrane destabilization after nanosecond and microsecond pulsed electric fields were applied¹⁷ Copyright (2003), with permission from Elsevier..... 23

Figure 1.8: Melanoma death and healing of flesh after treatment of nanosecond pulsed electric field needle array showing complete remission after 65 days ¹⁸ Copyright (2006), with permission from Elsevier..... 24

Figure 1.9: Setup showing ablative electrodes inserted in to rabbit heart ²⁰ Reproduced with permission CC BY 25

Figure 1.10: Transmission line pulse generator schematic (left) with actual implantation (right) used to generate nanosecond pulses for biomedical application in cuvettes with 1-4 mm gaps ²¹ © John Wiley and Sons. Reproduced with permission..... 26

Figure 1.11: Yaw sensor for automotive applications such as stability control safety features with microscale spacing of components ²² © Emerald Publishing Limited all rights reserved..... 27

Figure 1.12: Dependence on nuclear detonation height and effected EMP area²⁴ 28

Figure 1.13: Outline of piecemeal connections of various breakdown mechanisms²⁶ Reprinted with the permission of AIP Publishing. 29

Figure 1.14: Schottky modified work function potential showing finite width..... 32

Figure 1.15: Tunneling effect showing how quantum mechanical distribution of electron potential can lead to breaching the potential barrier. 33

Figure 1.16: Current as a function of voltage showing transition between different emission regimens ⁵¹ Reprinted with the permission of AIP Publishing.	36
Figure 1.17: Plot of nondimensional voltage and gap size showing a third order nexus between Fowler-Nordheim, Child-Langmuir and Mott-Gurney depending on the gap size and voltage for a given electron mobility ⁵⁴ Reprinted with the permission of AIP Publishing.	38
Figure 2.1: Circuit schematic of the experimental setup with a pin to plate configuration to test samples.	44
Figure 2.2: Atomic force microscopy (AFM) measurements of the 800 grit cathode prior to experiments showing the average surface features (a) Optical image of the surface visually showing the surface roughness. (b) Contour mapping of surface height along the surface. (c) AFM arm deflection showing height and depth of the surface features.	46
Figure 2.3: Observed ablated region on the cathode after ten breakdown events for a 5 μm gap with the cathode polished using 800 grit, demonstrating the crater formed in the surface.	47
Figure 2.4: Representative voltage (solid) and current (dashed) waveforms for a $5 \pm 0.5 \mu\text{m}$ gap with the cathode polished using 800 grit for (a) a single breakdown event and (b) the tenth breakdown event. All breakdown events exhibited similar characteristics.	49
Figure 2.5: Breakdown voltage as a function of number of breakdown events for three individual trials for (a) 400 grit (b) 800 grit and (c) 1200 grit samples at 1 μm gap distance.	49
Figure 2.6: Breakdown voltage as a function of number of breakdown events for three individual trials for (a) 400 grit (b) 800 grit and (c) 1200 grit samples at 5 μm gap distance.	50
Figure 2.7: Breakdown voltage as a function of number of breakdown events for three individual trials for (a) 400 grit (b) 800 grit and (c) 1200 grit polished cathodes at 10 μm gap distance.	50
Figure 2.8: Average breakdown voltage as a function of number of breakdown events for (a) 400 grit (b) 800 grit and (c) 1200 grit for three trials each.	52
Figure 2.9: Average breakdown voltage, V , as a function of effective gap distance, $d_{eff} = d + \delta$, where d is the anode-cathode gap and δ is the breakdown induced crater depth, compared to numerical results from (2.1) and analytic results from (2.2). The product of the ionization coefficient and effective gap distance, αd_{eff} , is displayed on the secondary vertical axis as a function of d_{eff} . The largest two gap distance points have $\alpha d_{eff} \gg 18$, which exceeds Meek's criterion for streamer formation.	56
Figure 2.10: (a) Field enhancement factor, β , as a function of effective gap distance, $d_{eff} = d + \delta$, where d is the gap distance and δ is the crater depth, showing that β is approximately linear until the larger gap distances corresponding to the transition to Townsend avalanche, where it becomes constant. (b) The ratio of the field emission component to the Townsend component, $\mu\nu$, as a function of d_{eff} , demonstrating that field emission effects govern breakdown until $d_{eff} \approx 10 \mu\text{m}$, which corresponds to $\alpha d_{eff} \approx 10$. This point coincides with the transition of β from linear to constant in (a), indicating the transition to the traditional Paschen's law.	57
Figure 2.11: Breakdown voltage, V , as a function of effective gap distance, $d_{eff} = d + \delta$, where d is the gap distance and δ is the crater depth, from the experimental data, the numerical results of	

(2.1), and the analytic results of (2.3) assuming $\gamma_{SE} = 1.5 \times 10^{-3}$. The product of the ionization coefficient and effective gap distance, αd_{eff} , is shown on the secondary vertical axis. The transition to Paschen's law (PL) occurs for $\alpha d_{eff} \approx 10$. PL predicts breakdown until it becomes driven by streamer formation when $\alpha d_{eff} > 18$ 58

Figure 2.12: The product of the ionization coefficient and effective gap distance, αd_{eff} , as a function of the effective gap distance gap distance, $d_{eff} = d + \delta$, where d is the gap distance and δ is the crater depth. Each pair of symbols shows the αd_{eff} value after the first and tenth breakdown events, showing that crater formation can push breakdown behavior past the $\alpha d_{eff} \approx 10$ criterion for transition to Paschen's law. 58

Figure 3.1: Geometry of the designed nanoscale device showing the sharp or blunt surface protrusion to evaluate field enhancement through current emission measurement and scaling by altering a , h , and d and fixing α 63

Figure 3.2: (a) The cross-section of the fabrication process showing the poly-methyl methacrylate (PMMA) photo-resist layer with an electrical insulation layer of SiO_2 , and an electrode layer of 5 nm of titanium under a 100 nm layer of gold. (b) shows the general shape of the devices considered before the 100 μm pads are added to the design to facilitate testing. 64

Figure 3.3: Layout of devices on 1 cm \times 1 cm square chips cut from silicon wafer with a view of the device layout showing spacing for testing. 67

Figure 3.4: Electrical testing setup of the Keithley 2410C source meter unit (SMU) to apply voltage and measure current across the test devices⁸⁴. 68

Figure 3.5: FN scaling of the data for (a) with $a = 192 \text{ nm} \pm 10 \text{ nm}$ and $d_{eff} = 57 \text{ nm} \pm 10 \text{ nm}$, $115 \text{ nm} \pm 10 \text{ nm}$, and $230 \text{ nm} \pm 10 \text{ nm}$ and (b) with $d_{eff} = 115 \text{ nm} \pm 10 \text{ nm}$ and $a = 38 \text{ nm} \pm 10 \text{ nm}$, $192.3077 \text{ nm} \pm 10 \text{ nm}$, and $384 \text{ nm} \pm 10 \text{ nm}$ showing strong gap dependence on breakdown voltage but no dependence on width $2a$ 69

Figure 3.6: Experimental data for $d_{eff} = 28 \text{ nm} \pm 10 \text{ nm}$ and a fitted emission area of 64 nm^2 fit to full theory from Darr, et. al. using mobility of (a) $0.00015 \text{ m}^2\text{V}^{-1}\text{s}^{-1}$ and (b) $0.001 \text{ m}^2\text{V}^{-1}\text{s}^{-1}$ showing FN dominated emission transitioning to breakdown as the device fails and (c) the associated FN plot for Ref. [54]. 71

Figure 3.7: Transition behavior for $d_{eff} = 125 \text{ nm} \pm 10 \text{ nm}$ using mobilities of (a) $0.0003 \text{ m}^2\text{V}^{-1}\text{s}^{-1}$ and (b) $0.001 \text{ m}^2\text{V}^{-1}\text{s}^{-1}$. Using the lower mobility predicts transition to MG; however, the full theory does not match the experimental data. The higher mobility agrees better with the experimental results and indicates that the data primarily follows FN over this regime. 72

Figure 3.8: JV plot for a device with d_{eff} of $450 \text{ nm} \pm 10 \text{ nm}$ and a fitted emission area of 64 nm^2 with mobilities of (a) $0.003 \text{ m}^2\text{V}^{-1}\text{s}^{-1}$ and (b) $0.01 \text{ m}^2\text{V}^{-1}\text{s}^{-1}$ showing no transition behavior, moving directly from FN dominant emission to breakdown. 73

Figure 3.9: Transition voltage presented from (3.4) for $\mu = 0.00299 \text{ m}^2\text{V}^{-1}\text{s}^{-1}$, $A = 6.4 \times 10^{17} \text{ m}^2$, $A_{FN} = 0.0013 \text{ AeV} \cdot \text{V}^{-2}$, and $B_{FN} = 1.1645 \times 10^9 \text{ Vcm}^{-1}\text{eV}^{-3/2}$ demonstrating that the minimum voltage for the transition from FN to MG to occur is for $d_{eff} \approx 0.02 \text{ nm}$ 74

Figure 4.1: Ionization coefficient α/p computed as a function of E/p using one-dimensional PIC-MCC simulations and the corresponding empirical parameters, where E is electric field and p is pressure. The experimental data is obtained indirectly using the breakdown data for 100 μm based on $\gamma_{SE} = 0.00532$ © [2020] IEEE 80

Figure 4.2: Variation of the ratio of microscale to macroscale α/N as a function of applied voltage for all simulations considered in this work. Also included for reference is the variation proposed by the empirical correlation in (4.5) © [2020] IEEE 81

Figure 4.3: Simulation results for $\ln(\alpha/p)$ as a function of the p/E for helium. 84

Figure 4.4: Simulation results for $\ln(\alpha/p)$ as a function of the p/E for argon. 85

Figure 4.5: Nondimensionalized assessment of $\ln(\bar{\alpha}/\bar{p})$ as a function of \bar{p}/\bar{E} for helium. 86

Figure 4.6: Nondimensionalized assessment of $\ln(\bar{\alpha}/\bar{p})$ as a function of \bar{p}/\bar{E} for argon. 87

Figure 5.1 New chip carrier with pin connections to connect directly to breadboard/feedthrough for testing. 91

Figure 5.2: New vacuum chamber from Varex Imaging with feed through connections that will allow easy testing of multiple devices. 92

Figure 5.3: Pumping station connected to entire testing system used for benchmarking new device fabrication. 93

Figure 5.4: Fowler-Nordheim curves for the Notre Dame (left) and University of Chicago (right) 93

Figure 5.5: Proposed nanoscale chip design for thermionic emission experiments. 95

ABSTRACT

Developments in modern electronics drive device design to smaller scale and higher electric fields and currents. Device size reductions to microscale and smaller have invalidated the assumption of avalanche formation for the traditional Paschen's law for predicting gas breakdown. Under these conditions, the stronger electric fields induce field emission driven microscale gas breakdown; however, these theories often rely upon semi-empirical models to account for surface effects and the dependence of gas ionization on electric field, making them difficult to use for predicting device behavior *a priori*.

This dissertation hypothesizes that one may predict *a priori* how to tune emission physics and breakdown conditions for various electrode conditions (sharpness and surface roughness), gap size, and pressure. Specifically, it focuses on experiments to demonstrate the implications of surface roughness and emitter shape on gas breakdown for microscale and nanoscale devices at atmospheric pressure and simulations to extend traditional semi-empirical representations of the ionization coefficient to the relevant electric fields for these operating conditions.

First, this dissertation reports the effect of multiple discharges for 1 μm , 5 μm , and 10 μm gaps at atmospheric pressure. Multiple breakdown events create circular craters to 40 μm deep with crater depth more pronounced for smaller gap sizes and greater cathode surface roughness. Theoretical models of microscale breakdown using this modified effective gap distance agree well with the experimental results.

We next investigated the implications of gap distance and protrusion sharpness for nanoscale devices made of gold and titanium layered onto silicon wafers electrically isolated with SiO_2 for gas breakdown and electron emission at atmospheric pressure. At lower voltages, the emitted current followed the Fowler-Nordheim (FN) law for field emission (FE). For either a 28 nm or 450 nm gap, gas breakdown occurred directly from FE, as observed for microscale gaps. For a 125 nm gap, emission current begins to transition toward the Mott-Gurney law for space-charge limited emission (SCLE) with collisions prior to undergoing breakdown. Thus, depending upon the conditions, gas breakdown may directly transition from either SCLE or FE for submicroscale gaps.

Applying microscale gas breakdown theories to predict this experimental behavior requires appropriately accounting for all physical parameters in the model. One critical parameter in these

theories is the ionization coefficient, which has been determined semi-empirically with fitting parameters tabulated in the literature. Because these models fail at the strong electric fields relevant to the experiments reported above, we performed particle-in-cell simulations to calculate the ionization coefficient for argon and helium at various gap distances, pressures, and applied voltages to derive more comprehensive semi-empirical relationships to incorporate into breakdown theories.

In summary, this dissertation provides the first comprehensive assessment of the implications of surface roughness on microscale gas breakdown, the transition in gas breakdown and electron emission mechanisms at nanoscale, and the extension of semi-empirical laws for ionization coefficient. These results will be valuable in developing theories to predict electron emission and gas breakdown conditions for guiding nanoscale device design.

1. INTRODUCTION

Gas breakdown may be either beneficial or detrimental depending on the application. The generated plasma produces reactive species and causes electrical effects such as ohmic heating. These phenomena can drastically alter material properties, which can cause device failure in microelectromechanical systems (MEMS) or ablate tumor cells. Medical/environmental, electrical, and aerospace applications all have examples of advantageous and adverse effects of this gas breakdown.

1.1 Advantageous Breakdown Applications

1.1.1 Biological and Medical Applications

The reactive species generated by microscale plasma discharges have been used for multiple medical and environmental applications. Atmospheric pulsed plasma jets are promising for microorganism inactivation for numerous applications such as dental treatment and surface treatment^{1,2}. Pothiraja, et. al. demonstrated that a plasma jet produced in small capillaries under flowing gas condition to produce plasma “bullets” that impinged on the target induced a 4-log reduction of *E. coli*³. In 2011, Weng, et al. applied the principle to small glass capillaries for aqueous inactivation⁴ to show that 90-180 s treatments inactivated *E. coli* in solution to the same degree as accepted methods. Sedghizadeh, et al. to characterized the inactivation kinetics when applying a 1 mm wide helium/oxygen plasma jet to pathogenic microorganisms on agar mounts⁵. Figure 1.1 shows the setup utilizing a jet mounted above an agar plate for treatment. The gas feed to the plasma jet was maintained at 1 SLPM and had an applied voltage of 6 kV at 1.5kHz. The plasma jet induced a 2 -3 log reduction for *P. aeruginosa*, *E. coli*, and *C. albicans* and a 4-4.5 log reduction of *S. aureus* and *S. epidermidis* after 30 s of treatment with negligible thermal effects.

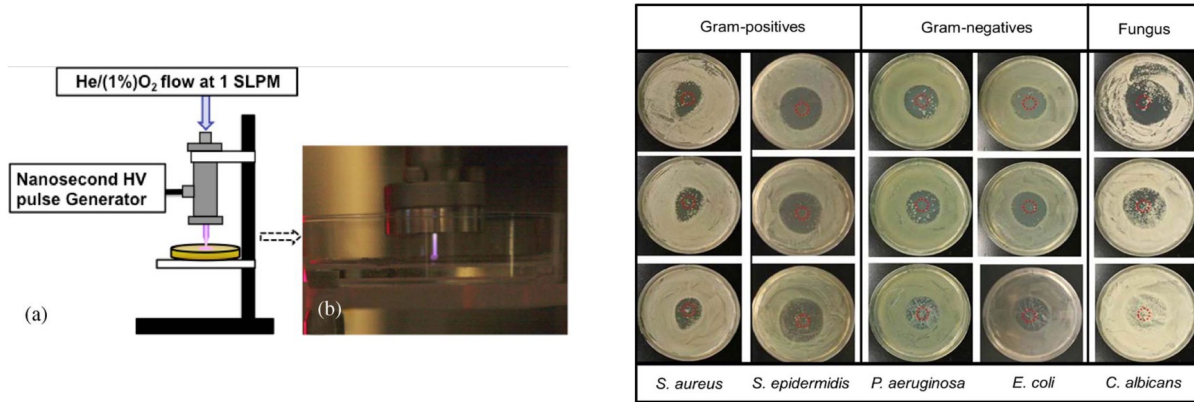


Figure 1.1: Plasma jet setup (left) and resulting cell cultures (right) showing reduced cell colonies after culturing and plasma jet treatment ⁵ ©[2012] IEEE

This shows significant potential for surface treatment for medical equipment, food, dental equipment, and skin applications. More recent work by Shamsurin, et al. examined the physical phenomena behind the breakdown forming the plasma jet formed with 3 to 40 kV at kHz repetition rates with pulse durations on the order of microseconds⁶. They first examined the breakdown between the anode and cathode by examining the Townsend avalanche that initially forms at the cathode. The avalanche eventually became so strong just before the anode that a strong electric field arose at the tail of the avalanche to initiate a streamer that propagated from the anode to the cathode. The streamer radius was on the order of 0.15 mm. This streamer formed on timescales on the order of microseconds compared to the pulse repetition rate of kHz. The streamer was cut off from fully bridging the cathode anode gap and moved with the gas flow out of the device. Shamsurin, et al. further quantified each stage of the breakdown process in the jet as a function of time to temporally characterize plasma jet formation and the emission process.

Scaling down the concept of plasma jet application, Park, et al. studied microscale arrays of plasma jets to treat fungal keratitis⁷, a common medical condition in which the cornea becomes inflamed with fungal filaments. They applied either a standard single micro-tipped plasma jet and a 4×4 array of 500 μm jets mounted into a silicon “contact lens” type applicator to lab infected rabbits with their left eyes uninfected and their right eyes infected with *Candida albicans*. Optical emission spectroscopy showed that the array application induced more uniform species distribution and overall higher species production at lower power consumptions. Both the single jet and array returned the cornea clarity to that of the control with no clouding of the cornea material; however, the single jet produced pro-inflammatory responses in the cornea, which could

alter vision and induce cornea thickening. The array application provides another potential treatment option that does not require high dose antibiotics. These studies have examined the generation and effect of the microplasma for various applications. This naturally leads to the application of these plasmas directly to wounds to promote healing.

The reactive species generated from plasmas are also effective for direct application to wounds for purposes of sterilization and healing^{2,8}. In 2014, Park, et al. applied a 6×6 array of microscale hourglass configuration plasma jets to open wounds on mice⁹. The jets consisted of a unique cross-sectional design that were produced by nanofabrication using photolithography and micro-powder ablation to provide arrays with finely controlled geometries. The jets operated at 190-374 VAC at 20 kHz with a flow of 0.35 slm/microcavity of the array. The jet array was applied directly to mice with three 1 cm² wounds on their stomachs with one wound left as an untreated control and the other two treated with a single 10 s (designated P10) application or a single 20 s (designated P20) application. The treatment was repeated twice a day for 7 d. Figure 1.2 shows the array and resulting wound healing after 7 d of treatment.

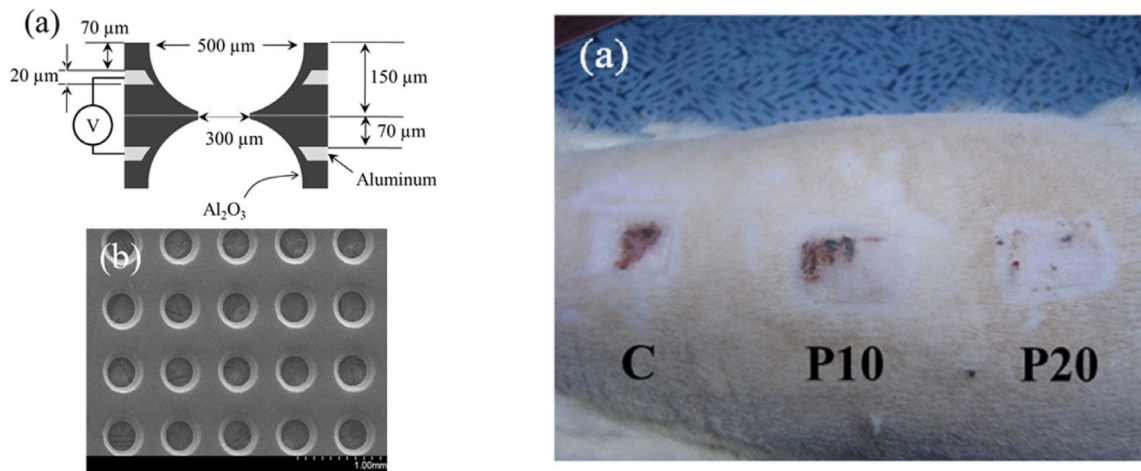


Figure 1.2: Microplasma array schematic (left) with wound healing progress (right) at day 7 showing a 9% reduction in wound size when treated for 20 s⁹ © IOP Publishing. Reproduced with permission. All rights reserved

Figure 1.2 clearly shows the microplasma array had a significant impact on wound healing. The P20 treatment reduced the wound to approximately 9% of its original size in just 7 d. The authors hypothesized that the observed formation of large concentrations of nitrogen and oxygen species interacted with the wound to produce NO. NO potentially stimulates regenerative biochemistry processes such as vasodilation stabilization of microcirculation, enhancement of bacterial

phagocytosis and nerve conductance, vascular growth by secretion of cytokines, fibroblast and keratinocyte proliferation, and increased collagen production. In 2016, Shao, et al. applied N₂/Ar jets to belly wounds on mice and used various immunoassays and imaging techniques to quantify the ensuing wound healing to confirm that microplasma jets produced large amounts of NO in the wound¹⁰.

Direct microplasma application may also induce apoptosis (programmed cell death) of cancer cells. Tan, et al. used a simple Tesla coil type AC voltage supply to provide 5 kV at 25 kHz to form a plasma from a 10 μm tip of a tungsten dissection needle to directly treat human hepatoma (HepG2), human cervical cancer (HeLa), and normal liver cells (L-02)¹¹. They used a 10 MΩ resistor to limit current to avoid damaging the needle and heating heat the cell. They applied voltage for 10 -15 s to only a single cell by using a manipulator to place the tip near a small group of cells. Cell membrane blebbing occurred on only the treated cell 20 min after application. To study this more in depth, green fluorescent label Annexin V-FITC was used to indicate binding to apoptotic cells. Dye binding occurred 5 min after treatment and increased over time only for the treated cell. DNA staining by Hoechst 33342 dye showed that the nucleus condensed 6 min after treatment, signifying the start of apoptosis.

In 2016, Recek utilized a plasma jet made out of a micropipette with an inner diameter of 0.8 mm to treat a single human lens anterior epithelial cell (LEC)¹². LECs cause secondary or post-surgical vision loss after cataract removal. In this study, a single cell was treated with a microplasma jet generated by using helium with 1 W of applied power (voltage not specified) at 25 kHz. Figure 1.3 shows the unique setup used to treat the LEC. The setup used a USB controlled micromanipulator to move the micropipette in position. Depending on the cell media and the volume of media around the cell, different species impacted the cell membrane.

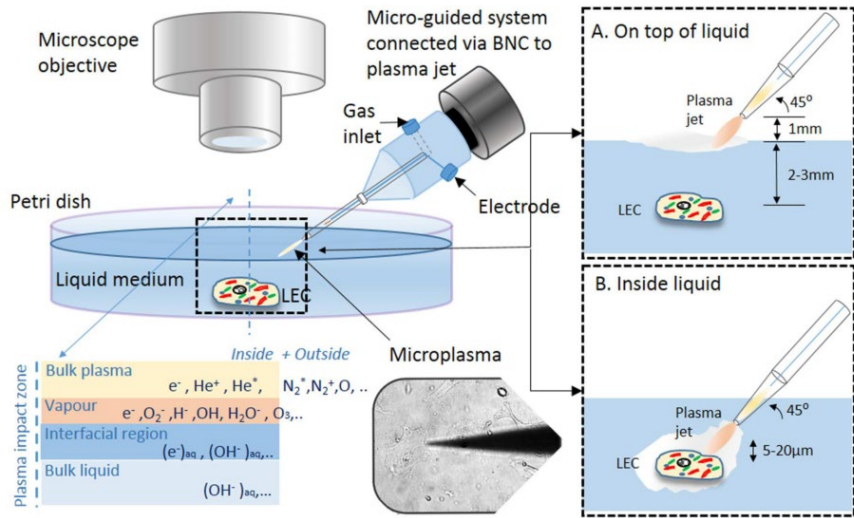


Figure 1.3: Microplasma pipette setup for applying a plasma to a single LEC, creating various layers of reactive species in the liquid¹² Reproduced with permission CC BY

Using various dye assays and FLIR imaging, 30 s of treatment induced significant morphological effects on the cells without significantly heating the system. The cells shrank and appeared apoptotic based on the presence of apoptotic bodies in the surrounding medium. After 30 min, weak membrane blebs were present following either indirect and direct application. Thus, this technique lends itself well to direct patient application to reduce LECs after surgery.

Xiong, et al. used a microplasma jet to alter neural stem cell differentiation¹³. The jet was applied directly to C17.2 neural stem cells (C17.2-NSCs) in a Petri dish for 60 s, which were then cultured and observed at various time points. Figure 1.4 shows the optical images of the cell differentiation after 2 d of culture.

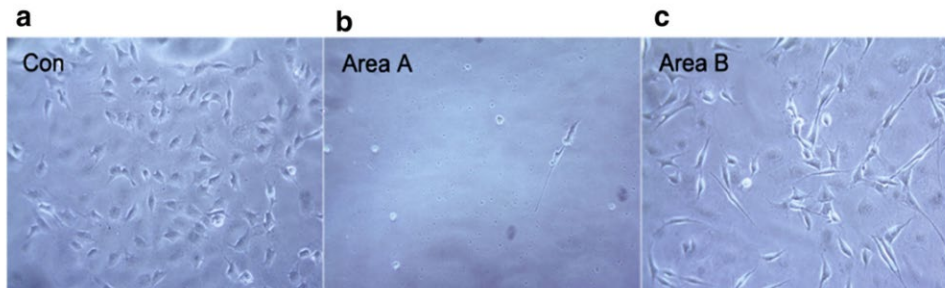


Figure 1.4: Stem cell differentiation after 60 s of plasma jet treatment with (a) being the control cells that differentiated on their own, (b) showing no to little growth, and (c) showing a different type of cell growing after treatment¹³ Copyright (2014), with permission from Elsevier

After 6 d, immunofluorescence studies were used to identify neuron subtype-specific markers, such as NF200 (mature neurons), ChAT (cholinergic neurons), Hb9 and LHX3 (motor neurons), GABA (GABAergic neurons), Serotonin (serotonergic neurons), and TH (dopaminergic neurons). NF200, ChAT, and LHX3 biomarkers showed very strong immunofluorescence responses in the plasma-treated C17.2-NSC cells indicating distinct cell differentiation. Western Blot analysis confirmed the same biomarkers; Hb9 was studied in more detail to more specifically identify the developed motor neurons.

1.1.2 Electrical Systems and Aerospace Applications

As electronics advance, component sizes become smaller and more closely packed together. Piezoelectric transformers have long been used as sources of backlight fluorescence in monitors, x-ray generation devices, low voltage battery chargers, and AC/DC converters¹⁴. Piezoelectric devices may also be used to generate a dielectric barrier discharge (DBD) in a quartz tube having an outer diameter of 6.35 mm and an inner diameter of 3.85 mm and no metallic connectors within approximately 10 cm of the plasma region. Helium was used at a flow rate of 43.5 sccm at a pressure of 1.75 atm. Nitrogen was supplied at 0.5 sccm when emission spectra was utilized for rotational and vibrational information. The piezoelectric was driven at 124 kHz at a maximum of 15 V RMS and 100 mA RMS. The resonance of the piezoelectric at that frequency induced alternating electric fields in the quartz tube producing a DBD type plasma. This was observed with a photomultiplier tube (PMT) by periodic light intensity observed as the plasma evolved in time. Figure 1.5 shows the species present in the plasma after 1000 exposures using a 1200 line per mm grating with a spectrometer.

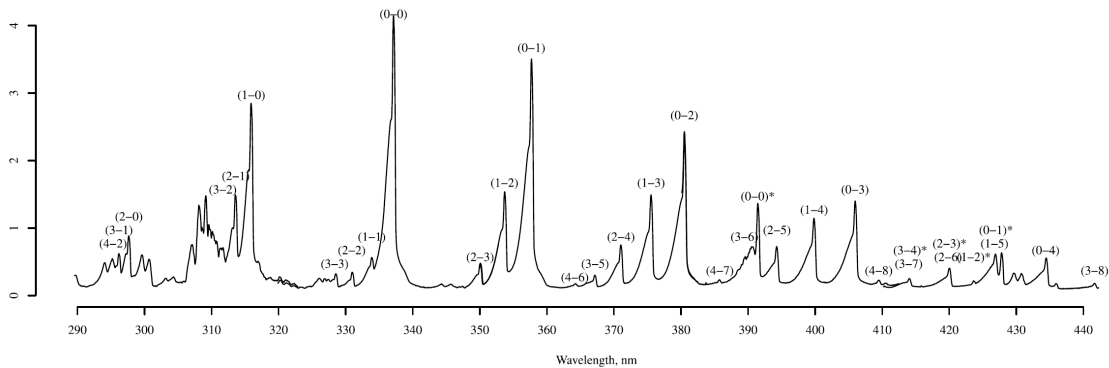


Figure 1.5: Spectroscopic scan showing species generated out to 440 nm with the N2 second positive (C-B) and N2 first negative (B-X) bands observed¹⁴ ©[2019] IEEE

Figure 1.5 shows the first negative (B-X) and second positive (C-B) transitions of nitrogen and OH lines near 310 nm. Using the C-B transition and collecting 5000 exposures yielded a rotational, vibrational, translation, and electron temperatures of 38 meV, 200 meV, 33 meV, and below 1 eV, respectively. This is significant because it shows the formation of nonequilibrium “cold” plasmas even at a relatively high pressure.

High pressure non-equilibrium plasma may also be used to alter ignition and high-speed flow control processes for the aerospace industry¹⁵. Applying up to 1000 20 kV pulses at a repetition rate of 20-50 kHz with durations of up to 25 ns ignited a slow flow reactor. The discharge flow reactor was fabricated from a single piece rectangular cross section quartz channel, 150 mm long \times 22 mm span \times 10mm height, with 1.75 mm thick walls and flanges at the ends for connecting gas inlet and exit lines. Two rectangular copper plate electrodes, 14 mm wide and 63 mm long each, were attached to the outside surface of the quartz channel to generate the plasma. Optical diagnostics such as emission spectroscopy in the UV VIS range and oxygen two-photon absorption laser induced fluorescence (TALIF) were conducted to study species evolution and temperatures as the ignition event evolved. Pulses ignited the flow at a much lower temperature than standard uniform heating. Moreover, the pulses reduced ignition time by two orders of magnitude for the same ignition temperature.

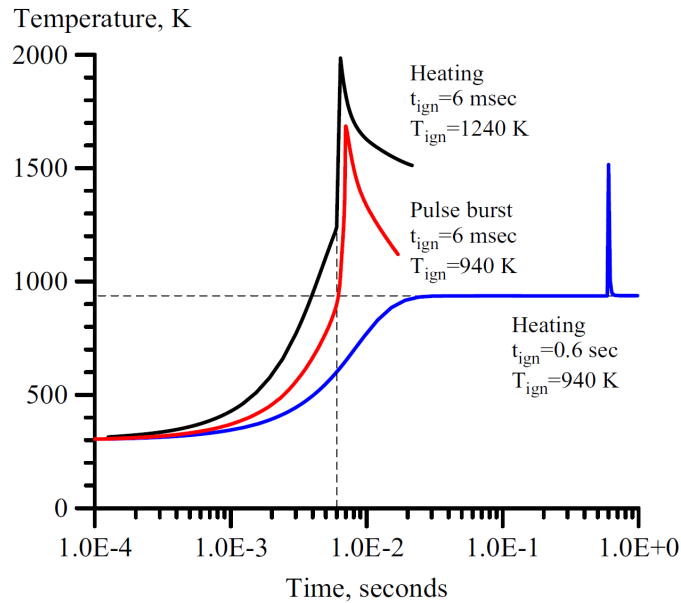


Figure 1.6: Ignition temperature vs time for conventional heating apparatus and pulsed discharge ignition showing a decreased ignition temperature for the pulsed application and an observed delay in ignition when the same ignition temperature is desired¹⁵© IOP Publishing. Reproduced with permission. All rights reserved

Figure 1.6 shows that for the same ignition temperature, a delay was present when using a conventional heating source. The pulse burst also decreased the required ignition temperature by 300 K when keeping ignition time constant. The same study utilized a plasma actuator to explore flow control. Utilizing a converging – diverging nozzle, a Mach 0.9 jet was produced and flowed into the actuator. A boron nitride plate was attached to the exit of the nozzle with pin electrodes made of tungsten wire with diameter of 1 mm. The nozzle exit cross section was 1.27 cm × 3.81 cm, and the flat plate dimensions were 2.5 cm × 4 cm. A 0.5 mm deep and 1 mm wide groove, machined into the flat plate 1 mm from the trailing edge, housed four pairs of pin electrodes distributed spanwise. The plasma was generated using a DC pulse generator or an RF generator, both designed to output at 0 to 50-100 kHz pulse repetition. The rise time was 4-5 μs and 2-3 μs for the DC and RF source, respectively. The flow was observed using emission spectroscopy to diagnose nitrogen transitions to gain information about temperature of the species. Additionally, Schlieren imaging in an anechoic chamber showed that the flow from the RF discharge was hotter than the DC discharge. This suggests that more energy goes into heating the flow than eroding and

heating the nozzle and actuator, as with the DC discharge. Thus, RF discharges may offer better performance when localized perturbations near the wall are required.

1.2 Adverse Breakdown Applications

1.2.1 Biological and Medical Applications

Many biological applications using pulsed power require applying nanosecond pulsed electric fields that do not induce breakdown to achieve various results such as creating nanopores in the cellular membrane that allow drug uptake or inducing apoptosis^{1,2}.

Beebe, et. al. noted that nanosecond pulsed electric fields (nsPEFs) could induce apoptosis and inhibit tumor cell division¹⁶. Applying nsPEFs induced apoptosis, as indicated by caspase activation, externalized phosphatidylserine, and fragmented DNA in the tumor cells. In vivo nsPEF-treated fibrosarcoma tumors grew more slowly than sham-treated tumors.

Deng, et. al. used propidium iodide (PI) to assess membrane permeabilization for cell exposed to pulsed electric fields (PEFs) with durations from 60 ns to 100 μ s.¹⁷ Florescent dye imaging utilizing PI was used to observe cell membrane integrity, as shown in Figure 1.7. Microsecond duration PEFs induced immediate PI uptake, consistent with electroporation, or the formation of membrane pores for PEFs of sufficient duration and intensity. Applying 60 ns PEFs induced a delayed, significant uptake in PI compared to 300 ns PEFs. Cellular swelling occurred rapidly following 300 ns pulses but was minimal following 60 ns pulses. Thus, nsPEFs induced distinct membrane effects compared to microsecond PEFs.

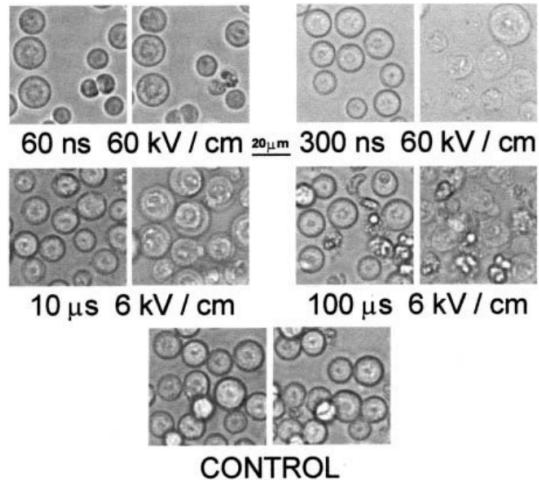


Figure 1.7: PI uptake showing cell membrane destabilization after nanosecond and microsecond pulsed electric fields were applied¹⁷ Copyright (2003), with permission from Elsevier.

In 2006, Nuccitelli, et. al. used arrays of microneedles spaced about 4 mm apart to treat melanomas in mice with one hundred 300 ns duration PEFs at 40 kV/cm and a repetition rate of 0.5 Hz at days 0, 1, 2, 21, 22, and 23¹⁸. The tumor began to shrink within two days of treatment and had gone completely into remission after 65 days, while the control tumor continued to grow normally. Figure 1.8 shows the tumor changes over time. The tumor self-destructed without increased caspase activity, indicating that apoptosis was not induced. Pyknosis and restricted blood flow were observed and attributed to the death of the tumor. This led the authors to postulate that this could be a viable treatment in humans to treat melanoma without surgery or drugs.

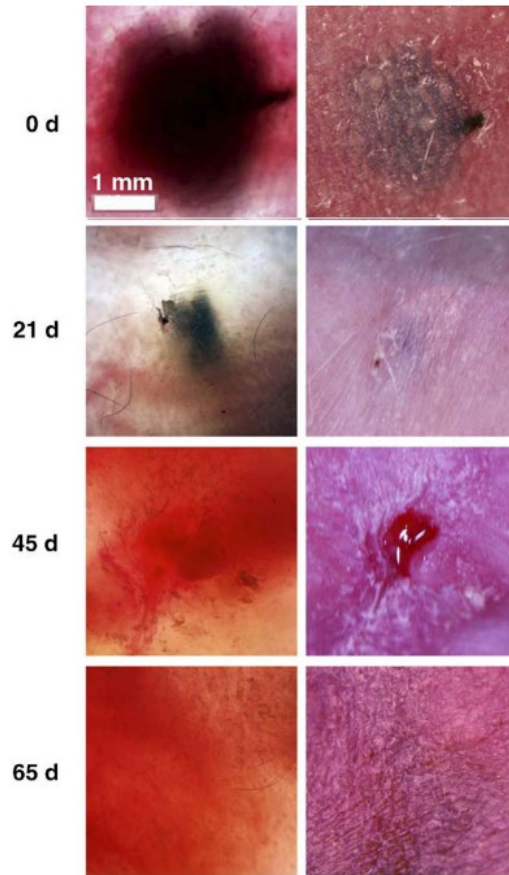


Figure 1.8: Melanoma death and healing of flesh after treatment of nanosecond pulsed electric field needle array showing complete remission after 65 days¹⁸ Copyright (2006), with permission from Elsevier

Chen, et. al. explored using nsPEFs to treat carcinoma in rats¹⁹. N1-S1 tumors were treated with pulse duration of 100 ns, electric field strengths of 50 kV/cm, a repetition rate of 1 Hz and various numbers of pulses. Applying between 100 and 1000 pulses significantly decreased tumor weight two weeks after treatment. A second study evaluating tumors six weeks after treatment indicated that most sham-treated rats required euthanasia before six weeks due to tumor burden and some tumors treated with fewer than 1000 pulse continued to grow. In contrast, tumors treated with 1000 pulses completely regressed. N1-S1 tumors treated with nsPEFs had a significant number of cells with active caspase-3 and caspase-9, but lacked caspase-8. This indicated that both an apoptotic and caspase-independent mechanism were present in the tumor death. Most remarkably, rats with successfully ablated tumors failed to re-grow tumors when a second injection of N1-S1 cells were implanted in the same or different liver lobe that harbored the original tumor.

Xie, et. al. applied trains of nsPEFs to cardiac tissue of rabbits to study myocardial ablation²⁰. Myocardial ablation is currently used to treat fibrillation, atrial flutter, and ventricular tachycardia but suffer from thermal side effects, long procedure times, and high rates repeated procedures for effectiveness. Current techniques utilizing RF power or cryoablation have massive thermal detriments to the surrounding tissues. Nanosecond pulsed electric fields offer the unique ability to effect cell integrity and induce cell death without requiring tissue heating. This also indicates that tissue with dense neuron formations can be treated without damaging the function of the surrounding tissues. To test this, two electrodes spaced 2–4 mm apart were inserted into the ventricles and various numbers of 350 ns duration nsPEFs from 5–20 kV/cm with 350 ns duration with different repetition rates were applied to create 12-18 mm long linear lesions. Figure 1.9 shows the setup and application directly through the walls of the heart.

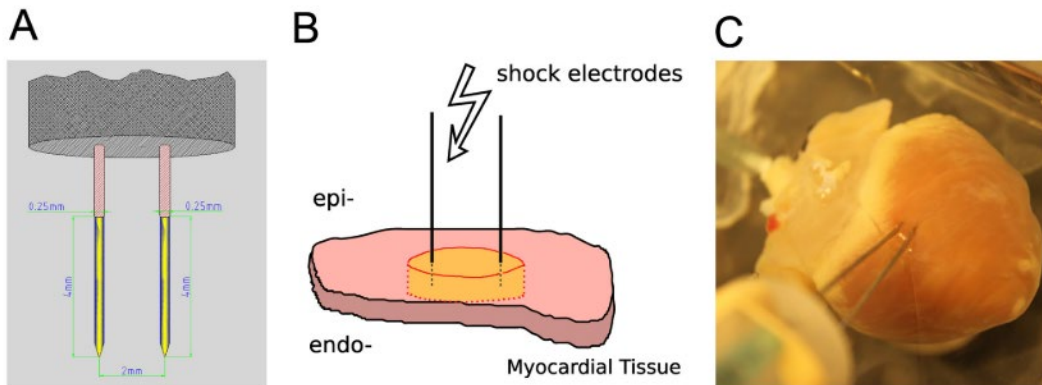


Figure 1.9: Setup showing ablative electrodes inserted in to rabbit heart²⁰ Reproduced with permission CC BY

Hearts were then stained either with tetrazolium chloride (TTC) or propidium iodide (PI) to determine the extent of ablation. The nsPEFs induced cell death and caused lesions between 2 and 5.5 mm depending on electrode spacing and pulse amplitude. A complete absence of thermal effects to the surrounding tissue offers great promise for this technique in the future to treat human subjects with increased success.

1.2.2 Electrical Systems and Aerospace Applications

The applications previously mentioned rely on pulsed power system development to deliver the electrical pulses. Kolb, et. al. developed solid state pulse generators that achieve the

fast rise time required for biomedical applications²¹. For gaps less than 100 μm , electric fields of 10 MV/cm may be easily generated using ultra-fast MOSFET switches to provide compactness and ease of use. However, for larger gaps of 1-4 mm (e.g. cuvettes), applied voltages exceed 10 kV, which rules out the use of solid state switching to achieve rectangular pulses. Instead, a transmission line style pulse generator, as shown in Figure 1.10, was designed. The pulse generator consisted of aluminum conductors with Teflon sheets used as dielectric material. Instead of MOSFETs, this design used a brass-hemispherical spark gap switch under high pressure of SF₆ or nitrogen to achieve 10 kV in bursts of up to 2000 pulses, with a repetition rate of 2 Hz, and 30 kV, in bursts up to 800 pulses, with a repetition rate of 1 Hz.

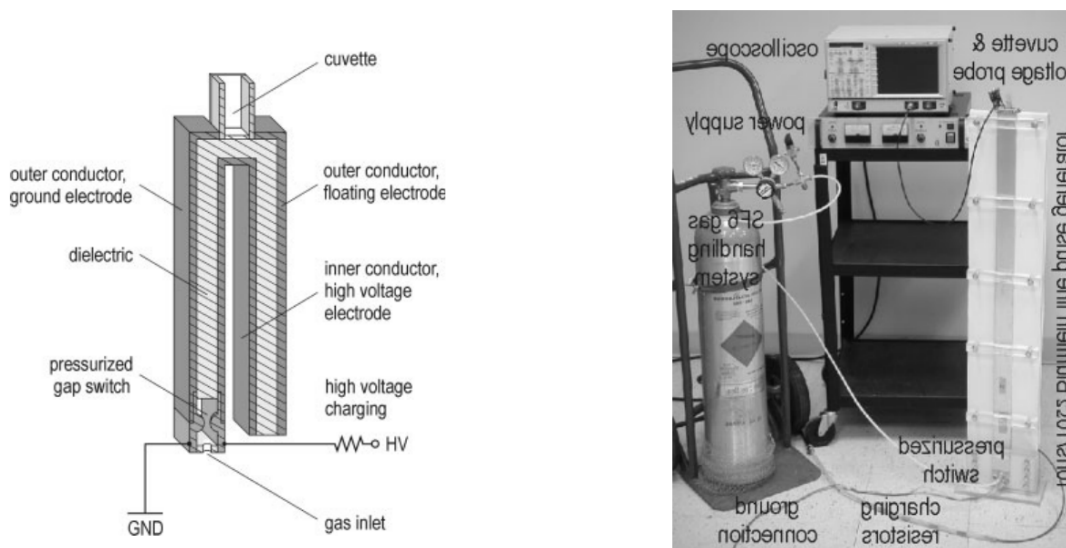


Figure 1.10: Transmission line pulse generator schematic (left) with actual implementation (right) used to generate nanosecond pulses for biomedical application in cuvettes with 1-4 mm gaps²¹ © John Wiley and Sons. Reproduced with permission

Submillimeter electronics, such as microelectromechanical systems (MEMS), are increasingly used in biotechnology, medicine, and communications²². Continuing reduction in the size of MEMS increases the importance of preventing breakdown between their nanofabricated components. The components of MEMS are typically nanofabricated on semiconductor wafers using various metal alloys as conductors. The spacing of these conductors is on the order of tens to hundreds of microns. One such example is found in yaw sensors of automobiles as part of stability control systems, which are a required safety feature on all new vehicles in the United

States since 2012. Figure 1.11 shows an optical image of such a device. The components very closely align with each other. An electrostatic discharge (ESD) occurring between the tips of the device parts will very easily damage the device.

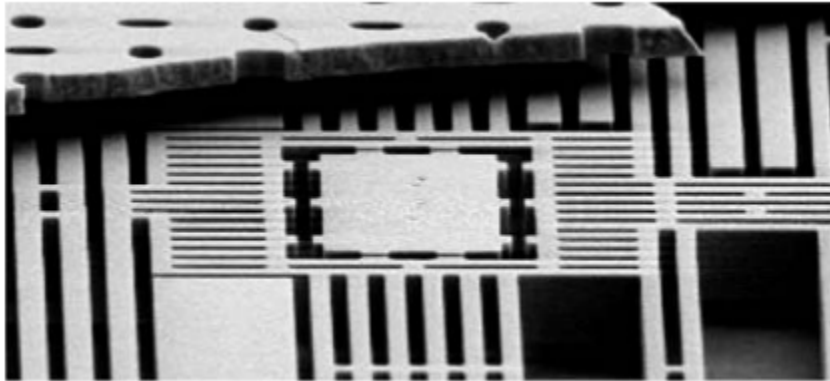


Figure 1.11: Yaw sensor for automotive applications such as stability control safety features with microscale spacing of components ²² © Emerald Publishing Limited all rights reserved.

Nanoelectromechanical systems (NEMS) are increasingly used for sensing and scanning²³ with common applications including electronic displays, printers, and airbags. One such system is of micromechanical mirrors that can be tilted very accurately. Created by Lucent Technologies, the mirrors' diameters are on the order of 0.4 mm with micron spacing between them, however the supporting wires and structure are on the order of 50 nm or 200 times smaller than previous devices used for similar applications. The mirrors are driven by AC voltage applied to the substrate beneath them, causing micromechanical oscillations. Even a slight deviation in the voltage at this scale can cause an arc and device failure.

Other potential sources of electrostatic discharge failure, as reported to Congress in 2008 by the Congressional Research Service, are High Altitude Electromagnetic Pulses (HEMP) and High Power Microwaves (HPM)²⁴. Detonated at altitude, nuclear weapons create a series of energy pulses that are collectively known as Electro-Magnetic Pulses (EMP). The EMP arrive and cause failure to micro- and nanoscale devices by causing electrostatic discharge between components. Figure 1.12 shows that the height of detonation has a direct impact on the area effected. Given that critical infrastructure is in a few locations in the country, such an attack could pose a great threat even if it is localized to a single city.

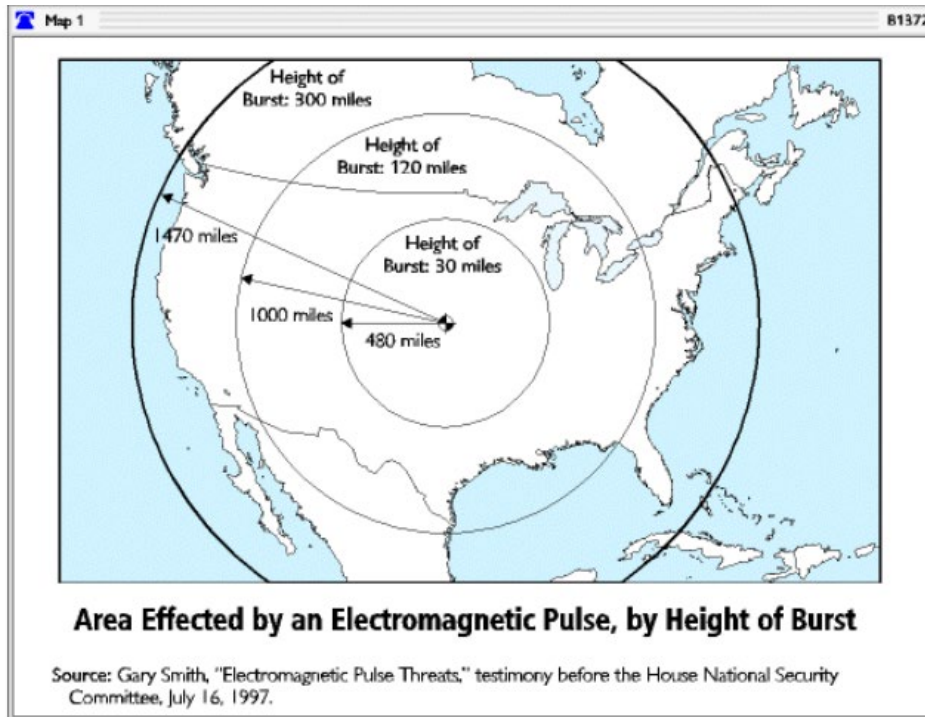


Figure 1.12: Dependence on nuclear detonation height and effected EMP area²⁴

ESD can also be generated in aerospace applications as vehicles move through the atmosphere, posing risk to antennas and other discharge sensitive electronics²⁵. Paschen's law (PL) predicts the breakdown voltage of a gas due to the formation of an avalanche between two electrodes. PL does not consider when the gas is flowing and has particulate matter in the flow stream, which can cause localized field enchainment that can trigger a discharge event. Hogue, et al. used experimental data to modify PL to account for flow around an antenna; however, more data is needed to fully account for flow and particulate influence on ESD from atmospheric flight.

1.3 Gas Breakdown and Electron Emission Physics

Depending on the gas pressure and gap distance, various mechanisms may drive gas breakdown and electron emission. Figure 1.13 schematically summarizes the key mechanisms and generally shows the influence on gas pressure and gap distance on these mechanisms. Multiple ongoing studies in our research group are theoretically examining these transitions, which is the subject of two other Ph.D. dissertations. A brief summary of the key mechanisms that this dissertation assesses experimentally follows.

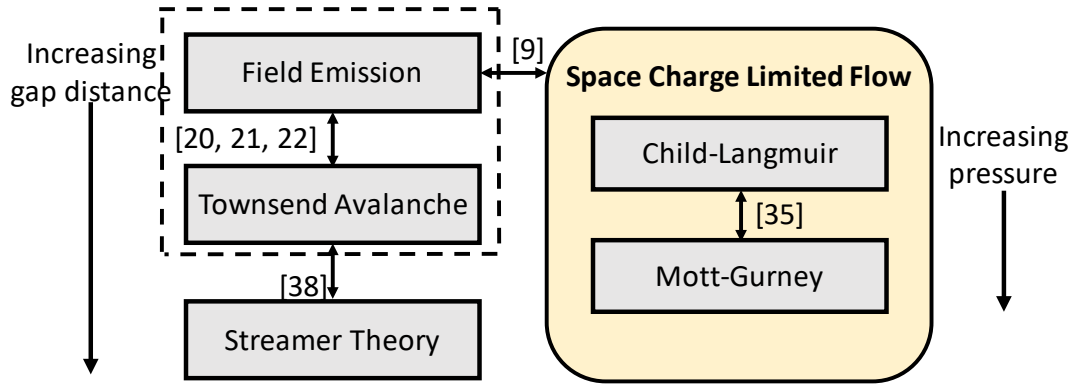


Figure 1.13: Outline of piecemeal connections of various breakdown mechanisms²⁶ Reprinted with the permission of AIP Publishing.

1.3.1 Paschen's Law

Characterizing gas breakdown and electron emission for microscale and smaller devices is important across application and pressure, motivating studies on the responsible physical phenomena. At a certain applied voltage and pressure, a planar diode will experience a flow of current between the electrodes as the gas between them suddenly becomes conductive. This process is referred to as gas breakdown. It occurs due to the creation of electron avalanches started by seed electrons that multiply due to collisions with surrounding gas particles and from secondary emission from the cathode as ions reach it. The first free electrons can come from a few sources such as cosmic rays interacting with gas molecules, random radioactive decay of small amount of radon in the air, or other naturally present radioactive particles. Townsend's theory describes this breakdown process.

Townsend developed a criterion that a free electron near the cathode will create at least one new secondary electron due to its location with vicinity to the cathode. This leads to a sustained discharge across the gap d . The condition for this avalanche to occur in terms of α , known as the first Townsend coefficient, which refers to the rate of ionization events per unit length for electrons having a drift velocity in the direction of the electric field E and γ , the secondary ionization coefficient of the cathode, is given by²⁷

$$\gamma(e^{\alpha d} - 1) = 1, \alpha d = \ln\left(\frac{1}{\gamma} + 1\right). \quad (1.1)$$

An empirical relation for the first Townsend coefficient, given by $\alpha=A_p\exp(-B_p p/E)$, where A_p [$\text{cm}^{-1} \text{Torr}^{-1}$] and B_p [$\text{V}/(\text{cm-Torr})$] are empirically known coefficients, can be used to derive the breakdown voltage V_{br} and electric field E_{br} for a planar diode with gap distance d and pressure p ($E_{br} = V_{br}/d$) as²⁷

$$V_{br} = \frac{B_p p d}{\{\ln(A_p p d) - \ln[\ln(1 + \gamma^{-1})]\}}, \quad (1.2)$$

which is referred to as Paschen' law (PL). However, the values for the constants A_p [$\text{cm}^{-1} \text{Torr}^{-1}$] and B_p [$\text{V}/(\text{cm-Torr})$] are only valid over a certain range of E/p and are not necessarily valid for microscale gaps^{28,29}. The commonly referenced text of Raizer specifies a limit of 700 V/cm/torr as a validity limit²⁷. Plots of V_{br} as a function of pd are known as Paschen curves. Paschen collected experimental data showing obvious minimums exist²⁷. The minimum voltage V_{min} from PL, known as the Paschen minimum, is achieved when

$$(pd)_{min} = \frac{\exp(1)}{A} (\ln \gamma^{-1} + 1), \quad (1.3)$$

which yields

$$V_{min} = \exp(1) \frac{B}{A} (\ln \gamma^{-1} + 1), \quad (1.4)$$

where A and B are empirically fit constants. Gas breakdown is typically driven by Townsend avalanche and predicted by Paschen's law (PL)³⁰. AC breakdown may also be predicted in a slightly different, but related manner³¹.

The ionization coefficient may be better characterized by using 1-D particle-in-cell (PIC)-Monte Carlo collision (MCC) simulations³². The ionization coefficient may be obtained directly from simulations by

$$\alpha = \frac{1}{d} \left[\frac{J_{e,anode}}{J_{e,cathode}} \right], \quad (1.5)$$

where $J_{e,anode}$ is the current density at the anode and $J_{e,cathode}$ is the current density at the cathode. The ionization coefficients were found over a range of E/P exceeding the accepted validity limit for a 100 μm gap for argon gas. The ionization coefficient decreased as predicted. This has potentially applications for magnetrons, where the emission from the wall material is critical in creating oscillations that produce microwaves or RF. A small shift in surface roughness

effecting the field enhancement or a small deviation in voltage could affect the efficiency of the device or lead to failure.

1.3.2 Field Emission Driven Microscale Gas Breakdown

Reducing gap sizes to microscale causes field emission (FE) to drive breakdown^{33–35}. This field emission driven microscale gas breakdown regime is characterized experimentally by the absence of the “Paschen minimum,”³³ or the minimum breakdown voltage V_{br} typically observed when plotting V_{br} as a function of the product of pd . Instead, V_{br} exhibits either an extended plateau or a continued decrease with decreasing d at a constant pressure. While the extended plateau occurs near the transition from the PL to field emission regime, the exact reason why it occurs under certain conditions and not others remains unclear. One contributing factor could be the combination of various aspect ratio nonuniformities on the electrode causing an extended effective Paschen’s curve³⁶. The individual field emission parameters may also impact the transition from FE to PL, leading to the extended plateau, which can be investigated theoretically. One can mathematically predict the behavior of V_{br} by coupling field emission with Townsend avalanche³⁷ and performing a matched asymptotic analysis to derive analytic equations in appropriate limits to demonstrate the transition between the two mechanisms^{26,38,39}. The linear decrease in breakdown voltage for further reductions in gap distance at a constant pressure can be further derived analytically³⁹. Depending upon the pressure and field emission parameters, the linear decrease may occur for gap distances at or above the Paschen minimum or below the Paschen’s minimum, which could give the appearance of an extended plateau⁴⁰.

Field emission occurs due to the quantum mechanical behavior of matter and its interaction with the potential well of the work function of a material. The work function of a material is the energy potential an electron must overcome to break free of the surface of the material. Applying an electric field to a material modified the work function due to the Schottky effect. The Schottky effect modifies the work function to account for image charges and applied electric fields. The modified work function potential due to the Schottky effect is given by⁴¹

$$V_0 = \phi_w - \frac{e^2}{16\pi\epsilon_0 x} - e\epsilon_x x, \quad (1.6)$$

where V_0 is the Schottky modified work function in V, ϕ_w is the work function, e is the electron charge, ϵ_0 is the permittivity of free space, ϵ_r is the relative permittivity of the material, $\epsilon_x = \epsilon_0\epsilon_r$,

and x is the linear distance from the height of the potential barrier to the surface of the metal. The second term on the right hand side of (1.6) modifies the work function for image charges in the system and the third term on the right hand side accounts for the applied electric field. Figure 1.14 shows the Schottky modified work function.⁴¹ The black line in both the left and right diagrams of Figure 1.14 represents the Schottky modified work function potential that has substantially decreased due to the applied electric field. The modified work function also now has a finite width associated with it, and this is where the quantum mechanical distribution of the electron potential comes into play. The wave nature of the electron also creates a spatial distribution.

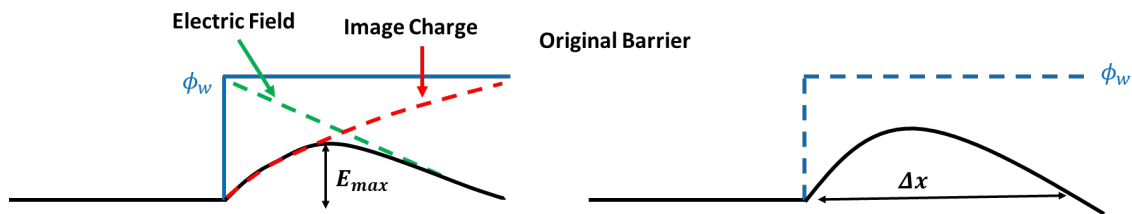


Figure 1.14: Schottky modified work function potential showing finite width.

Figure 1.15 shows that the classical version of an electron would appear as a point, while the quantum mechanical consideration has a spatial distribution that may, in fact, cross the potential width Δx ⁴². The spatial distribution of the electron potential indicates that some portion of the distribution is beyond the potential barrier, giving the electron sufficient energy to escape the surface and move away from the cathode.

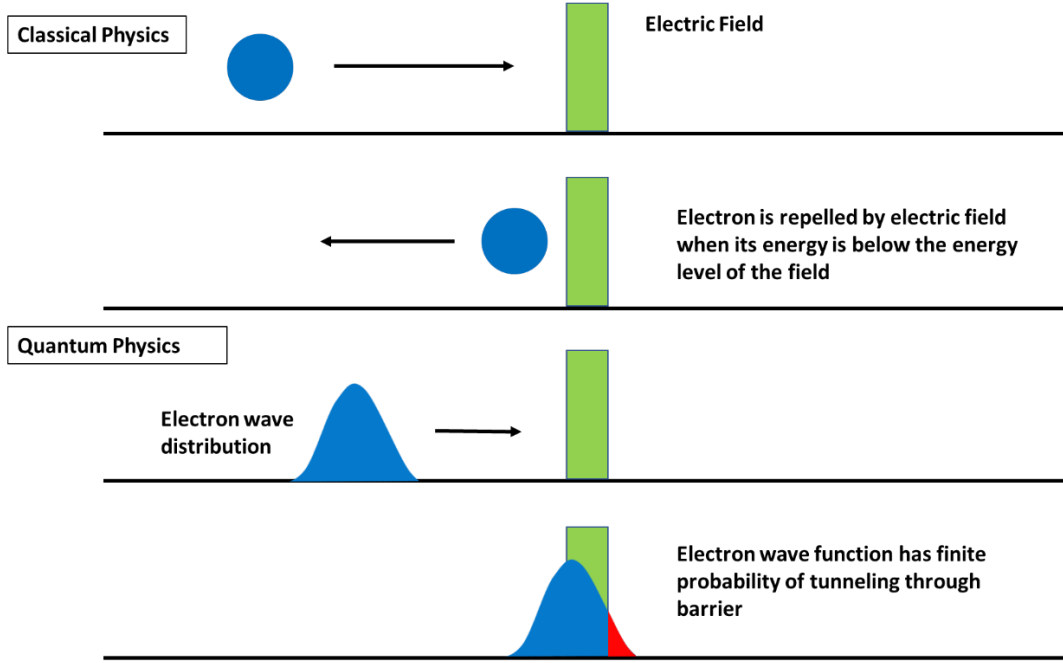


Figure 1.15: Tunneling effect showing how quantum mechanical distribution of electron potential can lead to breaching the potential barrier.

Empirically, the emission of the electrons (current density) is governed by the Fowler-Nordheim equation, given by⁴¹

$$J_{FN} = A_{FN}(\beta V)^2 \exp \left[\frac{-B_{FN}\phi_w^{3/2}}{\beta V} \right] \left[\frac{A}{cm} \right], \quad (1.7)$$

where

$$A_{FN} = 1.42 \times 10^{-6} \frac{1}{\phi_w} \exp \left[\frac{10.4}{\phi_w^{1/2}} \right] \quad (1.8)$$

$$B_{FN} = 6.44 \times 10^7 [\text{Vcm}^{-1}\text{eV}^{-3/2}] \quad (1.9)$$

where β is the field enhancement factor due to sharpness of microfeatures present on the surface of the material and V is the applied voltage.

One of the critical challenges with predicting this behavior at smaller scales is accurately accounting for the contribution of work function and field enhancement factor⁴³, which drive field emission and play the largest role in the sensitivity of predicted V_{br} at microscale⁴⁴. Since changes in surface roughness can impact the presence of sharp features contributing to field enhancement

and localized modifications in electrode structure can modify the work function ⁴⁵, experimentally characterizing the impact of surface roughness for microscale gaps is paramount for extending the validity of the theoretical descriptions^{26,38,39,44}. Studies on the impact of surface roughness on emission in vacuum have experimentally considered the formation of field emission sites for unpolished stainless steel electrodes ⁴⁶, the impact of electrode microtip formation and destruction on field emission driven vacuum breakdown ⁴⁷, and the impact of repeated breakdowns on V_{br} , current at discharge initiation, field enhancement factor, and the current density as a function of the number of breakdown events ⁴⁸.

1.3.3 Space Charge Limited Emission in Vacuum

Further reducing the gap distance can cause electron emission to transition from field emission to space-charge limited emission. Space charge limited emission occurs when the charge accumulated due emitted electron in a vacuum gap becomes so strong that it completely counteracts the applied electric field, limiting further increase in applied current (emission of electrons) from the cathode. This condition occurs when the electric field goes to zero at the cathode.

This limiting current density is given by the Child-Langmuir Law at vacuum^{49,50}. To derive this relationship, we start from Poisson's equation, given by

$$\nabla \cdot \mathbf{E} = \frac{\rho(x)}{\epsilon_0}, \quad (1.10)$$

where ρ is the electron charge density and $\mathbf{E} = -\nabla V$. Substituting this equation for \mathbf{E} gives

$$(\nabla \cdot \nabla V) = \Delta V = -\frac{\rho(x)}{\epsilon_0}. \quad (1.11)$$

Assuming a 1-D, planar geometry gives

$$\frac{d^2V}{dx^2} = -\frac{\rho(x)}{\epsilon_0}. \quad (1.12)$$

Taking into account the space charge distribution and that $\rho(x) = J/v(x)$, where J is the emitted current density and $v(x)$ is the electron velocity as a function of position x , gives

$$\frac{d^2V}{dx^2} = -\frac{J}{\epsilon_0 v(x)} \quad (1.13)$$

for the collisionless case. Using energy conservation and assuming the anode is grounded with the cathode biased at a potential V_0 and electron mass m gives

$$v(x) = \left[\frac{2e(V_0 - V(x))}{m} \right]^{1/2} \quad (1.14)$$

Substituting $v(x)$ into (1.14) gives

$$\frac{d^2V}{dx^2} = -\frac{J}{\varepsilon_0} \left[\frac{m}{2e(V_0 - V(x))} \right]^{1/2} \quad (1.15)$$

For a 1-D, planar diode, J is constant, and we can manipulate (1.15) to obtain

$$\left(\frac{dV}{dx} \right)^2 - \left(\frac{dV}{dx} \right)_0^2 = \frac{4J}{\varepsilon_0} \left[\frac{m(V_0 - V(x))}{2e} \right]^{1/2}. \quad (1.16)$$

At the space-charge limit, the electric field at the cathode is zero, or

$$\left(\frac{dV}{dx} \right)_0 = 0. \quad (1.17)$$

Thus, (1.16) becomes

$$\frac{dV}{dx} = 2 \left(\frac{J}{\varepsilon_0} \right)^{1/2} \left[\frac{m(V_0 - V(x))}{2e} \right]^{1/4}. \quad (1.18)$$

Integrating both sides yields

$$V = V_0 - \left[\frac{3}{2} \left(\frac{J}{\varepsilon_0} \right)^{1/2} \left(\frac{m}{2e} \right)^{1/2} x \right]^{4/3}, \quad (1.19)$$

where e is the charge of an electron. For a gap of distance d and $V(d) = 0$, this becomes

$$V_0 = \left[\frac{3}{2} \left(\frac{J}{\varepsilon_0} \right)^{1/2} \left(\frac{m}{2e} \right)^{1/2} d \right]^{4/3}. \quad (1.20)$$

Solving for J gives the Child-Langmuir law as

$$J_{CL} = \frac{4\varepsilon_0}{9} \left(\frac{2e}{m} \right)^{1/2} \frac{V_0^{3/2}}{d}. \quad (1.21)$$

Measuring the current emitted across the gap as a function of applied voltage gives the required information to measure when the emission regimes have changed. Bhattacharjee and Chowdhury showed this when they examined the transition from Quantum Child-Langmuir to Classical Child-Langmuir to Fowler-Nordheim⁵¹. The method is very simple and requires only fitting the different current emission equations to the voltage to determine the slopes of the plots. The transition from quantum Child-Langmuir to Classic Child-Langmuir occurs at larger V and the slope changes from 1/2 to 3/2 as one would expect from Quantum Child-Langmuir, given by

$$J_{QCL} = \frac{\varepsilon_0 \hbar^2 V^{1/2}}{e^{1/2} m^{3/2} d^4}, \quad (22)$$

where \hbar is the reduced Planck constant. The right portion of Figure 1.16 shows the transition from quantum Child-Langmuir to Classic Child-Langmuir when the curve fits change at larger V and the slope changes from $1/2$ to $3/2$.

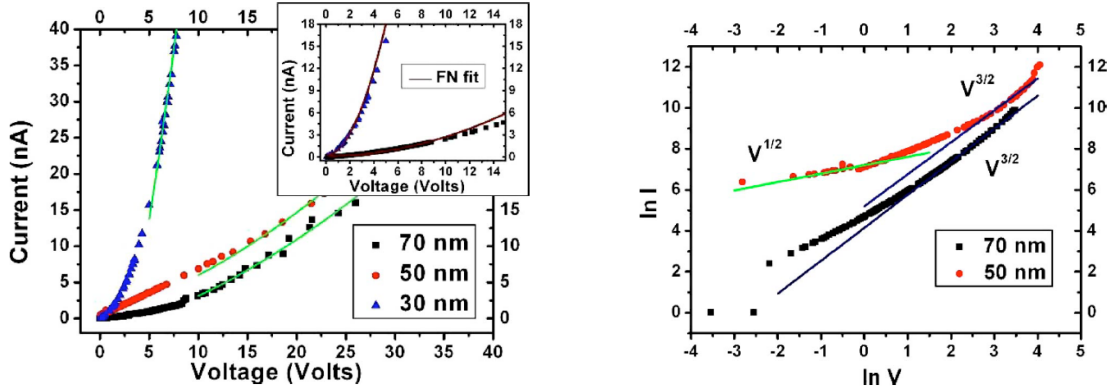


Figure 1.16: Current as a function of voltage showing transition between different emission regimes⁵¹ Reprinted with the permission of AIP Publishing.

Realistic devices are not necessarily one-dimensional. Luginsland, et. al. considered uniform emission of electrons over a finite strip of width W in a planar gap of gap separation D , and extend the classical one-dimensional Child-Langmuir law to two dimensions⁵². The limiting current density in two dimensions $J_{CL}(2)$ in units of the classical one-dimensional value $J_{CL}(1)$, given by (1.21) is a monotonically decreasing function of W/D . Simulations using OOPIC and MAGIC examined the space-charge limit when electrons were emitted only over a finite strip on a planar cathode with and without a large parallel magnetic field B . The simulations results could be fit to

$$\frac{J_{CL}(2)}{J_{CL}(1)} = 1 + \frac{0.3145}{W/d} - \frac{0.0004}{(W/d)^2} \quad (1.23)$$

within 5%. For $W/d = 1$ and 4, the corrections to the 1-D Child Langmuir equation are

$$\frac{J_{CL}(2)}{J_{CL}(1)} = 1 + \frac{0.3145}{1} - \frac{0.0004}{(1)^2} = 1.3141 \quad (1.24)$$

$$\frac{J_{CL}(2)}{J_{CL}(1)} = 1 + \frac{0.3145}{4} - \frac{0.0004}{(4)^2} = 1.0786 \quad (1.25)$$

This matches closely with the data presented in Figures 1 and 2 of Ref. [52]. The authors successfully modified the classical Child-Langmuir law to two dimensions by PIC simulation. The

critical current density only weakly depended on the axial magnetic field that confines the electron flow. The virtual cathode began to form near the central region of the emitting surface, and very close to the surface.⁵³

Considering an emission strip used above as W combined with the gap d raises interesting questions about the effect of geometry on these regimes. If the device (like most real applications) is not a 1-D planar diode, we must account for W . Moreover, one must also account for field enhancement from protrusions or features on the surface of the material at nano- or microscale. Specifically looking at the Fowler-Nordheim equation (1.7), β must account for geometric behavior. Currently, β is often treated as a fitting variable with limited empirical data available^{27,28}. More importantly, the work function ϕ_w appears in multiple locations in the equation. Typically, on the macroscale, ϕ_w is a function of the material since quantum mechanical effects have minimal influence; however, at micro- and nanoscales, quantum effects become important, as shown during the derivation of the Schottky effect. Thus, slight surface irregularities can cause drastic differences in device performance based simply on how sharp a peak or valley may be and if, as previously presented, the surface is modified during operation.

1.3.4 Space Charge Limited Emission with Collisions

These previous studies on the transition from space-charge limited emission to field emission consider vacuum conditions; however, as we have shown above, electron emission is critical for predicting breakdown for microscale and smaller gaps and it is possible that space-charge limited emission may become important in this regime. Alternatively, one may consider vacuum electronics devices with some degree of leakage resulting in “dirty vacuum,” which may lead to divergence from the standard Child-Langmuir law. This necessitates the consideration of space-charge limited emission with collisions as defined by the Mott-Gurney law, given by

$$J_{MG} = \frac{9}{8} \epsilon \mu \frac{V^2}{d^3}, \quad (1.26)$$

where ϵ is the permittivity of the medium and μ is electron mobility. Accounting for electron interactions with the neutral gas by introducing the electron mobility, Darr, et al. derived an exact solution for the current as a function of applied voltage for a given μ and d ⁵⁴. Moreover, they derived asymptotic solutions for FN, CL, and MG in appropriate limits of V , d , and μ to obtain the nexus where two or three of these asymptotes matched. Figure 1.17 shows an example nexus

plot for a given μ . At larger gap distances, electrons may collide with the neutral gas, introducing a MG regime between FN and CL (vacuum). There exists a third-order nexus where all three asymptotes match. At gap distances below this point, FN transitions directly to CL, as in vacuum. For nitrogen, this third order nexus occurs at ~ 250 nm for atmospheric pressure, suggesting that MG may become an important limit to consider as gap distances are reduced submicroscale at atmospheric pressure.

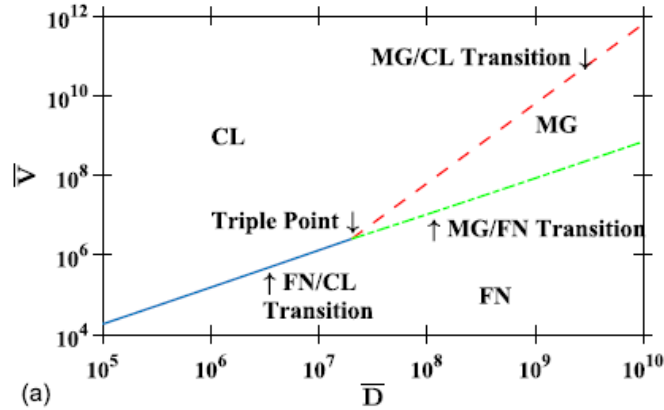


Figure 1.17: Plot of nondimensional voltage and gap size showing a third order nexus between Fowler-Nordheim, Child-Langmuir and Mott-Gurney depending on the gap size and voltage for a given electron mobility⁵⁴ Reprinted with the permission of AIP Publishing.

1.3.5 Streamer Discharges

Although much of this dissertation focuses on going from gap distances corresponding to PL to nanoscale, we briefly touch on the phenomenon going from PL to larger gaps or higher pressures. In this case, discharge formation moves from Townsend avalanche to the Meek criterion, which dictates that when the electric field at the tip of the avalanche from Townsend avalanche is strong enough, it begins to dominate the ionization process²⁹. Meek's criterion states that it is possible to state when the spark is now dominated by the electric field rather than avalanche by considering collision density, or the product of the first ionization coefficient α [collisions/cm] and gap distance d [cm]. When $\alpha d > 18 - 20$ for atmospheric pressure air at $d = 1$ cm, Meek's criterion dictates that the regime has moved into the streamer discharge. Furthermore, experimental observations in a cloud chamber led Meek and Raether to derive another criterion that relates the first Townsend breakdown coefficient and the electric field of the streamer tip by

$$E_r = \frac{5.27 \times 10^{-7} (\alpha e^{\alpha X})}{(X/P)^{1/2}} \left[\frac{\text{V}}{\text{cm}} \right], \quad (1.27)$$

where P is the gas pressure and X is the streamer length and α is the ionization coefficient. The condition when E_r matches the applied electric field and $X = d$ corresponds to Raether's criteria for streamer discharge.

1.3.6 Overview of Dissertation

Electronics in modern society has continued to drive applications to smaller scale and higher electric fields and currents. Typical understanding of how electrical breakdown and plasmas form has been based on semi-empirical models that incompletely describe the process and phenomena at microscale and nanoscale. This has motivated research to characterize the fundamental physics of electrical breakdown at these dimensions to aid into the basic nature of electrical application to nano- and microscale to allow for its controlled use at ever expanding conditions. One important aspect of electrical breakdown is the interaction of nano- and microscale surface properties with surrounding gas causing emission of electrons. Previous experimental and theoretical work has shown that surface roughness could alter breakdown voltage conditions. Experiments from other groups and theory from our group has also demonstrated that gas type and pressure can also alter breakdown mechanisms.

This dissertation hypothesizes that one may predict *a priori* how to tune emission physics and breakdown conditions by altering electrode conditions (sharpness and surface roughness), gap size, and pressure. Specifically, it focuses on the experimental and simulation aspects of this hypothesis to both benchmark theoretical advances in our research group and guide future theoretical studies. Chapter 2 examines the effect of multiple discharges on microscale, atmospheric breakdown voltage, providing the first results demonstrating the effect of surface roughness on this behavior and showing that theory agrees with experimental results when the crater depth is factored into the overall effective gap distance. Chapter 3 reports the design and testing of electron emission and gas breakdown for nanoscale gaps at atmospheric pressure. While microscale gaps exhibit a transition from field emission to gas breakdown, this Chapter reports for the first time that nanoscale gaps may exhibit a transition from either field emission or space-charge limited emission to gas breakdown at various gap distances. These results demonstrate the sensitivity of emission mechanisms to slight device construction or external conditions at these

smaller gap distances, motivating further studies into these parameters. Chapter 4 reports the results of particle-in-cell simulations for extending the empirical relationship for α to the relevant parameter range for nano- and microscale gas breakdown. Contemporary microscale (and now nanoscale) experiments violate the ranges of electric field and pressure for which traditional semi-empirical relationships for α are valid. The simulations conducted directly calculate α from the current density in systems with various nanoscale and microscale parameters and pressures of relevance for these experiments. The resulting database will ultimately provide new relationships for α over a wide range of electric fields and pressures to provide more accurate theories for breakdown. Chapter 5 provides concluding remarks and makes recommendations for future experiments to account for other emission mechanisms such as thermionic emission.

2. THE IMPACT OF CATHODE SURFACE ROUGHNESS AND MULTIPLE BREAKDOWN EVENTS ON MICROSCALE GAS BREAKDOWN AT ATMOSPHERIC PRESSURE

Reproduced from R.S. Brayfield, A.J. Fairbanks, A.M. Loveless, S. Gao, A. Dhanabal, W. Li, C. Darr, W. Wu, and A.L. Garner, *J. Appl. Phys.* **125**, 203302 (2019)., with the permission of AIP Publishing

2.1 Background and Motivation

Miniaturization of electronic components constantly drives innovation in multiple fields, motivating studies of the behavior of electric breakdown and gas discharges at microscale^{2,33}. The increased use of microsattellites has led to the development of electric micropropulsion to better control them^{55,56}. This further motivated the design of chemically reactive, non-reactive, and plasma thrusters, which all suffer from the challenge of applying sufficient energy to the system to alter the propellant without damaging the circuitry used in these micro to nanoscale devices⁵⁷. For microplasma thrusters, the challenge becomes inducing breakdown for propulsion while protecting the devices producing the plasma from excessive damage⁵⁷. A similar challenge arises when developing microplasma systems for biomedical applications⁵⁸.

In electronics, one ideally avoids creating discharges, or electrical breakdown. Even for commercializing compact pulsed power systems, one must account for the potential of discharges or arcing that may be detrimental to safe and effective operation. For instance, a recent study that developed a flexible, compact pulsed power system for biomedical applications specifically considered the impact of arcing across electrodes not completely covered by the liquid biological sample on device design⁵⁹. While these systems typically use gap lengths on the order of millimeters⁵⁹, other applications apply electric pulses to sub-millimeter gaps⁶⁰, motivating understanding of breakdown in both liquid⁶¹ and gases at these size scales. Electronics designed specifically at these sizes, such as microelectromechanical systems (MEMS), are increasingly used in biotechnology, medicine, and communications²². Continuing reduction in the size of MEMS increases the importance of preventing breakdown between their nanofabricated components. Nanoelectromechanical systems (NEMS) are increasingly examined for sensing and scanning²² with common uses including electronic displays, printers, airbags, and many new MEMS systems. As relevant device sizes transition from microscale to nanoscale, electron emission may shift from

field emission to space-charge limited emission^{54,62}, motivating additional studies on gas breakdown at smaller scale. These phenomena also have significant implications in vacuum electronics, where ongoing research in electron sources^{63,64} has focused on assessing groups of nanoemitters^{65,66} and intentionally modifying device designs to better control field enhancement⁶⁷.

Thus, characterizing gas breakdown and electron emission for microscale and smaller devices is important across application and pressure, motivating studies on the responsible physical phenomena. Gas breakdown is typically driven by Townsend avalanche and predicted by Paschen's law (PL)³⁰; however, reducing gap sizes to microscale causes field emission to drive breakdown³³⁻³⁵. This field emission driven microscale gas breakdown regime is characterized experimentally by the absence of the "Paschen minimum,"³³ or the minimum breakdown voltage V_b typically observed when plotting V_b as a function of the product of gas pressure p and gap distance d , or pd . Instead, V_b exhibits either an extended plateau or a continued decrease with decreasing d at a constant pressure. While the extended plateau occurs near the transition from the PL to field emission regime, the exact reason why it occurs under certain conditions and not others remains unclear. One contributing factor could be the combination of various aspect ratio nonuniformities on the electrode causing an extended effective Paschen's curve³⁶. The individual field emission parameters may also impact the transition from FE to PL, leading to the extended plateau, which can be investigated theoretically. One can mathematically predict the behavior of V_b by coupling field emission with Townsend avalanche³⁷ and perform a matched asymptotic analysis to derive analytic equations in appropriate limits to demonstrate the transition between the two mechanisms^{26,38,39}. The linear decrease in breakdown voltage for further reductions in gap distance at a constant pressure can be further derived analytically³⁹.

One of the critical challenges with predicting this behavior at smaller scales is accurately accounting for the contribution of work function and field enhancement factor⁴³, which drive field emission and play the largest role in the sensitivity of predicted V_b at microscale⁴⁴. Since changes in surface roughness can impact the presence of sharp features contributing to field enhancement and localized modifications in electrode structure can modify the work function⁴⁵, experimentally characterizing the impact of surface roughness for microscale gaps is paramount for extending the validity of the theoretical descriptions^{26,38,39,44}. Studies on the impact of surface roughness on emission in vacuum have experimentally considered the formation of field emission sites for

unpolished stainless steel electrodes⁴⁶, the impact of electrode microtip formation and destruction on field emission driven vacuum breakdown⁴⁷, and the impact of repeated breakdowns on V_b , current at discharge initiation, field enhancement factor, and the current density as a function of the number of breakdown events⁴⁸.

This study examines the impact of surface roughness and multiple breakdowns on V_b and the electrode surfaces by using a setup comprised of a small tungsten needle placed a few microns from a copper plated sample based on one used previously to assess atmospheric pressure, field emission driven microdischarges⁶⁸. For fixed gap distances of $1 \pm 0.5 \mu\text{m}$, $5 \pm 0.5 \mu\text{m}$, and $10 \pm 0.5 \mu\text{m}$, we measured breakdown voltage and current for a single and ten breakdown events, noting the general increase in breakdown voltage for repeated breakdown events, as observed in Ref [48]. This study places these results in the context of electrode modification and surface roughness by using atomic force microscopy (AFM) and light microscopy to show that breakdown events create craters on the cathode with depths (3-40 μm) that may be significant compared to the interelectrode gap distance (1, 5, and 10 μm), contributing to increased V_b . To our knowledge no microscale experiments have demonstrated the impact of multiple breakdown event induced craters on V_b . Section 2.2 outlines the materials and methods used in this study. Section 2.3 summarizes the experimental results. We apply microscale gas breakdown theory based on asymptotic analysis to demonstrate the transitions in breakdown mechanisms in Section 2.4. Section 2.5 discusses the results and provides concluding remarks.

2.2 Materials and Methods

2.2.1 Materials

The setup consists of tungsten dissection needles (Roboz Surgical Instrument Co., RS-6065) mounted into polyethylene to ensure electrical isolation. The copper plates were mounted to polyethylene blocks mounted to a micromanipulator and moved in increments of 1 μm . Figure 2.1 shows a circuit schematic of the micromanipulator setup with a fixed pin electrode.

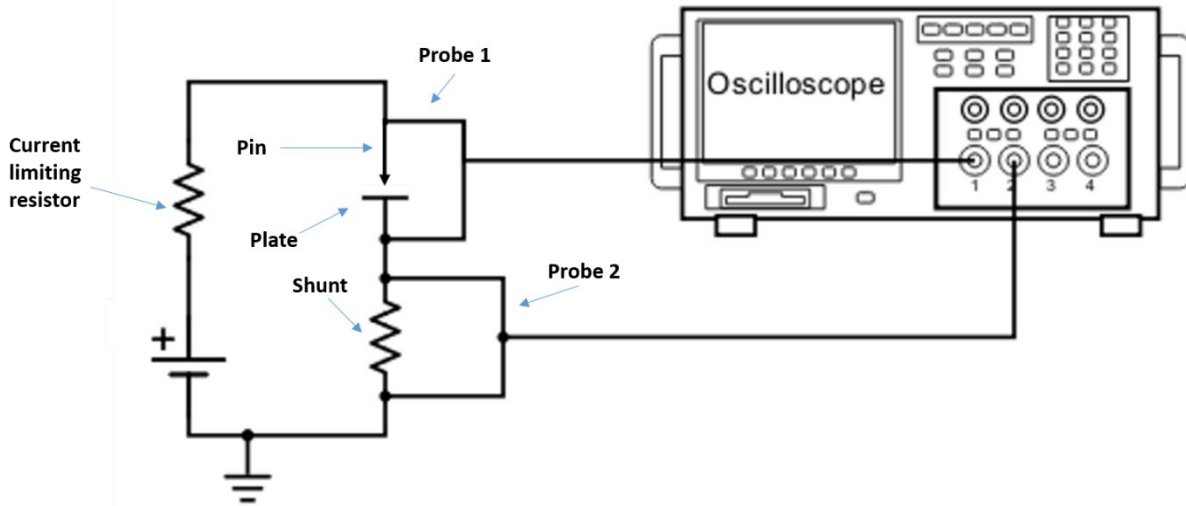


Figure 2.1: Circuit schematic of the experimental setup with a pin to plate configuration to test samples.

The copper (Fire Mountain Gems, H20-9336FX) was cut into 12.7 mm² plates that were then polished to various degrees of surface roughness by using a wet polishing station with 400, 800, and 1200 grit polishing pads (Pace Technologies). After polishing, we soaked the plates in acetone to remove any surface contamination and rinsed them with water to remove any residue. AFM was then conducted to verify the absence of residue or polishing particulate on the surfaces. Table I reports the surface conditions under these initial AFM tests. A wire was soldered onto the back of the copper plate to provide electrical connections. Voltage and current measurements were made using an oscilloscope and two 100:1 voltage probes. One probe was connected across the pin to plate gap to measure the gap voltage and the second across a 1 M Ω resistor to determine the current. With the copper plate as the ground (cathode) and the tungsten needle as the “hot” electrode (anode), we used a high voltage supply (Stanford Research System, PS365, 10 kV) to apply DC voltage until discharge formation.

2.2.2 Methods

We divided each copper plate into sections for single breakdown event testing, ten breakdown event testing, and sample handling. We tested cathodes polished with each grit in triplicate for statistical purposes. We set the gap distance by applying 35 V to create a bias and using the micromanipulator to move the plate until it softly contacted the needle to create a “short”

in the circuit before withdrawing the plate to the desired gap distance. This method was previously used to calibrate needle electrode distance with no effect on the surface⁶⁸. To determine whether the contact phase of the setup damaged the surface, we used the micromanipulator to force a needle electrode into the surface. AFM was used to verify no significant change to the electrode surface was measurable. We considered gap distances of $1 \pm 0.5 \mu\text{m}$, $5 \pm 0.5 \mu\text{m}$, and $10 \pm 0.5 \mu\text{m}$ between the needle and the copper plate. Voltage was ramped at approximately 3 V/s from 100 V to breakdown, where an oscilloscope recorded the breakdown voltage and current waveforms. We removed the voltage immediately following the oscilloscope trigger to prevent further breakdown events. Since no current was present before breakdown, there was no voltage across the 1 M Ω resistor prior to breakdown, so this voltage served as an indication of breakdown. We collected voltage and current waveforms for each breakdown event to compare breakdown voltage across events. Breakdown for these tests was defined as the movement of electrons across the gap, creating a sustained dielectric breakdown of the gas. The current was limited using a ballast resistor to prevent damage to the anode and prevent large currents across the gap that would damage the tip. We observed no damage to the tungsten tips. The discharge event was measured by a shunt resistor that allowed us to monitor the current. When the current across the gap was detected by the oscilloscope, we immediately turned off the power supply to ensure that we only created a single breakdown event at a time. For the ten breakdown experiments, we waited one minute after each breakdown event before repeating. The relative humidity varied from 38-50% during the course of experiments.

We used atomic force microscopy (AFM) to quantify the change in surface roughness by measuring the average height of surface features before and after the breakdown events. Some breakdown induced surface features were too deep for AFM analysis and were estimated by altering the depth of field of an optical microscope to observe when the bottom of the feature was in focus compared to the surface.

2.3 Experimental Results

2.3.1 Cathode Surface Changes

Figure 2.2 shows the representative AFM data for the 800 grit polished cathode prior to breakdown experiments using a 5 μm gap. The optical images of the surface, such as Figure 2.2(a),

show the general roughness of the surface. Figure 2.2(b) shows the contour map of the 800 grit sample with a maximum surface height of 200 nm and crater depth of 200 nm. Figure 2.2(c) shows the AFM tip deflection that measures the surface feature height. This was repeated for each sample to characterize the average surface features before the breakdown experiments. Table 2.1 presents the initial average surface feature height for the samples before breakdown events along the red dashed line in Figure 2.2(b). The data in Table I was taken by averaging all of the peak to peak and RMS values for each grit.

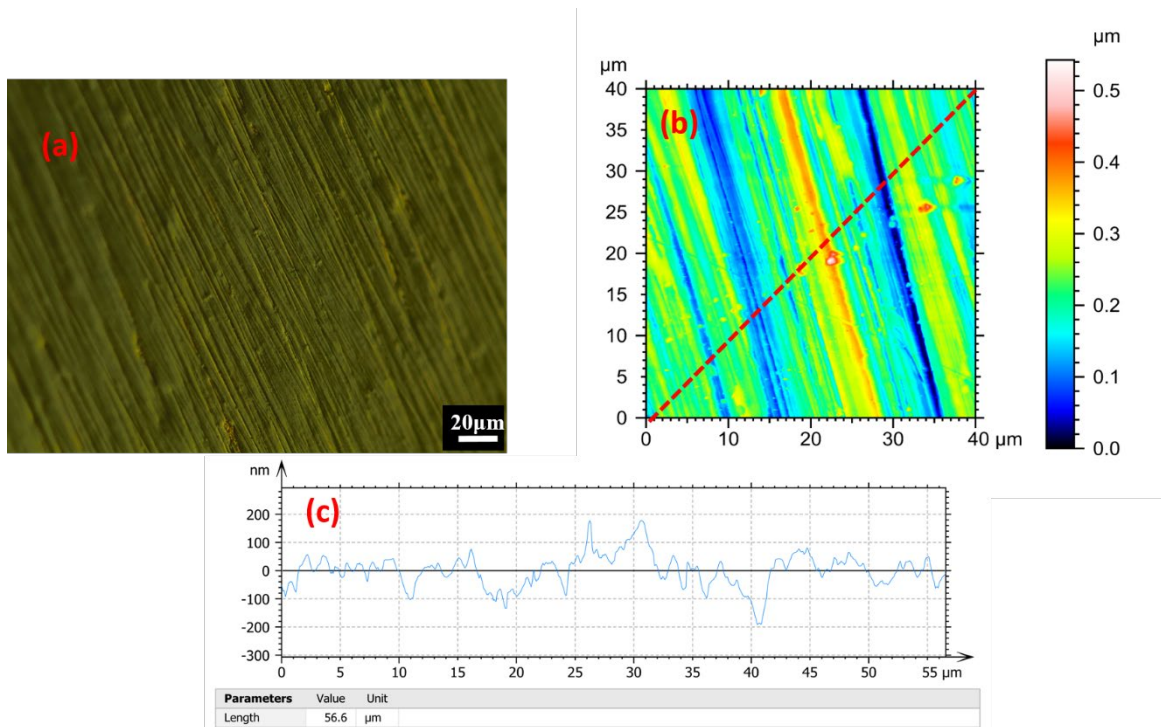


Figure 2.2: Atomic force microscopy (AFM) measurements of the 800 grit cathode prior to experiments showing the average surface features (a) Optical image of the surface visually showing the surface roughness. (b) Contour mapping of surface height along the surface. (c) AFM arm deflection showing height and depth of the surface features.

Table 2.1: Average surface features before breakdown tests.

Grit	Number of samples	Peak to Peak	Standard Deviation (μm)	RMS (nm)
		Average (μm)		
400	9	1.47	1.08	535.22
800	9	0.26	0.18	65.99
1200	9	0.24	0.23	39.48

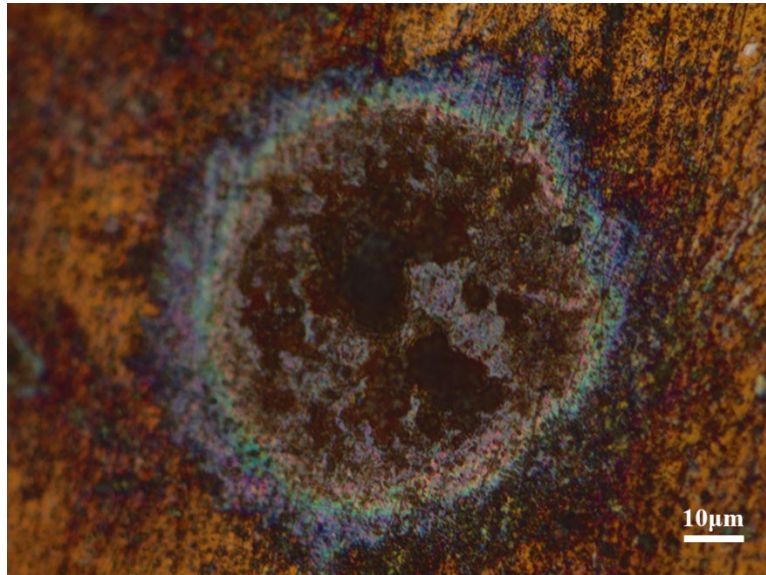


Figure 2.3: Observed ablated region on the cathode after ten breakdown events for a 5 μm gap with the cathode polished using 800 grit, demonstrating the crater formed in the surface.

The breakdown events created small circular ablations on the samples at the test site. Figure 2.3 shows an optical image of an example ablated feature for a cathode polished using 800 grit exposed to ten breakdown events at a 5 μm gap distance. The ablation depth ranged from 3 to 50 μm and is reported in Table 2.2 for all samples containing them. The depth was so great that the samples could not be measured using AFM to quantify the surfaces without damaging the AFM tips. These results indicate that breakdown can cause significant surface modification, ablating material from a localized spot. Furthermore, the ablation depth is greatest for the cathodes with the largest average surface height (400 grit polished cathodes), which would be anticipated to have the highest

field enhancement and, thus, be more susceptible to field emission driven breakdown. This suggests that the concentration of the discharges at the locations of higher surface height for the cathodes polished with 400 grit causes greater cathode damage compared to the 800 and 1200 grit samples, whose surface features are less sharp and will cause less field enhancement.

Table 2.2: Depth of the observed craters at the breakdown voltage for the cathodes polished at each grit where measurable ablation occurred.

Grit (gap distance)	Depth (μm)	Grit (gap distance)	Depth (μm)	Grit (gap distance)	Depth (μm)
400 (10 μm)	9.7	800 (5 μm)	6.2	1200 (1 μm)	12.1
400 (10 μm)	6	800 (5 μm)	7.4	1200 (1 μm)	3.5
400 (10 μm)	13.5	800 (5 μm)	12.4	1200 (10 μm)	4.8
400 (5 μm)	41.2	800 (5 μm)	5.3	1200 (10 μm)	5.4
400 (5 μm)	19.6	800 (5 μm)	5.2		
400 (1 μm)	42.5				

To determine the effect of the contact phase of the setup, we used the micromanipulator to force a needle electrode into the surface. AFM was used to verify no significant change to the electrode surface was measurable. The resulting absence of a circular mark indicated that the breakdown events, and not needle placement, damaged the surface. The absence of these marks on some samples following breakdown indicated that slight variations in surface polishing, which could influence the initial presence of surface structures, could sufficiently alter discharge path and subsequent surface ablation.

2.3.2 Changes in Breakdown Voltage

Figure 2.4 shows a representative waveform for a single breakdown event and the tenth breakdown event for a $5 \pm 0.5 \mu\text{m}$ gap distance with the cathode polished using 800 grit. The voltage remains relatively constant until breakdown occurs, as expected for an applied DC voltage. The breakdown voltage following the tenth event exceeded that for a single event, as shown in

Figure 2.6. In this case, the first breakdown event occurred at 434.85 V while the tenth breakdown occurred at 523.25 V.

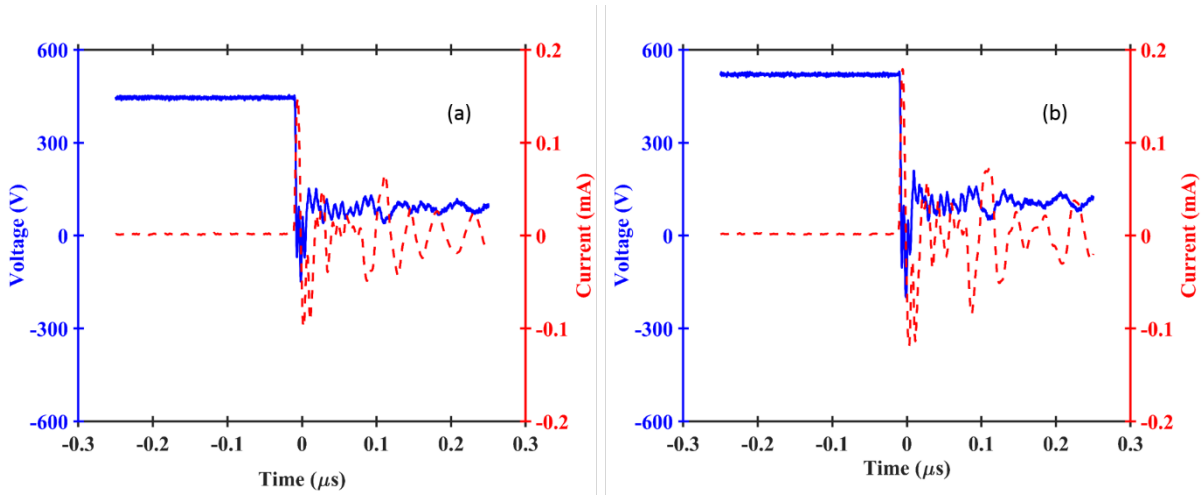


Figure 2.4: Representative voltage (solid) and current (dashed) waveforms for a $5 \pm 0.5 \mu\text{m}$ gap with the cathode polished using 800 grit for (a) a single breakdown event and (b) the tenth breakdown event. All breakdown events exhibited similar characteristics.

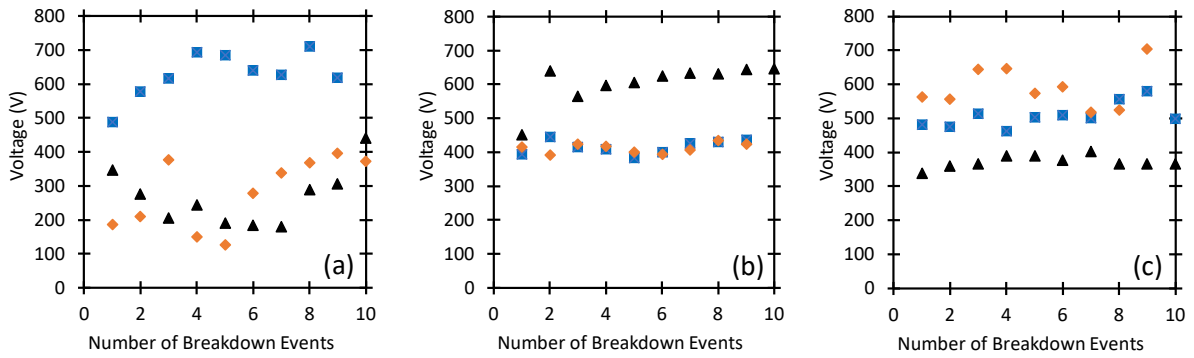


Figure 2.5: Breakdown voltage as a function of number of breakdown events for three individual trials for (a) 400 grit (b) 800 grit and (c) 1200 grit samples at $1 \mu\text{m}$ gap distance.

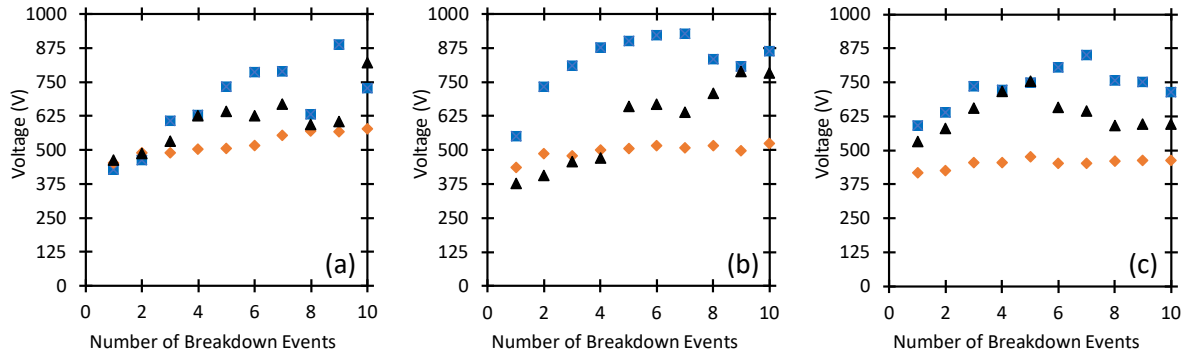


Figure 2.6: Breakdown voltage as a function of number of breakdown events for three individual trials for (a) 400 grit (b) 800 grit and (c) 1200 grit samples at 5 μm gap distance.

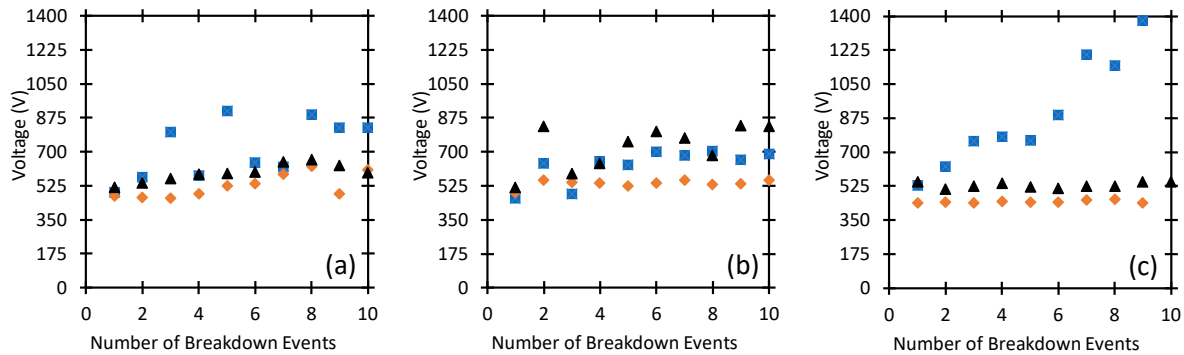


Figure 2.7: Breakdown voltage as a function of number of breakdown events for three individual trials for (a) 400 grit (b) 800 grit and (c) 1200 grit polished cathodes at 10 μm gap distance.

Figure 2.5 Figure 2.7 report the individual replicates for breakdown voltage as a function of the number of breakdown events for a 1, 5, and 10 μm gap with cathodes polished using 400, 800, and 1200 grit disks. Note that we did not achieve three repetitions for a few of the ten breakdown event cases due to either reaching high voltages for larger gap distances or slight sensitivity to micromanipulator position for smaller gap distances. Figure 2.8 reports the average values for a given grit. Generally, breakdown voltage increases with subsequent breakdown events, although this difference is not monotonic and noticeable variation occurs between samples.

Because the craters make noting distinct differences challenging, we ran a general linear model analysis of variance (ANOVA) with stepwise backward elimination to identify the statistically significant difference in means based on voltage as the response for each breakdown event (Minitab 18 software). Anderson-Darling normality tests showed no significance (p -values

> 0.05), indicating normal distribution of residuals, except for the ninth pulse, which likely arises due to some outliers in our experimental dataset when reaching the limit of the micromanipulator travel tolerances. The ANOVA was followed by a Tukey pairwise comparison test at the 95% confidence level and adjusted p -values are reported due to the need for multiple comparisons. Grit did not exhibit any significance for any of the tests. Gap showed significant differences in means for voltage after at least five breakdown events ($p < 0.05$). Table 2.3 summarizes the adjusted p -values from the Tukey tests for significance. Breakdown voltages for 1 μm gap after at least five breakdown events differ statistically significantly from either the 5 μm and 10 μm gaps while the breakdown voltages following the fifth breakdown event for the 5 μm and 10 μm gaps do not exhibit any statistically significant difference.

Table 2.3: Adjusted p -values from Tukey tests comparing breakdown voltage for 5 μm and 1 μm gaps, 10 μm and 1 μm gaps, and 10 μm and 5 μm gaps for the fifth through tenth breakdown events. Conditions undergoing a statistically significant change are denoted with *. Generally, breakdown events after the fifth event yield a statistically significant breakdown voltage between the 1 μm gap and the other gap distance while no statistically significant difference arises between the 5 μm and 10 μm gaps.

Breakdown Event	Difference between 5 μm and 1 μm	Difference between 10 μm and 1 μm	Difference between 10 μm and 5 μm
5	0.015*	0.038*	0.914
6	0.017*	0.044*	0.900
7	0.036*	0.035*	1.000
8	0.141	0.026*	0.693
10	0.002*	0.005*	0.988

This behavior arises because the breakdown events alter the electrode surface, which also contributes to the increased variation after multiple events. First, each breakdown ablates the sharp-tipped features that contribute to field enhancement meaning that the applied voltage (and, thus, the electric field) for subsequent breakdown events must exceed the breakdown voltage for the initial event. The breakdown events additionally create craters on the surface that increase the effective gap distance, as shown by comparing Table 2.1 and Table 2.2, further increasing the applied voltage to achieve the electric field necessary for breakdown. Thus, we anticipate that the

combination of these phenomena will cause a general increase in breakdown voltage for subsequent breakdown events. This trend may not necessarily be monotonic since changes to the electrode surface structure (both electrode depth and field enhancement factor) may vary from event to event and across samples.

This suggests that the change in effective gap distance induced by crater formation plays a dominant role in breakdown voltage for multiple events. Table 2.4 shows that the crater depth is highest for the smallest gap distances, where field emission tends to drive breakdown^{33,39,43,44}, and for the cathode (400 grit) with the sharpest surface features, which would initially provide greater field enhancement to further drive field emission. Thus, we anticipate that the discharges under these conditions would focus on the sharp emitters during repeated breakdowns, resulting in greater cathode damage characterized by larger craters. These larger craters would create an increased effective gap distance, which also corresponds to a higher field enhancement factor in the combined field emission/Townsend avalanche regime since field enhancement increases with increasing gap distance in this regime⁶⁸. Eventually, these larger effective gap distances could also lead to a transition in breakdown mechanism from field emission to Townsend avalanche. Section 2.4 applies an asymptotic theory for microscale gas breakdown to confirm this hypothesis and quantify the contributions of the phenomena involved.

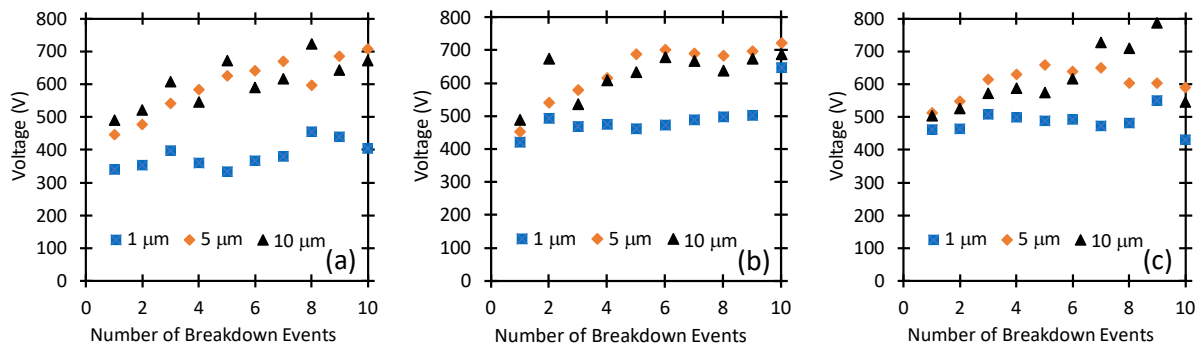


Figure 2.8: Average breakdown voltage as a function of number of breakdown events for (a) 400 grit (b) 800 grit and (c) 1200 grit for three trials each.

Figure 2.8 shows larger gap sizes did not always result in higher breakdown voltage, as one would intuitively expect. The variation in breakdown voltage is likely due to the crater formation, which leads to a larger effective gap. Table 2.4 presents the average crater depths for the conditions where craters occurred. Since this experiment only considered conditions after either a single breakdown

event or after ten breakdown events, we did not record information on crater formation for intermediate conditions (i.e., the exact number of events when crater formation occurred).

Table 2.4: Average crater depth and breakdown voltage after the tenth breakdown event.

Grit	Starting Gap Distance (μm)	Average Crater Depth (μm)	Average Breakdown Voltage for 1 st Event (V)	Average Breakdown Voltage for 10 th Event (V)
400	1	42.5	339	405
400	5	30.4	446	707
400	10	9.73	491	672
800	5	7.3	454	723
1200	1	7.8	462	432
1200	10	5.1	504	545

2.4 Theoretical Assessment

Table 2.4 summarizes the average crater depth for various grits and initial gap distances, along with the average breakdown voltage following the first and tenth breakdown events. Strictly speaking, we would need the crater depth after the ninth breakdown event to calculate the average breakdown voltage after the tenth event; however, the data indicates relatively slight variation between the breakdown voltage for the ninth and tenth events, so we use this crater depth for these calculations. Applying an “effective gap distance” that combines the initial gap distance with the crater depth allows us to assess the transition in breakdown mechanisms with crater formation, analogous to our previous theoretical studies.^{26,38,39,44} It is critical to point out that applying the theory to the *raw* data from Figure 2.5 to Figure 2.8 would lead to large variations in the fitting parameters; however, accounting for the crater depth using Table 2.2 dramatically reduces the relative error of the gap distances (particularly compared to the raw data), enabling the application of the theory.²⁷ While variation clearly remains (which motivated the study from Ref. [44], we

apply the theory here to clearly emphasize the behavior of breakdown voltage as a function of gap distance and the transitions in breakdown regime that we have observed elsewhere.²⁵

Table 2.5: Summary of parameters used in the theoretical analysis.

Parameter	Name	Value	Unit
ϕ	Work function	4.7	eV
ϕ_*	Work function scale	96.81	eV
d	Gap distance	Variable	m
L	Gap distance scale	3.92×10^{-12}	m
p	Pressure	760	Torr
p_*	Pressure scale	1.70×10^8	Torr
E	Breakdown electric field	Variable	V/m
E_*	Breakdown electric field scale	6.20×10^{12}	V/m
V	Breakdown voltage	Variable	V
V_*	Breakdown voltage scale	24.3	V
T	Temperature	300	K
T_*	Temperature scale	7976	K
β	Field enhancement factor	Variable	N/A
γ_{SE}	Secondary emission coefficient	10^{-5}	N/A

We start from our previously-derived universal gas breakdown model,²⁶ given by

$$\frac{\exp[\bar{\phi}^{3/2}/(\beta\bar{E})]}{\beta\bar{\phi}^{1/2}\exp(\bar{\phi}^{-1/2})}\sqrt{\frac{\bar{T}\bar{E}}{\bar{p}\bar{d}_{eff}^2}}\frac{\{1-\gamma_{SE}[\exp(\bar{\alpha}\bar{d}_{eff})-1]\}}{\exp(\bar{\alpha}\bar{d}_{eff})-1}=\exp(1)(1+2\bar{E}), \quad (2.1)$$

where $\bar{E} = E/E_*$ is the dimensionless breakdown field, $\bar{d}_{eff} = \bar{d} + \bar{\delta} = (d + \delta)/L$ is the effective dimensionless gap distance with \bar{d} the dimensionless electrode gap distance and $\bar{\delta}$ the dimensionless crater depth, $\bar{\phi} = \phi/\phi_*$ is the dimensionless work function, $\bar{p} = p/p_*$ is the dimensionless pressure, $\bar{T} = T/T_*$ is the dimensionless gas temperature, and Table V defines all other parameters and provides typical values.

We numerically solve (2.1) for \bar{E} and apply $V = \bar{E}\bar{d}_{eff}E_*L$ to obtain the breakdown voltage in volts using β as a fitting parameter. Furthermore, since the product of the ionization coefficient α and d exceeds unity (specifically, $1.1 < \bar{\alpha}\bar{d}_{eff} = \bar{p}\bar{d}_{eff}\exp(\bar{p}\bar{d}_{eff}\exp(-1)) < 50$, where $\bar{\alpha}=\alpha L$), we apply the analytic equation for breakdown voltage for $\bar{\alpha}\bar{d} \gg 1$, given by [69]

$$V = (E_*L\bar{d}_{eff}/\Lambda_2)\left[-\Delta_2 - (\Delta_2^2 - 2\Lambda_2\bar{\phi}^{3/2}/\beta)^{1/2}\right], \quad (2.2)$$

where $\Delta_2 = -[\bar{\mu} + \bar{\nu}]$ and $\bar{\mu} = \ln(\Lambda_2)/2 + \ln(\beta\bar{\phi}^{1/2}) + \bar{\phi}^{-1/2} + 3/2$ and $\bar{\nu} = \ln\{\exp[\bar{p}\bar{d}_{eff}\exp(-1)] - 1\} - \ln\{1 - \gamma_{SE}[\exp(\bar{p}\bar{d}_{eff}\exp(-1))]\} - \ln[\bar{T}\bar{p}^{-1}\bar{d}_{eff}^{-2}]/2$

represent the field emission and Townsend contributions, respectively, and $\Lambda_2 = 10^{-5}$ is a fitting parameter. Figure 2.9 shows the experimental results (correcting for effective gap distance, which means that many of these points are individual points from Table 2.2), the calculations from (2.1) and (2.2), and the values of $\bar{\alpha}\bar{d}_{eff}$ (note that $\bar{\alpha}\bar{d}_{eff} = \alpha d_{eff}$ since both quantities are scaled by L). Note that several d_{eff} have multiple data points due to crater formation changing d_{eff} under various conditions. From Meek's criterion⁷⁰, $\bar{\alpha}\bar{d}_{eff} \approx 18$ corresponds to the transition to streamer formation, making (2.1) and (2.2) no longer valid (in fact, (2.2) is unsolvable for these points). Although we have addressed this limitation to this theory in previous studies^{26,38,39}, this experimental condition is unique in that we start in the field emission regime and then transition to the Townsend and streamer regimes without changing the physical gap distance. Current theory does not address the transition to streamer discharge at microscale, so we note the potential

transition in the current study. The results of (2.1) and (2.2) differ by $\sim 10\%$ except for the two largest gap distances where $\bar{\alpha}d_{eff} > 18$ and (2.2) cannot be solved.

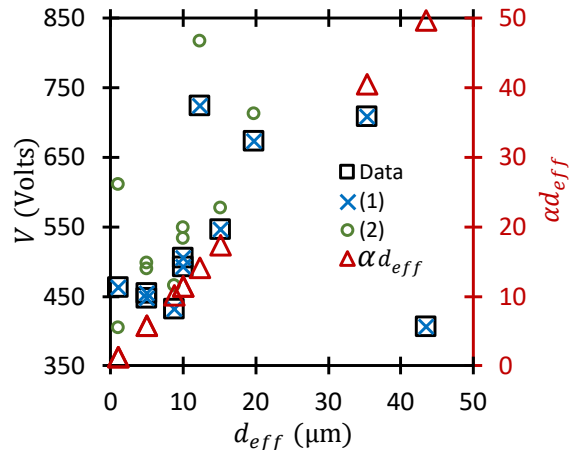


Figure 2.9: Average breakdown voltage, V , as a function of effective gap distance, $d_{eff} = d + \delta$, where d is the anode-cathode gap and δ is the breakdown induced crater depth, compared to numerical results from (2.1) and analytic results from (2.2). The product of the ionization coefficient and effective gap distance, αd_{eff} , is displayed on the secondary vertical axis as a function of d_{eff} . The largest two gap distance points have $\alpha d_{eff} \gg 18$, which exceeds Meek's criterion for streamer formation.

Figure 2.10(a) shows β for fitting the model to experimental data. Interestingly, β varies linearly with d_{eff} until the largest gap distances, excluding the outlier at $d_{eff} \approx 12 \mu\text{m}$. At the largest gaps, β becomes approximately constant. This behavior is similar to our previous application of this theory to experimental results for single breakdown events at microscale, where β increased linearly until Townsend avalanche began to dominate³⁹. Furthermore, the transition from linear to constant β occurs approximately when $\bar{\mu} = \bar{v}$, or when breakdown begins to transition from field

emission to the traditional Paschen law^{30,43,44,71}. Figure 2.10(b) shows that $\alpha d_{eff} \approx 10$ at this transition.

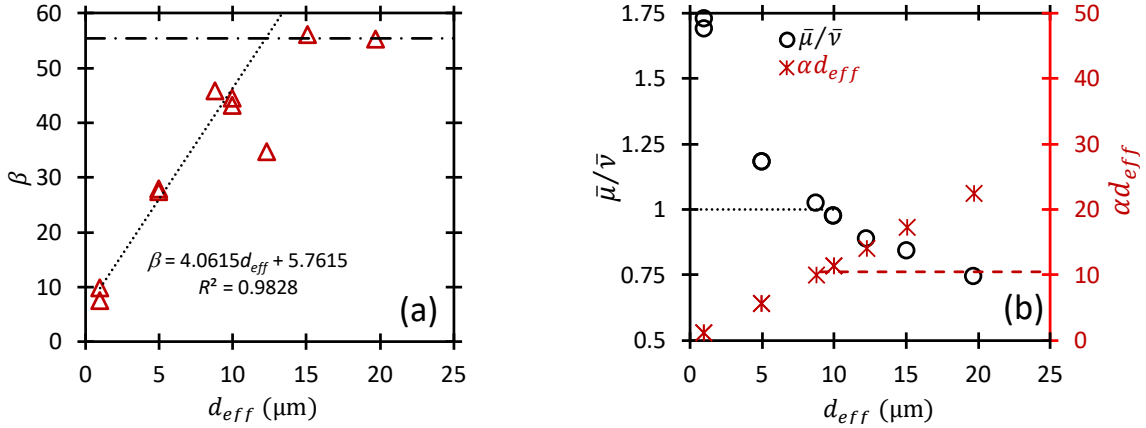


Figure 2.10: (a) Field enhancement factor, β , as a function of effective gap distance, $d_{eff} = d + \delta$, where d is the gap distance and δ is the crater depth, showing that β is approximately linear until the larger gap distances corresponding to the transition to Townsend avalanche, where it becomes constant. (b) The ratio of the field emission component to the Townsend component, $\bar{\mu}/\bar{\nu}$, as a function of d_{eff} , demonstrating that field emission effects govern breakdown until $d_{eff} \approx 10 \mu\text{m}$, which corresponds to $\alpha d_{eff} \approx 10$. This point coincides with the transition of β from linear to constant in (a), indicating the transition to the traditional Paschen's law.

Upon transition to Paschen's law, the experimental data and numerical results from (1) agree well with the universal Paschen's law (UPL)²⁶, given by

$$V = \frac{(\bar{p}\bar{d}_{eff})}{\ln(\bar{p}\bar{d}_{eff}) - \ln[\ln(1 + \gamma_{SE}^{-1})]} (E_*L). \quad (2.3)$$

Figure 2.11 shows the experimental results, the numerical results from (2.1), and the results of (2.3) using $\gamma_{SE} = 1.5 \times 10^{-3}$, which we selected based on previous studies^{26,44,72} and agreement with the experimental data. The calculations from (2.1) for the asymptotic solution match (2.3) for the UPL when $\alpha d_{eff} \approx 10$, corresponding to the transition from the combined field emission and Townsend regime to the traditional Paschen's law, and deviate once αd_{eff} becomes sufficiently large for streamer formation. Alternatively, noting that the transition to Paschen's law occurs when $\alpha d_{eff} \approx 10$, we can calculate γ_{SE} to match the experimental results by solving (2.3) to obtain

$\gamma_{SE} = \{\exp[\bar{p}\bar{d}_{eff} \exp(-\bar{p}\bar{d}_{eff}/\bar{V})] - 1\}^{-1}$. Future work will aim to better characterize γ_{SE} and further assess streamer formation and behavior.

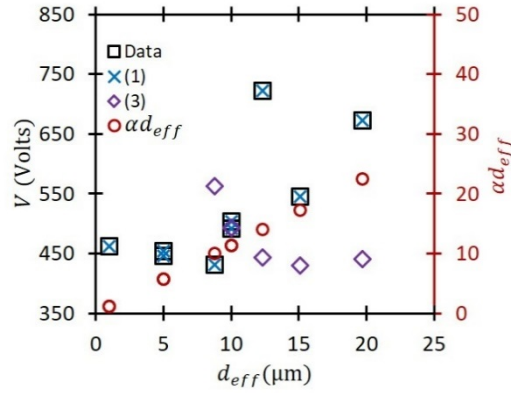


Figure 2.11: Breakdown voltage, V , as a function of effective gap distance, $d_{eff} = d + \delta$, where d is the gap distance and δ is the crater depth, from the experimental data, the numerical results of (2.1), and the analytic results of (2.3) assuming $\gamma_{SE} = 1.5 \times 10^{-3}$. The product of the ionization coefficient and effective gap distance, αd_{eff} , is shown on the secondary vertical axis. The transition to Paschen's law (PL) occurs for $\alpha d_{eff} \approx 10$. PL predicts breakdown until it becomes driven by streamer formation when $\alpha d_{eff} > 18$.

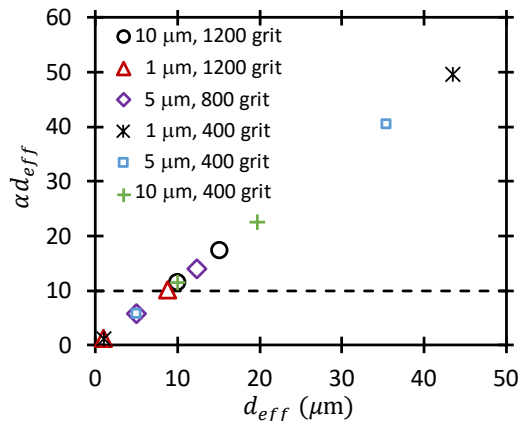


Figure 2.12: The product of the ionization coefficient and effective gap distance, αd_{eff} , as a function of the effective gap distance gap distance, $d_{eff} = d + \delta$, where d is the gap distance and δ is the crater depth. Each pair of symbols shows the αd_{eff} value after the first and tenth breakdown events, showing that crater formation can push breakdown behavior past the $\alpha d_{eff} \approx 10$ criterion for transition to Paschen's law.

Finally, we theoretically assess the impact of crater formation on breakdown voltage. Figure 2.12 summarizes the six sets of data, showing αd_{eff} after the one and ten breakdown events. Notably, the data from the samples with initial gap distances of 1 and 5 μm had $\alpha d_{eff} < 10$ after the first breakdown event, but transitioned to $\alpha d_{eff} > 10$ after the tenth breakdown event, indicating that crater formation alone can push the breakdown mechanism into the Townsend regime even if the anode-cathode gap remains unchanged. This could have significant implications on device design, where many breakdown events are expected to occur and breakdown voltage is expected to remain constant. Moreover, this suggests that eventually, subsequent breakdown events will not increase crater depth much since one transitions to the Townsend regime, where field enhancement diminishes, reducing the localization of breakdown that occurs at smaller gaps in the field emission regime. This suggests that most sensitivity to the influence of surface effects in breakdown occurs when operating in the field emission regime with rough cathodes, where the higher electric fields lead to greater crater formation and noticeable changes in breakdown voltage and electrode conditions.

2.5 Conclusion

These results show the dependence of breakdown voltage on repeated breakdown events for a pin-to-plate configuration at microscale gaps and atmospheric pressure. Specifically, they are the first results examining the impact of surface roughness on microscale gas breakdown. Additionally, we are the first to show that breakdown voltage for subsequent breakdown events agrees with theory by accounting for the effective gap distance as the sum of the interelectrode gap separation and resulting crater formation.

With a polished copper plate as the cathode and a tungsten dissection needle as the anode, we measured the breakdown voltage for 1, 5, and $10 \pm 0.5 \mu\text{m}$ gaps. We polished the cathodes using 400, 800, and 1200 grit papers with a wet polishing machine to vary the surface roughness. Figure 2.5 to Figure 2.7 show that the change in breakdown voltage due to surface roughness for a fixed gap distance or due to gap distance for a fixed surface roughness were not statistically significant. The major change in behavior involved the variation in breakdown voltage due to cathode crater formation. AFM and optical imaging before and after the breakdown events showed that the cathodes changed from having average surface feature heights ranging from 0.24 to 1.47

μm before the events to containing small ablated regions with crater depths ranging from 3 to 50 μm (cf. Table 2.2). The combination of initial surface feature height and the ablation/melting of surface material changed the effective gap distance of the system. Cathode crater formation drove the changes by increasing the effective gap distance, which increased breakdown voltage for multiple breakdown events. We observed similar breakdown voltages for similar effective gap distances independent of the interelectrode spacing. Applying a matched asymptotic analysis to the experimental results demonstrated that the breakdown voltage was a function of the effective gap distance and that the transition from field emission to Townsend avalanche occurred at effective gap distances equivalent to the gap distances observed for single breakdown studies^{26,39}. Moreover, β varied linearly with gap distance in the field emission regime before becoming constant at the transition to the Townsend avalanche, as observed for single breakdown studies³⁹.

While the current study focused on the breakdown voltage and surface structure, predominantly cathode feature height or depth, sensitivity analysis of breakdown theory indicates that microscale gas breakdown voltage also depends strongly on work function⁴⁴. Future studies will extend the analysis to assess changes in work function with repeated breakdown events to ascertain the relative contribution on gas breakdown, particularly when uncertainty in work function and field enhancement dominate the sensitivity of breakdown voltage predictions for gap distances below 10 μm ⁴⁴. Although mean surface roughness did not impact the breakdown voltage, it did lead to concentration of the discharge at emission sites that impacted subsequent breakdown events; however, this study did not consider the impact of a single, controllable sharp-tipped emitter on breakdown voltage. Future studies will thus further investigate the impact of controllable aspect ratio⁶⁷ as a function of gap distance and pressure on gas breakdown and current density to additionally characterize transitions between electron emission mechanisms^{22,64} and breakdown phenomena.

3. THE IMPACT OF CATHODE – ANODE GAP ON ELECTRON EMISSION AT ATMOSPHERIC PRESSURE

3.1 Background and Motivation

Electronic device manufacturing continues to demand reduced device sizes, necessitating characterization of gas breakdown for these devices^{2,73}. The application of these devices in the medical, aerospace, and consumer electronics further accelerates size reductions^{9,15,22,23,74}. Recent work has laid the ground work for better understanding of gas breakdown by examining the effects of removing material dependence in breakdown theory by creating scaling laws³¹. Modern work predicting breakdown relies on empirical constants that have been measured at limited conditions. The scaling laws developed helped to create a universal theory of breakdown that removed material dependence for microscale field emission (FE) discharges and discharges created by Townsend avalanche that follow the classical Paschen's Law (PL)²⁶. Further exploring the FE effects at microscale work showed that Townsend avalanche was insufficiently strong to induce a sustained avalanche for sufficiently small gaps, meaning that FE driven breakdown drove breakdown⁷².

The importance of FE in microscale gas breakdown naturally leads to the question concerning other electron emission mechanisms. Theory, simulation, and experiment indicate that electron emission transitions from FE, as defined by the Fowler-Nordheim law, to space-charge limited emission, as defined by the Child-Langmuir law, as one reduced diode size at vacuum. At even smaller gap sizes, one transitions from the classical Child-Langmuir law to the quantum space-charge limited law.

This dissertation's focus on atmospheric pressure raises the question about how electron emission transitions with reducing gap size when pressure is included. Another graduate student in the group is currently unifying space charge limited breakdown, Child-Langmuir (CL) and Mott-Gurney (MG), which is space-charge limited emission with collisions, FN, and PL⁷⁵. This model is universal (true for any gas) except for a single material-dependent constant in PL. An intermediate step performed by another graduate student in our research group unified CL, MG, and FE⁵⁴; this student has expanded this concept to unify CL, MG, FE, Ohm's law (for an external resistor), and thermionic emission⁷⁶. Unification of these theories moves closer to providing experimentalists a guideline for selecting device parameters to satisfy desired emission conditions or avoid/create breakdown *a priori*. Although these approaches are generally for perfectly smooth

electrodes, surface roughness can cause field enhancement, which may modify the predictions above.⁷⁷

Experimental work exploring electron emission for nanoscale diodes characterized the transition from field emission to quantum space-charge limited emission and classical space-charge limited emission at vacuum^{51,78}. For the smallest gaps, comparable to the de Broglie wavelength of the electrons, $I \propto V^{1/2}$, indicating quantum space charge limited emission current scaling⁷⁹⁻⁸¹. Further work explored the effects of microscale repetitive discharges on a pin to plate configuration quantifying the transition from field emission of electrons to the self-sustained plasma breakdown of the gap⁶⁸. Microscale gaps on the micro-scale field emission current had negligible impact on the pre-breakdown regime of the discharge. To further explore the effects on the microscale work was done expanding the pin to plate geometry to look at how repetitive breakdown events altered the breakdown condition⁸². Repetitive breakdown events significantly altered the surface structure of the electrodes, leading to altered gap distance significantly larger than the initial conditions. The altered surface structure affects sharp or blunt nanoscale features, potentially modifying the field enhancement on the surface, leading to an altered effective work function. The effects of these sharp and blunt features were the focus of theoretical formulations studying emission physics in nanoscale diodes⁶⁷. The width, height, and degree of sharpness of individual nanostructures significantly impacts the emission physics of a nanoscale gap DC device.

This chapter expands upon the theoretical work to measure the emission current from the nanoscale devices. The devices are based on the geometry from Lin, et al. in 2017⁶⁷. The nanoscale devices were fabricated at Birck Nanotechnology Center at Purdue University, and testing was conducted to measure electron emission current as applied voltage was increased. The measured current allows for determination of emission regime along with estimates for emission area and electron mobility. The measured currents were also evaluated in terms of previous theoretical work showing transitions between the regimes

3.2 Materials and Methods

Lin, et al. theoretically examined the implications of electrode geometry on emission current for nanoscale diodes⁶⁷. We used this geometry as a baseline for designing devices for assessing gas breakdown and electron emission for various gap distances and electrode aspect

ratios. The tests were conducted in air at atmospheric pressure to simulate typical usage in modern electronics.

Figure 3.1 shows the geometry used to fabricate the test devices. Each device consists of two $100\ \mu\text{m}$ square test pads separated by a gap d . One of the test pads is smooth; the second has a surface protrusion of length h , width $2a$, and angle α . We fixed $\alpha = 45^\circ$ and constructed devices with various h and a . Adjusting h for a fixed a varied both the effective interelectrode gap distance $d_{\text{eff}} = d - h$ and changed protrusion's aspect ratio; adjusting a just changed the aspect ratio. The test pads were fabricated directly onto the design of the devices by making $100\ \mu\text{m} \times 100\ \mu\text{m}$ squares on each side. The pads were used to place test probe electrodes onto the devices to apply voltage and measure current.

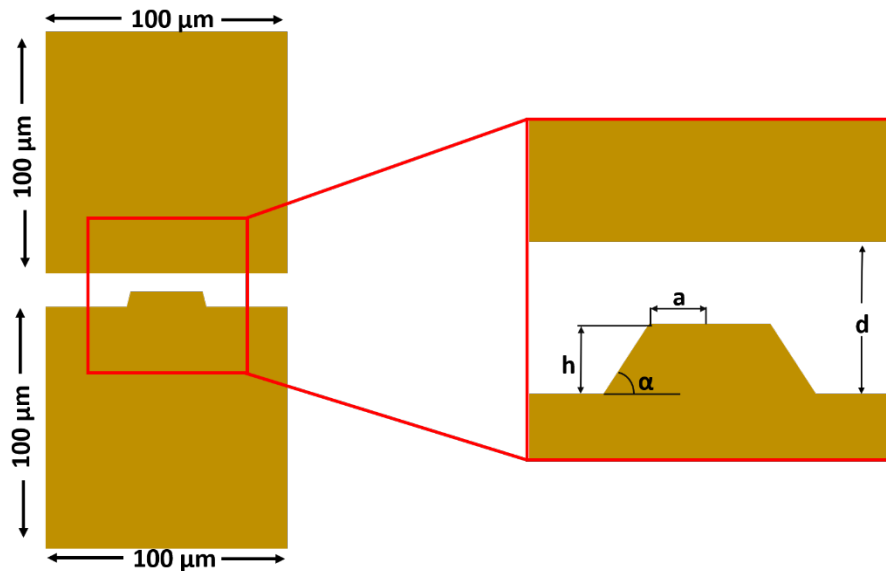


Figure 3.1: Geometry of the designed nanoscale device showing the sharp or blunt surface protrusion to evaluate field enhancement through current emission measurement and scaling by altering a , h , and d and fixing α .

Birck Nanotechnology Center fabricated these devices using electron beam lithography (EBL) on a base silicon wafer with a top layer of silicon dioxide to ensure electrical insulation of the devices. Multiple devices were fabricated on a single wafer per run to provide multiple devices for testing. Devices were then created on top of the electrically insulative layer using $5\ \text{nm}$ of titanium and $100\ \text{nm}$ of gold. Figure 3.2 shows the layers as they were produced along with cross-section and top views of the devices.

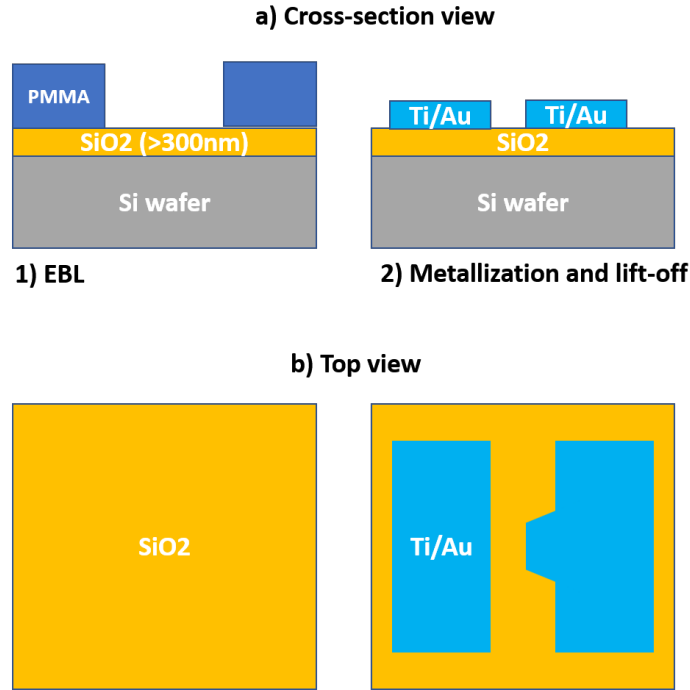


Figure 3.2: (a) The cross-section of the fabrication process showing the poly-methyl methacrylate (PMMA) photo-resist layer with an electrical insulation layer of SiO₂, and an electrode layer of 5 nm of titanium under a 100 nm layer of gold. (b) shows the general shape of the devices considered before the 100 μm pads are added to the design to facilitate testing.

Following the process described above and the general layering shown in Figure 3.2, we fabricated 200 devices per chip consisting of five replicates of forty different variations of the protrusion with different d , h , a , and $d_{\text{eff}} = d - h$. Table 3.1 lists the parameter space of the designs in its entirety.

Table 3.1: Parameter space used to fabricate devices.

Data #	a [nm]	h [nm]	d [nm]	$d_{eff} = d - h$ [nm]
1	384	769	1000	230
2	76	769	1000	230
3	38	769	1000	230
4	192	769	1000	230
5	769	769	1000	230
6	50	500	1000	500
7	125	500	1000	500
8	250	500	1000	500
9	500	500	1000	500
10	62	250	1000	750
11	125	250	1000	750
12	250	250	1000	750
13	100	50	1000	950
14	100	100	1000	900
15	38	384	500	115
16	96	354	500	145
17	192	384	500	115
18	384	384	500	115
19	62	250	500	250
20	125	250	500	250

Table 3.1 Continued: Parameter space used to fabricate devices.

Data #	a [nm]	h [nm]	d [nm]	$d_{eff} = d - h$ [nm]
21	250	250	500	250
22	31	125	500	375
23	62	125	500	375
24	125	125	500	375
25	25	50	500	450
26	50	50	500	450
27	48	192	250	57
28	31	125	250	125
29	96	192	250	57
30	62	125	250	125
31	31	62	250	187
32	25	25	250	225
33	192	192	250	57
34	125	124	250	126
35	62	62	250	187
36	48	96	125	28
37	62	62	125	62
38	96	96	125	28
39	31	62	125	62
40	31	31	125	93

The edge of each device was $400\ \mu\text{m}$ away from its nearest neighbor to minimize electromagnetic interference during testing. Due to the solid-state design and voltages applied heating issues were not able to be mitigated for these tests. Figure 3.3 shows the layout of each chip, with a blown-up view showing labeling of each device on the chip. The blown-up view in Figure 3.3(b) shows the orientation of the devices on the chip with the protrusion always on the bottom pad, protruding into the middle of the device. The gap is too small to be seen in these images.

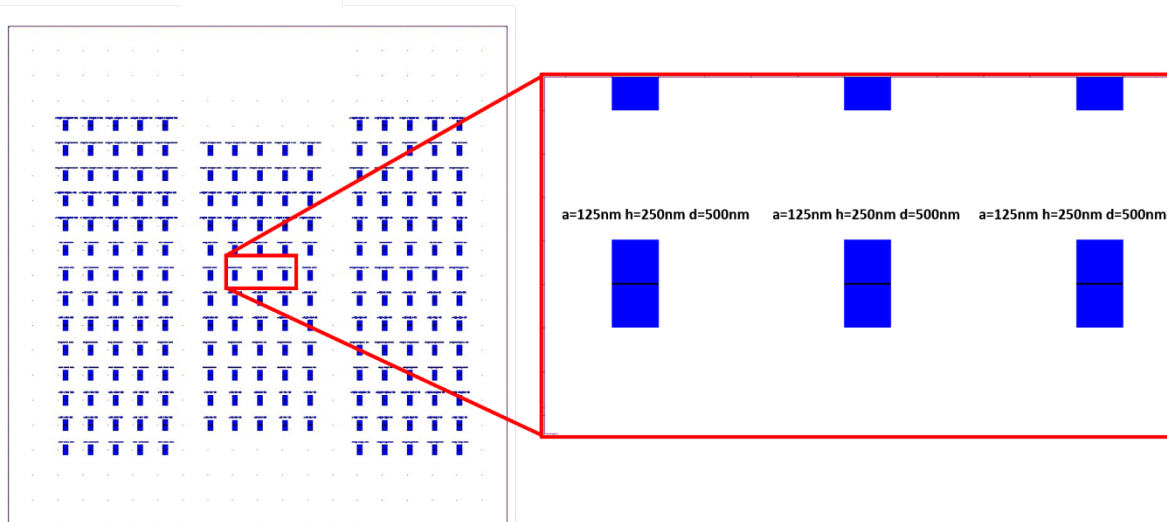


Figure 3.3: Layout of devices on $1\text{ cm} \times 1\text{ cm}$ square chips cut from silicon wafer with a view of the device layout showing spacing for testing.

We measured the emitted current as a function of applied voltage using a Keithley 2410-C source meter unit (SMU) with sensing current sensitivity of 1 nA and sourcing voltage with a resolution of $1\text{ }\mu\text{V}$. The measured current was based on a two wire reverse bias diode test with current measured at a user specified rate during a voltage sweep⁸³. We used the microscope and micromanipulators present on the Signatone H-150W DC probe station to place tungsten PTT 12/4-25 needle probes with tips with a diameter of $1.2\text{ }\mu\text{m}$ on each of the gold test pads fabricated on the devices. The positive probe was always placed on the pad with the protrusion feature for each test. The test consisted of a voltage sweep starting at 0 V with steps of 0.005 V lasting 0.1 s until the current spiked, indicating device failure and melting, with current sampled at 10 samples per second. Device failure was confirmed by using a microscope to confirm test pad degradation. Figure 3.4 shows the general electrical test setup as it was connected to each device.

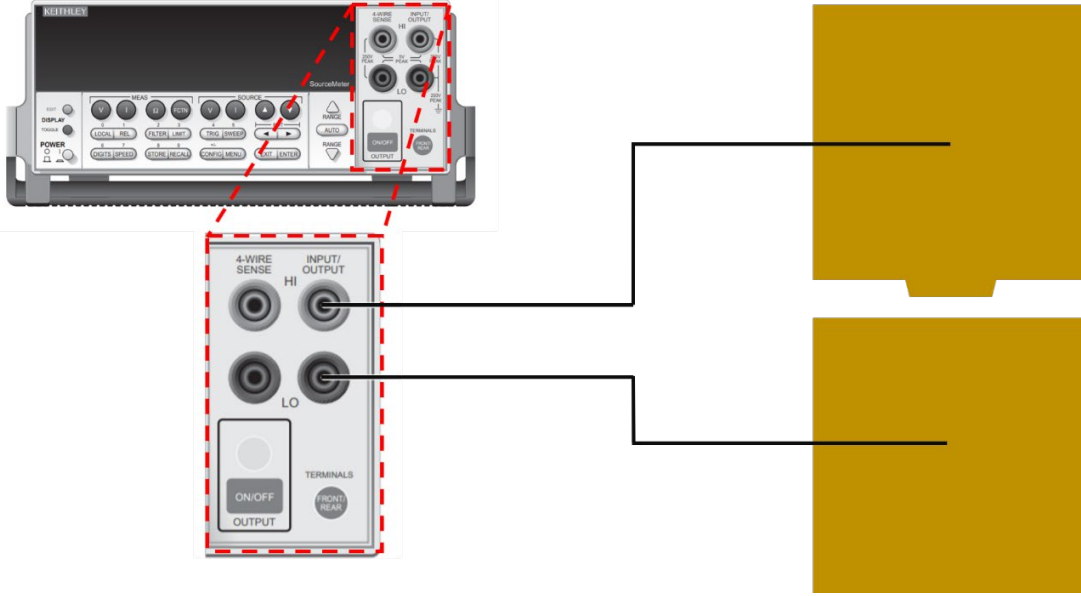


Figure 3.4: Electrical testing setup of the Keithley 2410C source meter unit (SMU) to apply voltage and measure current across the test devices⁸⁴.

3.3 Results

Using previously published methods, the data was analyzed to determine which emission regime the devices were during the test^{51,68,78}. Current (amperes) and voltage (volts) data was collected during the test and plotted with different fits and axes scaling to observe regions that are linear. The current density J for the different emission regimes of interest, the classical Child-Langmuir law (CL), Fowler-Nordheim (FN) law, and Mott-Gurney (MG) law, may be written as

$$J_{CL} = \frac{4\epsilon_0}{9} \left(\frac{2e}{m}\right)^{1/2} \frac{V^{3/2}}{d^2}, \quad (3.1)$$

$$J_{FN} = A_{FN}(\beta V)^2 \exp\left[\frac{-B_{FN}\phi_w^{3/2}}{\beta V}\right], \quad (3.2)$$

and

$$J_{MG} = \frac{9}{8} \epsilon \mu \frac{V^2}{d^3}, \quad (3.3)$$

respectively, where e is electron charge, ϵ_0 is the permittivity of free space, m is electron mass, V is applied voltage, $d_{eff} = d - h$ is the effective gap distance from the protrusion to the flat electrode, A_{FN} and B_{FN} are Fowler-Nordheim constants, ϕ_w is the electrode work function, ϵ is the permittivity of the medium, and μ is the electron mobility^{43,50,85}. Thus, plotting experimentally measured I (since $J = I/A$, where A is the emission area, is not known *a priori*) as a function of V

can provide insight into the appropriate mechanism based on the functional relationships. In other words, $I \propto V^{3/2}$ denotes CL, $I \propto V^2$ denotes MG, and $\ln(I/V^2) \propto V^{-1}$ gives FN (known as a “FN curve”). Theoretical assessments indicate that these simple scaling relationships strictly hold only in the asymptotic limits of high μ and/or high V for CL, low μ for MG, and low V for FN^{54,77}; intermediate levels require an exact solution of the full force law for an electron emitted from the cathode, leading to measured I that falls between the various asymptotic limits^{54,77}.

We first plotted the data on a FN curve since we anticipate FN scaling at low V . Figure 3.5 shows the FN curves for (a) $a = 192 \text{ nm} \pm 10 \text{ nm}$ with three values of d_{eff} and (b) $d_{eff} = 115 \text{ nm} \pm 10 \text{ nm}$ and three different a values.

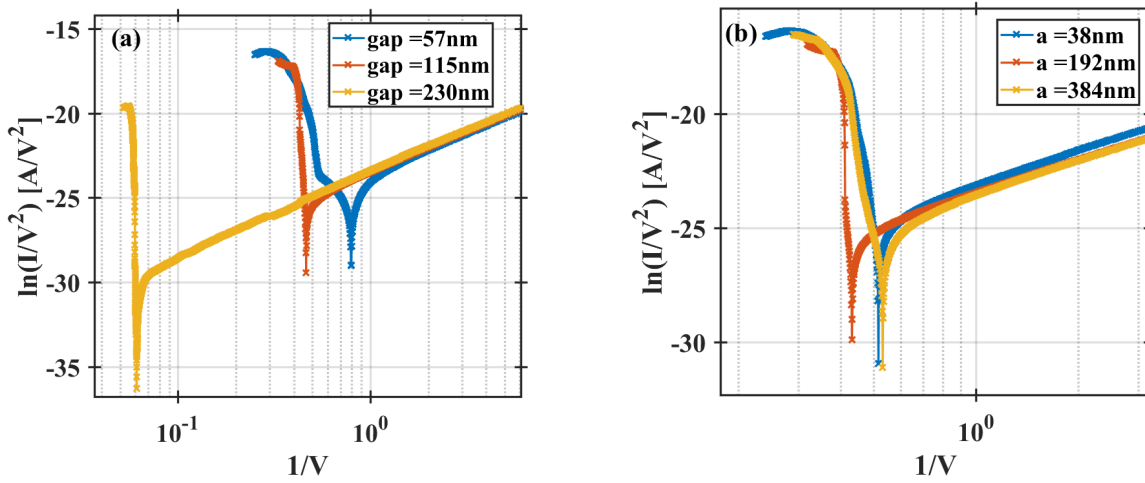


Figure 3.5: FN scaling of the data for (a) with $a = 192 \text{ nm} \pm 10 \text{ nm}$ and $d_{eff} = 57 \text{ nm} \pm 10 \text{ nm}$, $115 \text{ nm} \pm 10 \text{ nm}$, and $230 \text{ nm} \pm 10 \text{ nm}$ and (b) with $d_{eff} = 115 \text{ nm} \pm 10 \text{ nm}$ and $a = 38 \text{ nm} \pm 10 \text{ nm}$, $192.3077 \text{ nm} \pm 10 \text{ nm}$, and $384 \text{ nm} \pm 10 \text{ nm}$ showing strong gap dependence on breakdown voltage but no dependence on width $2a$.

Figure 3.5 shows that the effective gap size of $d_{eff} = d - h$ has a dominant effect on the emission current and breakdown of the device. Breakdown was determined by a sudden spike in current, leading directly to a constant current value that indicated a short circuit, or device failure. A dramatic change in slope from the FN regime occurred during breakdown. Device shorting was confirmed with the microscope as visible damage to the devices from heating was observed. Figure 3.5(a) shows that the breakdown voltage increases with increasing d_{eff} while Figure 3.5(b) shows that it is insensitive to changes in a . Table 3.2 shows the estimated breakdown voltage (V_{BD}) for each of the cases presented in Figure 3.5.

Table 3.2: Estimated breakdown voltage from FN plots for each case presented.

$d_{eff} = d - h$ [nm]	a [nm]	V_{BD} [nV]
57	192	1.9
115	192	2.3
230	192	16.7
115	38	2.1
115	192	2.0
115	384	2.4

Table 3.2 shows that V_{BD} generally increased with increasing d_{eff} and that a did not have any particular effect. The linear region on the FN curve indicate the regime where FN emission dominates. We performed a linear regression over this region to fit the Fowler-Nordheim constants A_{FN} and B_{FN} for each case. The emission area and mobility were estimated using a least squares fit to obtain the current density J . This process permits comparison of the experimental data to the theory describing the transition between the regimes⁵⁴. Since emission area and mobility are unknown, we can only set limits, varying both until experiment and theory have notably deviated setting an upper limit for the data. Due to the design of the parameter space, not all gap distances were fabricated for each feature width a , resulting in different d_{eff} being used for the data presented in some cases. For the smallest mobility considered, Figure 3.6 shows $d_{eff} = 28 \text{ nm} \pm 10 \text{ nm}$ and a fitted emission area of 64 nm^2 . Regardless of the mobility used, emission current is clearly FN dominated until breakdown conditions are reached.

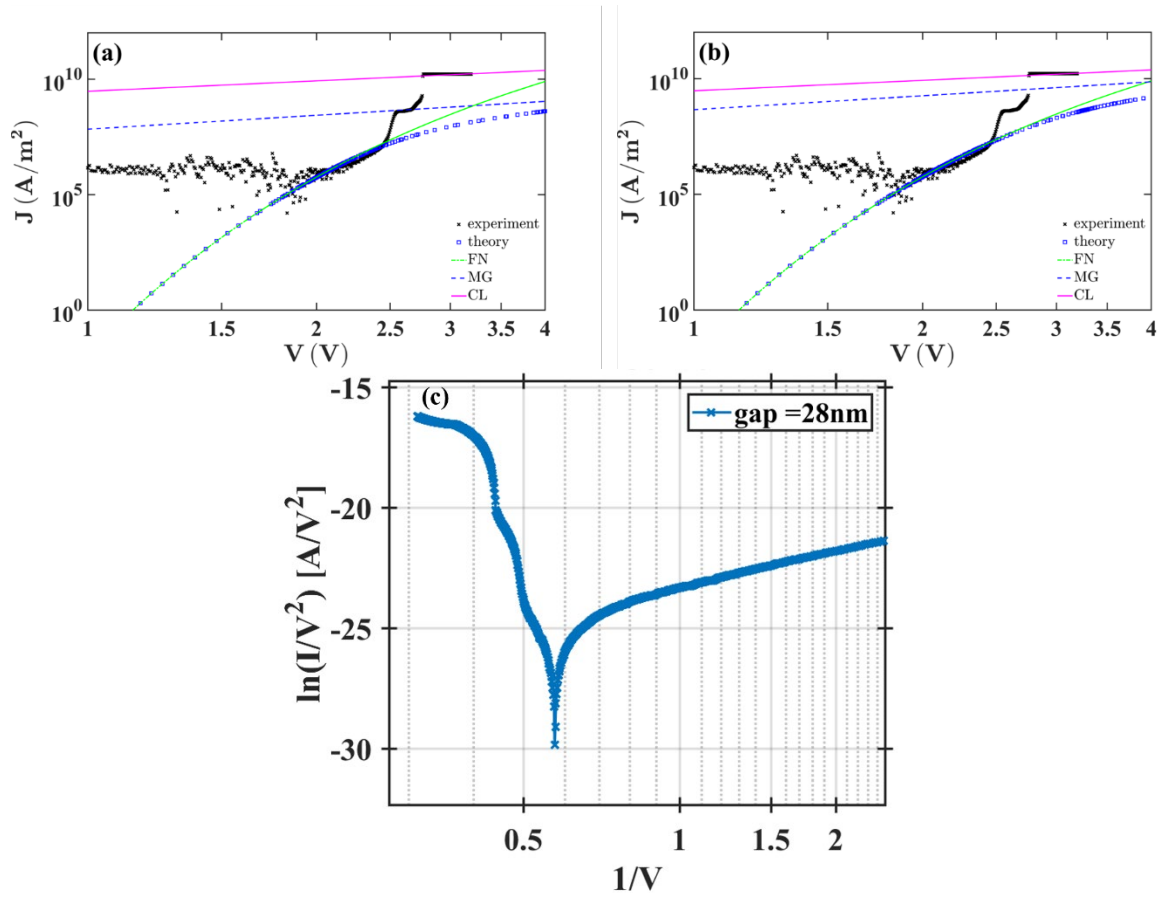


Figure 3.6: Experimental data for $d_{eff} = 28 \text{ nm} \pm 10 \text{ nm}$ and a fitted emission area of 64 nm^2 fit to full theory from Darr, et. al. using mobility of (a) $0.00015 \text{ m}^2\text{V}^{-1}\text{s}^{-1}$ and (b) $0.001 \text{ m}^2\text{V}^{-1}\text{s}^{-1}$ showing FN dominated emission transitioning to breakdown as the device fails and (c) the associated FN plot for Ref. [54].

For $d_{eff} = 28 \text{ nm} \pm 10 \text{ nm}$ and a fitted emission area of 64 nm^2 fit to full theory from Darr et. al. using mobility of (a) $0.00015 \text{ m}^2\text{V}^{-1}\text{s}^{-1}$ and (b) $0.001 \text{ m}^2\text{V}^{-1}\text{s}^{-1}$ showing fieldemission transitioning to breakdown as the device fails and (c) the associated FN plot for Ref [54]. The plateau regions that appear to scale with MG or CL emission are attributed to the physical deterioration of the device during the test because they occur after a large spike in current and cannot be explained by either theory. Viewing the devices under the microscope showed that the devices heated to the point of melting during the test, which contributed to the direct transition to breakdown and accounts for the constant current value at the higher applied voltages.

As gap size is increased the transition behavior predicted by Darr, et al. is observed in the data⁵⁴. Figure 3.7 shows the transition behavior for a $d_{eff} = 125 \text{ nm} \pm 10 \text{ nm}$ and a fitted emission

area of 64 nm^2 with mobilities of (a) $0.0003 \text{ m}^2\text{V}^{-1}\text{s}^{-1}$ and (b) $0.001 \text{ m}^2\text{V}^{-1}\text{s}^{-1}$. It is assumed that the lower mobility causes the data to approach the MG asymptote; however, the exact theoretical model poorly predicts the experimental data for this mobility. Using higher mobility (cf. Figure 3.7 (b)) gives better agreement between the exact solution⁵⁴ and the experimental data, suggesting that it is more representative of the data. In this case, the measured current follows FN at lower current and space charge just begins to contribute prior to breakdown. The testing of the devices was halted as the breakdown was observed. Note that the emission is transitioning to space-charge dominated because the experimental results and the exact solution still do not approach the MG asymptote.

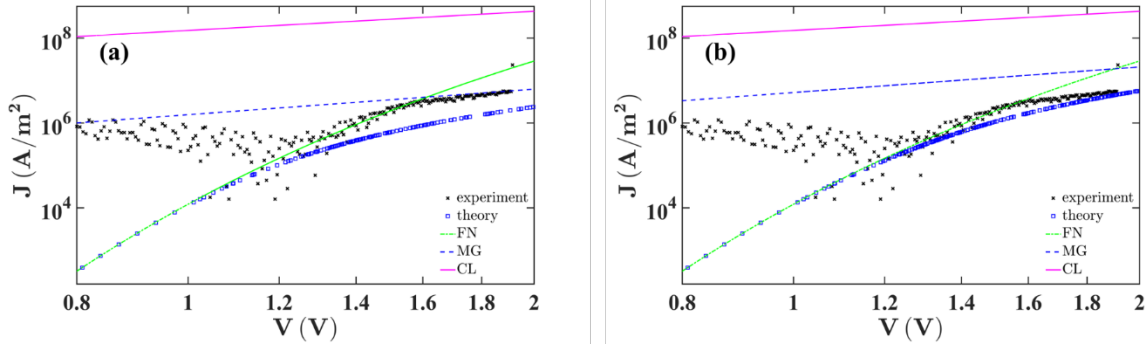


Figure 3.7: Transition behavior for $d_{eff} = 125 \text{ nm} \pm 10 \text{ nm}$ using mobilities of (a) $0.0003 \text{ m}^2\text{V}^{-1}\text{s}^{-1}$ and (b) $0.001 \text{ m}^2\text{V}^{-1}\text{s}^{-1}$. Using the lower mobility predicts transition to MG; however, the full theory does not match the experimental data. The higher mobility agrees better with the experimental results and indicates that the data primarily follows FN over this regime.

Figure 3.8 repeats this process for $d_{eff} = 450 \text{ nm} \pm 10 \text{ nm}$ and a fitted emission area of 64 nm^2 with mobilities of (a) $0.003 \text{ m}^2\text{V}^{-1}\text{s}^{-1}$ and (b) $0.01 \text{ m}^2\text{V}^{-1}\text{s}^{-1}$. In this case, the exact solution, the FN asymptote, and the experimental data all match prior to breakdown occurring, as indicated by the spike in current. Thus, as with conventional microscale gas breakdown and $d_{eff} = 28 \text{ nm}$, breakdown directly occurs from field emission.

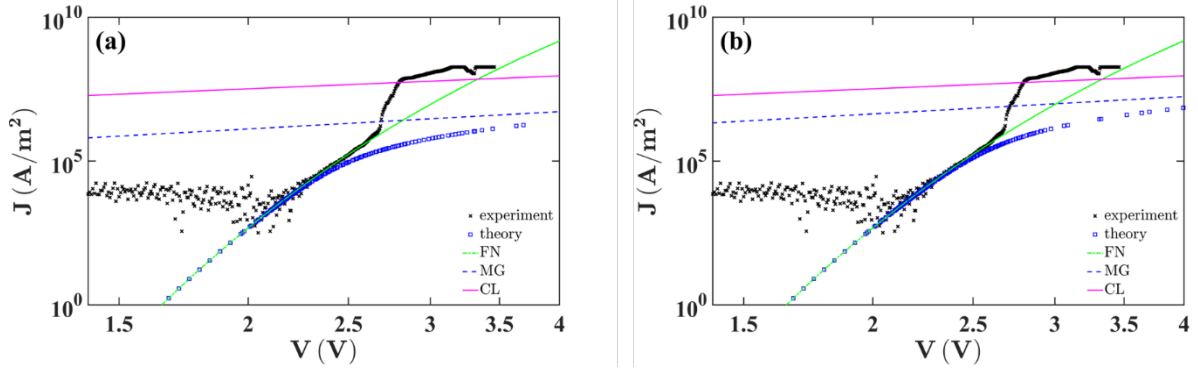


Figure 3.8: JV plot for a device with d_{eff} of $450 \text{ nm} \pm 10 \text{ nm}$ and a fitted emission area of 64 nm^2 with mobilities of (a) $0.003 \text{ m}^2\text{V}^{-1}\text{s}^{-1}$ and (b) $0.01 \text{ m}^2\text{V}^{-1}\text{s}^{-1}$ showing no transition behavior, moving directly from FN dominant emission to breakdown.

Figure 3.6 - Figure 3.8 show that emission transitions from FN toward MG without transitioning directly to breakdown only for $d_{eff} \approx 125 \text{ nm}$. Breakdown is observed due to the almost vertical spike in current density at high V rather than following the full solution emission curve. To understand why, we equate the asymptotic solutions from (3.2) and (3.3) to obtain

$$V_{FN-MG} = B_{FN}D / \ln\left(\frac{8A_{FN}d_{eff}}{9\mu\epsilon_0}\right) \quad (3.4)$$

which has a minimum at

$$d_{eff} = 9\mu\epsilon_0 \exp(1) / 8A_{FN}. \quad (3.5)$$

To examine the relevance of this behavior on the transition from field emission to space-charge limited emission, and its effect on the data presented (3.4) was plotted for $d_{eff} = 28 \text{ nm}$ case with $\mu = 0.00299 \text{ m}^2\text{V}^{-1}\text{s}^{-1}$, $A = 6.4 \times 10^{17} \text{ m}^2$, $A_{FN} = 0.0013 \text{ A} \cdot \text{eV} \cdot \text{V}^{-2}$, and $B_{FN} = 1.1645 \times 10^9 \text{ Vcm}^{-1}\text{eV}^{-3/2}$ found from fitting (3.2) to the experimental data.

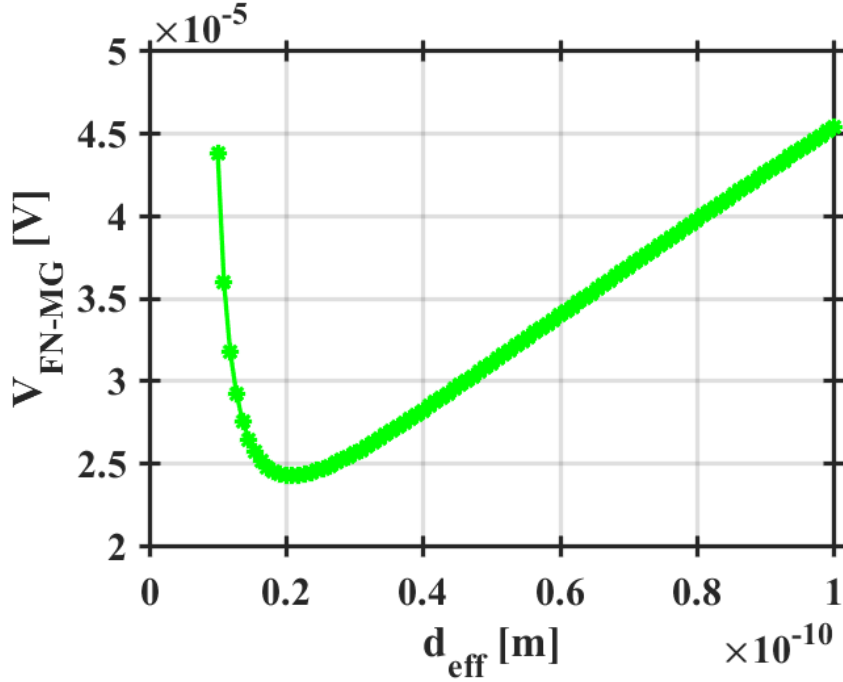


Figure 3.9: Transition voltage presented from (3.4) for $\mu = 0.00299 \text{ m}^2\text{V}^{-1}\text{s}^{-1}$, $A = 6.4 \times 10^{17} \text{ m}^2$, $A_{FN} = 0.0013 \text{ AeV} \cdot \text{V}^{-2}$, and $B_{FN} = 1.1645 \times 10^9 \text{ Vcm}^{-1}\text{eV}^{-3/2}$ demonstrating that the minimum voltage for the transition from FN to MG to occur is for $d_{\text{eff}} \approx 0.02 \text{ nm}$.

Figure 3.9 should be considered as a representative curve useful for analyzing devices with known FN and mobility parameters. This implies that there is a specific gap distance for which the transition will occur. The device was operating at a voltage clearly on the far-right side of the curve shown, meaning it was not near a transition condition of gap and applied voltage. This may explain the presence of the transition behavior shown in the $125 \text{ nm} \pm 10 \text{ nm}$ data but not in either the $28 \text{ nm} \pm 10 \text{ nm}$ or the $450 \text{ nm} \pm 10 \text{ nm}$. Since the calculated mobility and FN constants are fit from the data, this should be considered as an estimate as we cannot directly measure them for the devices tested. Table 3.3 shows the upper limit estimates of the mobility μ , area A , and relative error σ comparing the current to the FN solution assuming the largest possible emission area for the three d_{eff} considered.

Table 3.3: Summary of upper limit estimates for mobility μ , area A , and the resulting relative error σ between the current and the FN current for the three different gap distances considered.

d_{eff} [nm]	A [nm ²]	μ [m ² V ⁻¹ s ⁻¹]	σ
28	95.101504	0.00299	0.0994
125	59.954049	0.0162	0.1054
450	905542.56	0.0483	0.081

Table 3.3 shows that the emission area increases dramatically with gap distance. The limits for μ and A are based on σ obtained from the least squares fit of the data to the full theoretical solution assuming an arbitrarily large emission area. This serves as a scale for the minimum error possible for the data in the sets fit. The calculated A and μ assumed 30% as the maximum error when presenting the data in the previous figures. The largest estimated area is about 0.9 μm^2 , which is still about 10 times smaller than the actual total area of the device. The total possible emission area would occur if the entire gap emitted electrons from the test pad edges that are 100 μm long and 105 nm tall. Despite this increased emission area, the larger gaps did not attain space charge limited or even transitional behavior.

3.4 Conclusion

Nanoscale devices designed to isolate effects of gap distance and field enhancement were fabricated and test to study emission current and observe Fowler-Nordheim, Mott-Gurney, and Child-Langmuir behavior. The geometry of the devices was constructed such that a parallel plate device was fabricated with a protrusion into the gap that served to alter local field enhancement, though varying degrees of tip sharpness. The devices were made of gold and Titanium layered onto silicon wafers electrically isolated with SiO₂. Electrical tests similar to reverse bias diode testing was conducted, applying voltage to the side of the device with the protrusion and measuring the leakage current across the nanoscale gap of the device. A Signatone H-150W DC probe station was utilized to place tungsten PTT 12/4-25 needle probes with tips of 1.2 μm . The probes were placed using the stations microscope and micromanipulators on each of the gold test pads that were fabricated on the devices. The positive probe was always placed on the pad with the protrusion feature for each test. The test consisted of a voltage sweep starting at 0 V with steps of 0.005 V lasting 0.1 s until a spike in current was observed indicating the device had failed and was now

melted. Current was sampled at a rate of 10 samples per second. Device failure was confirmed under the microscope by observing the test pad degradation due to melting. Current (amperes) and voltage (volts) data was collected during the test and plotted with different fits and axis scaling to observe regions that are linear. The only observable linear trends were with certain portions of the FN curve. Figure 3.5 shows that $d_{eff} = d - h$ has a dominant effect on the emission current and breakdown of the device. The breakdown voltage increased with increasing gap size, as expected, while the protrusion width does not appear to have any effect on the emission current. This process was repeated for CL and MG scaling with similar results showing no effect of protrusion width. Emission area and mobility were estimated by using linear regression fits to the data and utilizing the theory from Darr, *et al.* to find a full solution to match the data. For $d_{eff} = 125 \text{ nm} \pm 10 \text{ nm}$ and a fitted emission area of 64 nm^2 with mobilities of (a) $0.0003 \text{ m}^2\text{V}^{-1}\text{s}^{-1}$ and (b) $0.001 \text{ m}^2\text{V}^{-1}\text{s}^{-1}$; the transition region between field emission and space charge emission was evident, as noted previously in published work by Darr, *et al.* However, this transition was not observed for $d_{eff} = 28 \text{ nm} \pm 10 \text{ nm}$ and $450 \text{ nm} \pm 10 \text{ nm}$ due to a local minimum being predicted by (3.5) and (3.6) implying that the mid-sized gaps more easily enter a space charge influenced transitional regime due to the effects of gap distance d_{eff} .

This chapter showed for the first time that while microscale gaps undergo field emission driven breakdown, nanoscale gaps may undergo breakdown either from field emission or directly from space-charge limited emission. Interestingly, the results were not monotonic with increasing gap distance since the smallest (28 nm) and largest (450 nm) gaps underwent breakdown from field emission, while the intermediate gap exhibited space charge effects (125 nm) prior to undergoing breakdown. Previous theory estimated that the asymptotic solutions for MG, FN, and CL intersected for a gap distance of 250 nm at atmospheric pressure. In reality (both experimentally and theoretically), such a condition will not exist since the conditions requiring this intersection do not, strictly speaking, satisfy each asymptotic solution; however, it serves as a signpost for a design parameters space where emission becomes sensitive to small perturbations in device conditions and parameters such as pressure, field enhancement, and general electrode conditions. These experiments demonstrate the design and construction of nanoscale devices to study electron emission and gas breakdown. Future studies can better characterize mobility to better describe the transition in emission regimes observed both experimentally and theoretically.

Future work will also consider the implications of pressure and temperature on these transitions, as well as the relevance of thermionic emission when heating is considered⁷⁶.

4. COMPUTATIONAL ASSESSMENT OF IONIZATION COEFFICIENT

4.1 Background and Motivation

As modern electronics advance, becoming smaller and smaller, the importance of understanding the physical mechanisms of gas breakdown become vitally important to device function and lifetime^{2,33}. The function of the devices largely determines if breakdown is advantageous or adverse. Many medical devices designed to apply reactive species directly to tissue rely on the direct breakdown of some form of gas to generate the requisite species³⁻⁹. Next generation piezoelectric transformers, used for sources of backlight fluorescence in monitors, x-ray generation devices, low voltage battery chargers, and even AC/DC converters all rely on breakdown as well¹⁴. Nanosecond pulsed repetitive discharges are of great interest to the aerospace community to alter flow regimes and combustion processes⁸⁶⁻⁸⁹. Adverse applications are wide ranging as well. Medical applications looking at the use of applied electric fields are used to treat many forms of cancer¹⁶⁻¹⁸. Nano- and microscale electronics also need to avoid breakdown in order for them to function properly over their specified lifespan^{22,23}. Thus, the importance of understanding the physical mechanisms driving breakdown have been studied for some time. Typically gas breakdown behavior is described by the Townsend avalanche and Paschen's law²⁷. However, at micro and nanoscale gaps, field emission become important, leading to what is called the modified Paschen curve⁹⁰. Previous studies have experimentally and theoretically characterized the breakdown behavior at these smaller gaps by examining the individual mechanisms that affect pre-breakdown and the breakdown processes³³. Further theoretical work eliminated material dependence to derive universal scaling laws^{69,91}.

Any theory for Townsend's avalanche requires calculating the ionization coefficient α . All the commonly accepted theoretical methods above rely on an empirically derived equation for α ; however, the common equations for α are typically only valid for a specific range of reduced electric field, or E/N , where N is the electron number density, which may be converted to E/P by using²⁸

$$E/N [\text{Townsend}] = (1.0354 \times 10^{-2} T)(E/p) [\text{V cm}^{-1} \text{ Torr}^{-1}], \quad (4.1)$$

where T is gas temperature in Torr, E is in V/cm, and p is in Torr, to more directly relate to experimental conditions. Common macroscale experimental conditions satisfy this range of E/P ;

however, reducing gap size to microscale creates high electric fields that violate these conditions, necessitating corrections to the standard equations for α .

One such common empirical equation for α/P is given by

$$\left(\frac{\alpha}{p}\right)_{\text{Macroscale}} = A_p \exp\left[-B_p \frac{p}{E}\right], \quad (4.2)$$

where A_p and B_p are empirical constants for inert gases, p is the pressure and E is the applied electric field, given by $E = V/d$, where V is the applied voltage and d is the gap distance, for a planar geometry²⁷. Alternatively, for argon, one may write

$$\left(\frac{\alpha}{p}\right)_{\text{Macroscale}} = C \exp\left[-D \left(\frac{p}{E}\right)^{1/2}\right], \quad (4.3)$$

with $C = 29.2 \text{ cm}^{-1} \text{ Torr}^{-1}$ and $D = 26.6 \text{ V}^{1/2} \text{ cm}^{-1/2} \text{ Torr}^{-1/2}$. However, A_p and B_p (and, similarly, C and D) are only valid over a certain range of E/P and are not necessarily valid for microscale gaps²⁸. Table 4.1 provides typical values of A_p and B_p and the associated range of validity for E/P and E/N .

Table 4.1²⁶: Values for A_p and B_p from Ref. [27], and the E/p and E/N ranges for which they are valid. The E/p range is from Ref. [27] and the E/N range is calculated from (4.3) considering room temperature Ref [28]. Reprinted from A. M. Loveless and A. L. Garner, "A Universal Theory for Gas Breakdown from Microscale to the Classical Paschen Law," *Phys. Plasmas* **24**, 113522 (2017), with Permission from AIP Publishing.

Gas	A_p [$\text{cm}^{-1} \text{ Torr}^{-1}$]	B_p [$\text{V cm}^{-1} \text{ Torr}^{-1}$]	E/p [$\text{V cm}^{-1} \text{ Torr}^{-1}$]	E/N [Td]
Argon	12	180	100-600	~300-1800
Nitrogen	12	342	100-600	~300-1800
Neon	4	100	100-400	~300-1200
Xenon	26	350	200-800	~600-2400
Helium	3	34	20-150	~100-750

One method to correct the ionization coefficient for these strong electric fields involves using XPDP1, 1-D particle-in-cell (PIC) and Monte Carlo collision (MCC) simulation³². By setting gap distance d , V , and p , one can use XPDP1 to determine α from

$$\alpha = \frac{1}{d} \left[\frac{J_{e,\text{anode}}}{J_{e,\text{cathode}}} \right] \quad (4.4)$$

where $J_{e,\text{anode}}$ and $J_{e,\text{cathode}}$ are the current density at the anode and cathode, respectively Figure 4.1 shows an example using PDP1 to determine α/P over a range of E/P that encompassed values both within and outside the accepted range of validity for a 100 μm gap of argon gas with $\gamma_{SE} =$

0.005. A peak α/P exists such that raising or lowering E/P causes less ionization. Prior simulations derived an empirical correction for the standard macroscale equations for α/P as

$$\left(\frac{\alpha}{p}\right) / \left(\frac{\alpha}{p}\right)_{\text{Macroscale}} = \left[1 - \exp \left[- \left(\frac{V/V_{ip} - 1.0}{3.1} \right)^{0.8} \right] \right], \quad (4.5)$$

where V_{ip} is the ionization potential⁶⁹. Figure 4.2 shows more recent PDP1 simulations determining α/P using (4.5) for two different E/N and comparing to this correction. While (4.5) is generally effective, the simulations indicate that it is incomplete as a correction term for a broad range of parameters for a single gas, much less for multiple gases under various gap distances and pressures.

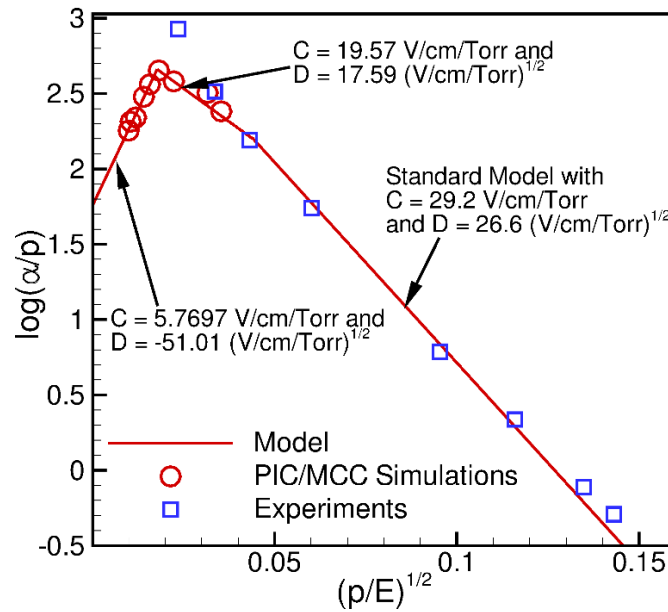


Figure 4.1: Ionization coefficient α/p computed as a function of E/p using one-dimensional PIC-MCC simulations and the corresponding empirical parameters, where E is electric field and p is pressure. The experimental data is obtained indirectly using the breakdown data for 100 μm

based on $\gamma_{SE} = 0.00532$ © [2020] IEEE

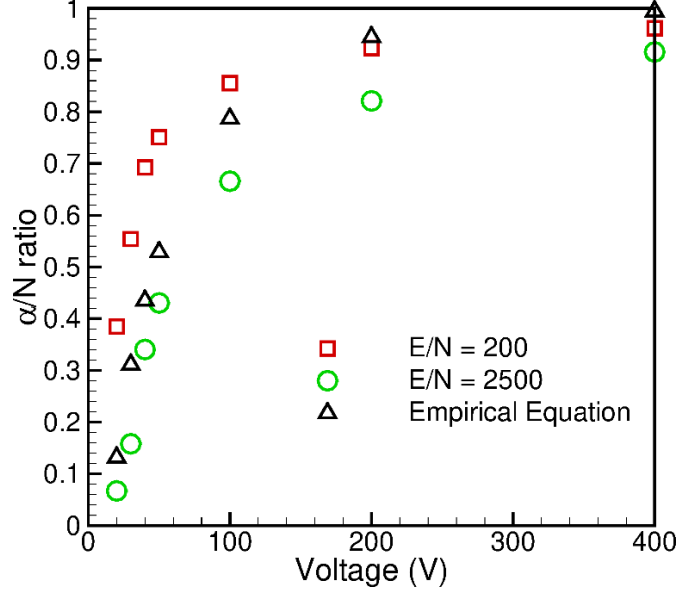


Figure 4.2: Variation of the ratio of microscale to macroscale α/N as a function of applied voltage for all simulations considered in this work. Also included for reference is the variation proposed by the empirical correlation in (4.5) © [2020] IEEE

This chapter expands the range of d, p, V , and gases simulated using PIC/MCC to provide a more comprehensive tabulation of correction factors for α/p as a function of E/p to provide more predictive theories for breakdown at microscale and smaller gaps. This correction will be particularly important in the transition region between field emission and Townsend avalanche, which occurs on the order of a few microns to 10 microns for air at atmospheric pressure^{39,40}. Improving the theory will also help to guide experimental design for nanoscale devices to avoid breakdown or to better predict the voltage to induce plasma formation for small devices for combustion or biotechnology.

4.2 Methods

The simulations to expand the range of simulated E/P followed the methods described in Garner et al.³². The simulations used the PIC/MCC code XPDP1, which uses a planar geometry with the anode at $x = 0$ grounded and the cathode at $x = d$ fixed at a potential V . Electrons are emitted from the cathode with a fixed electron current density^{92,93}. Because we strive to compare the influence of E/P on α for multiple gases, we set our simulation parameters based on nondimensionalized parameters rather than dimensional parameters. As discussed in detail

elsewhere³², nondimensionalization provides several key advantages. First, it makes all variables under consideration “equivalent.” Thus, when one considers a given value as “large,” it is large with respect to unity, regardless of whether one is considering P or E . This allows one to leverage series expansions to mathematically derive asymptotic solutions under various limits. Second, appropriate nondimensionalization can eliminate all material dependence, making the theory independent of material, or universal. Ref. [26] derived exact and asymptotic solutions for the breakdown voltage in the field emission and Townsend avalanche regimes, recovering field emission limits for low ionization ($\alpha d \ll 1$) and recovering a universal Paschen’s law for sufficiently large αd .²⁶

Following the process from Ref. [26], we define the nondimensionalized terms as

$$\begin{aligned}\bar{E} &= EE_*^{-1}, \quad \bar{p} = pp_*^{-1}, \quad \bar{d} = dL^{-1}, \quad \bar{j}_{FN} = j_{FN}j_0^{-1}, \quad \bar{\alpha} = \alpha L, \quad \bar{\phi} = \phi\phi_*^{-1}, \\ \bar{V} &= VV_*^{-1} = VE_*^{-1}L^{-1}\end{aligned}\tag{4.6}$$

with

$$\begin{aligned}p_* &= E_*B_p^{-1}, \quad L = p_*^{-1}A_p^{-1}, \quad j_0 = (A_{FN}E_*^2)/(t^2(y)\phi_*), \\ \phi_* &= [(3.79 \times 10^{-4})^2 B_{FN}]^2, \quad E_* = 0.95B_{FN}\phi_*^{3/2}, \\ V_* &= E_*L = \frac{E_*}{p_*A_p} = \frac{E_*B_p}{E_*A_p} = \frac{B_p}{A_p},\end{aligned}\tag{4.7}$$

where $A_{FN} = 6.2 \times 10^6$ A eV V⁻², $B_{FN} = 6.85 \times 10^9$ V m⁻¹ eV^{-3/2}, $t^2(y) = 1.1$, and the other parameters are given in Table 4.1. Table 4.2 summarizes the resulting scaling parameters for several gases, including the ones considered in this chapter.

Table 4.2: Calculated scaling parameters from (4.7) for argon, nitrogen, neon, xenon, and helium.

Gas	p_* [Torr]	L [m]	j_0 [A/m ²]	ϕ_* [eV]	E_* [V/m]	V_* [V]
Argon	3.44×10^8	2.42×10^{-12}	2.24×10^{18}	96.81	6.20×10^{12}	15
Nitrogen	1.81×10^8	4.60×10^{-12}	2.24×10^{18}	96.81	6.20×10^{12}	28.5
Neon	6.20×10^8	4.03×10^{-12}	2.24×10^{18}	96.81	6.20×10^{12}	25
Xenon	1.77×10^8	2.17×10^{-12}	2.24×10^{18}	96.81	6.20×10^{12}	13.5
Helium	1.82×10^9	1.83×10^{-12}	2.24×10^{18}	96.81	6.20×10^{12}	11.3

To obtain a wide range of p and E for each gas, we fixed $\bar{E}/\bar{p} = 10^{-4}, 10^{-3}, 10^{-2}, 10^{-1}$, and 1 for each pressure and gap distance simulated. We used (4.6) and

(4.7) to convert back to dimensional values for the simulations. We selected a range of dimensional parameters initially: $p = 76$ Torr, 190 Torr, 380 Torr, and 760 Torr and $d = 15$ μm , 5 μm , 1 μm , 0.5 μm , and 0.25 μm for argon and helium. This parametric study requires 100 simulations per gas. Future simulations will further assess the universality of $\bar{\alpha}/\bar{p}$ as a function of \bar{E}/\bar{p} by fixing \bar{p} and \bar{d} instead of p and d and including a third gas (e.g. nitrogen).

For now, this wide parameter space will provide a broad dataset to more comprehensively predict α at extreme values of E/p . We considered 100 cells across the diode for all simulations rather than fixing the size of the spatial discretization since the broad ranges of gap distances considered would lead to inconsistent cell sizes that may lead to either numerical artifacts for unnecessarily large grid or extreme computational expense for unnecessarily small grids. The time step was fixed at 2×10^{-14} s for a total simulation time of 1×10^{-9} s to ensure that the current achieved a steady state across the gap. We fixed the cathode current density at 1000 A/m² to calculate α . We neglected secondary emission and field emission in the simulations to avoid generating electrons due to non-ionization mechanisms and avoid breakdown. Controlling electron generation in this fashion avoids small fluctuations that may occur at lower applied currents that are unrelated to the ionization coefficient, which is the focus of the current simulations. Moreover, this permits us to calculate α at specific points within the gap rather than simply averaging throughout the gap, which may ultimately provide the ability to fully correct for local field changes due to nonuniform space charge.

4.3 Results

The relatively large number of simulations conducted prohibits detailed analyses of each individual condition, so we present the results here for a subset to demonstrate the general trends. Specifically, we consider $p = 76$ Torr, 190 Torr, 380 Torr, and 760 Torr and $d = 15$ μm , 5 μm , and 1 μm for a total of 60 simulations per gas from the larger dataset described in Section 4.2. One consideration, as shown in Figure 4.1, is that increasing or decreasing the electric field can both dramatically reduce α ; therefore, some of the conditions with small gaps may actually induce insufficient α to provide a result if V is either too high or too low. This may also hinder the use of the fixed p and d that we started with. Future efforts exploring \bar{p} and \bar{d} may alleviate this challenge.

Figure 4.3 shows $\ln(\alpha/p)$ as a function of p/E to put the data in the same form of (p/E) to use the more general form of (4.3), which was used in the universal theory unifying PL and field emission for the four different pressures and three different gap distances noted above⁷¹. For $d = 15 \mu\text{m}$ and $5 \mu\text{m}$, α increases to a peak and then decreases with increasing E/p , as demonstrated by previous works for the microscale gaps^{27,28,32}. The behavior for $d = 1 \mu\text{m}$ is more difficult to ascertain. We hypothesize that gap size is becoming sufficiently small at $1 \mu\text{m}$ that using the nondimensional representation to select the simulation parameter space may provide more meaningful results.

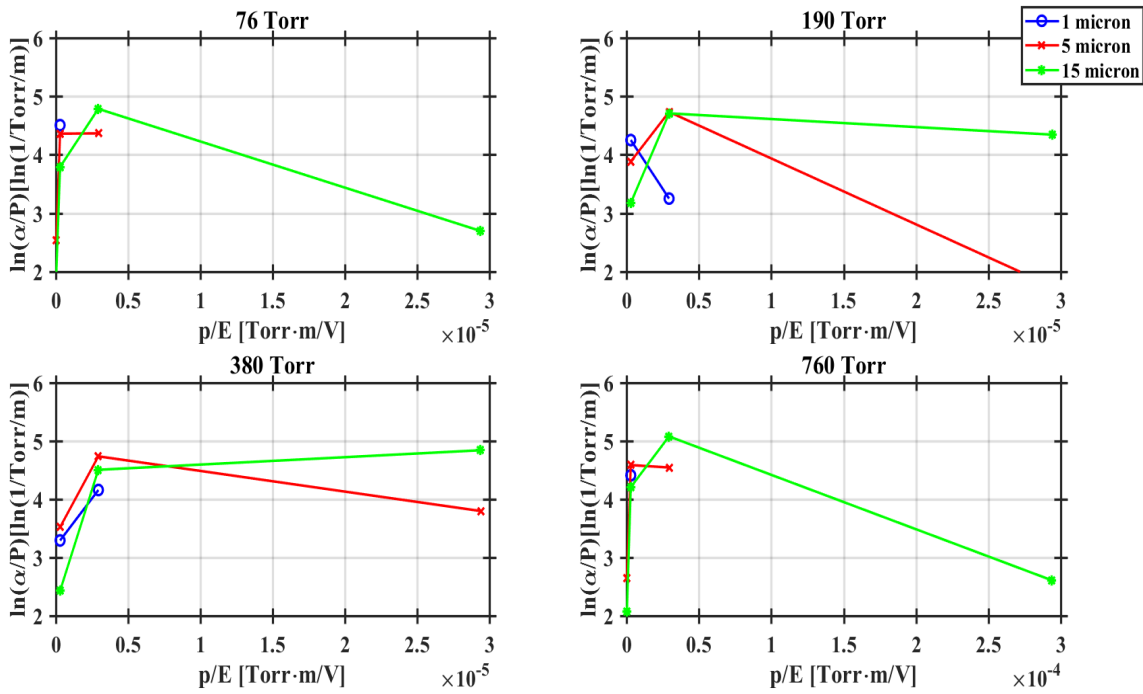


Figure 4.3: Simulation results for $\ln(\alpha/p)$ as a function of the p/E for helium .

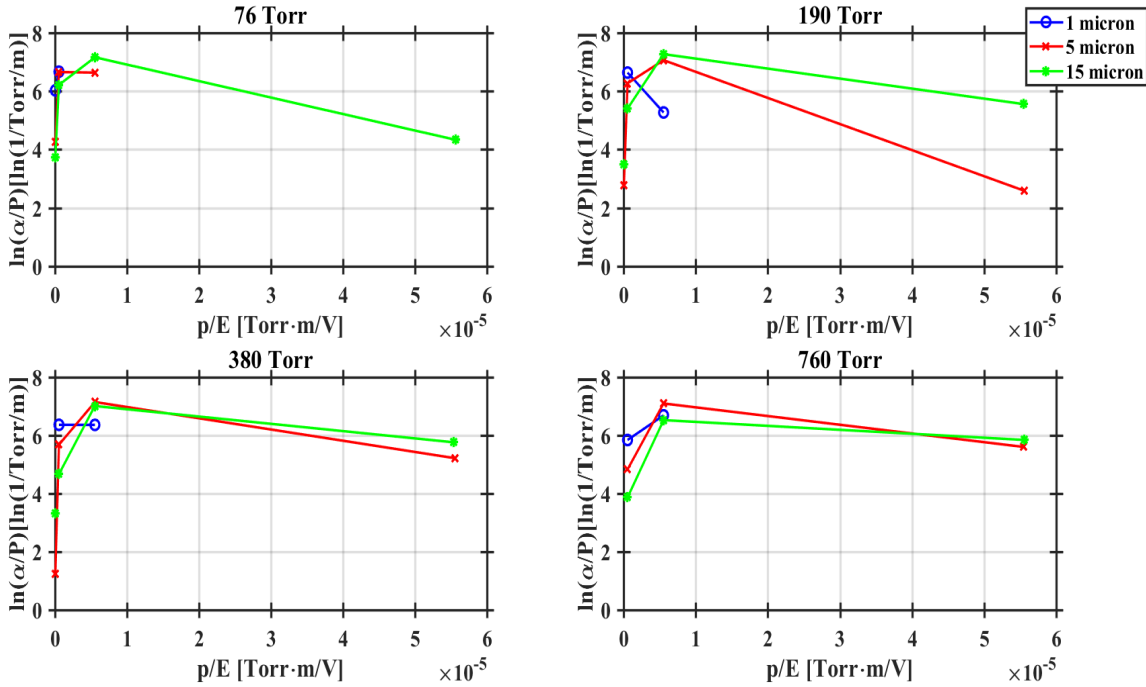


Figure 4.4: Simulation results for $\ln(\alpha/p)$ as a function of the p/E for argon.

Figure 4.4 shows the same analysis for α for argon. Again, α/p decreases with increasing and decreasing E/p after reaching a maximum for $d = 5$ and $15 \mu\text{m}$. As for helium, the reduced ionization at $d = 1 \mu\text{m}$ makes it difficult to ascertain the trend with increasing and decreasing E/p , likely necessitating some other gap distances and voltages for more precise characterization. Increasing pressure appears to influence the peak of the alpha plots, but more data points are needed to fill out the trend.

To directly compare the results across gases, we nondimensionalize the data to eliminate the material dependence on gas and electrode material by using (4.6) and (4.7). Figure 4.5 and Figure 4.6 show the same results as Figure 4.3 and Figure 4.4 in dimensionless units. These figures highlight the importance of fixing \bar{p} , \bar{d} , and \bar{V} for each of the various conditions so that we can directly compare the two gases.

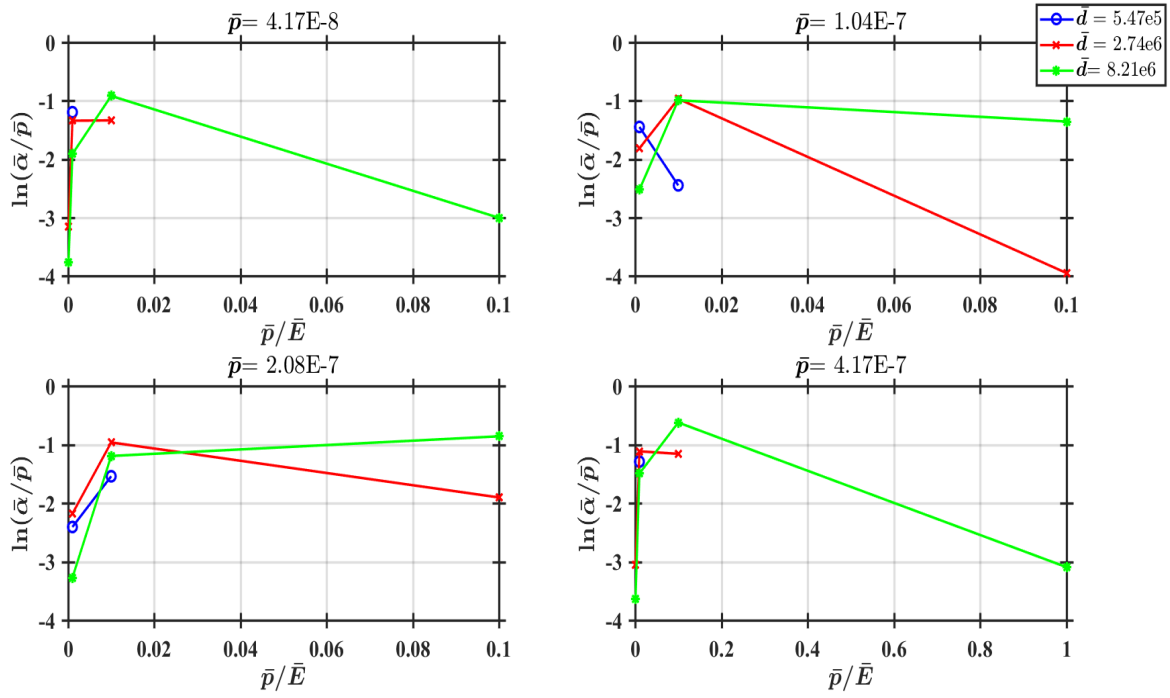


Figure 4.5: Nondimensionalized assessment of $\ln(\bar{\alpha}/\bar{p})$ as a function of \bar{p}/\bar{E} for helium.

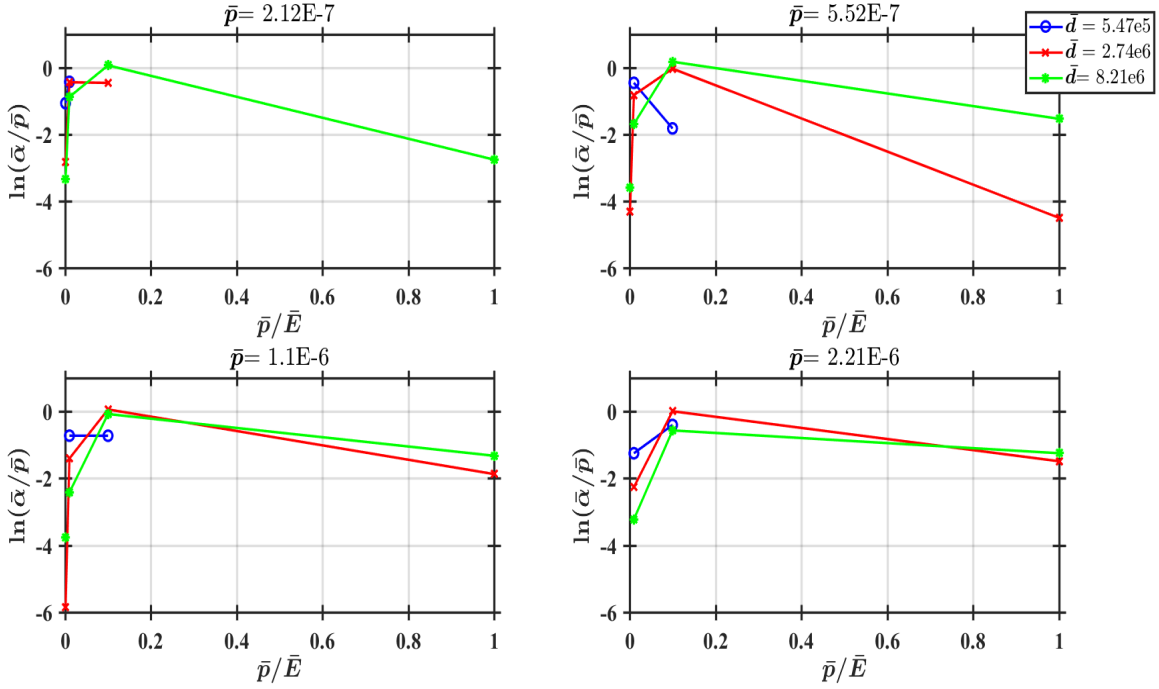


Figure 4.6: Nondimensionalized assessment of $\ln(\bar{\alpha}/\bar{p})$ as a function of \bar{p}/\bar{E} for argon.

4.4 Conclusion

This chapter provides a starting point for acquiring a large dataset to study the behavior of the ionization coefficient for nano- and microscale diodes. The ionization coefficient α is typically found using (4.1), where A_p and B_p are empirical constants for inert gases. However, these constants are only valid over a certain range of E/P and are not necessarily legitimate for use with microscale and nanoscale gaps. The need to better quantify α motivated a large parameter space for PIC/MCC simulations using XPDP1. Argon and helium gases at pressures of 76 Torr, 190 Torr, 380 torr, and 760 Torr were simulated at gaps of 15 μm , 5 μm , and 1 μm for various applied voltages. Figure 4.3 and Figure 4.4 show that α decreases with increasing E/P after a certain point, as previously observed³². To compare the two sets directly, we nondimensionalized the parameters and simulation results using (4.3) to eliminate the dependence on gas and electrode material. Figure 4.6 shows that the dimensional and nondimensionalized results for argon and helium exhibit the same trends. The next step is to simulate argon and helium with common \bar{d} and \bar{p} so that the results are directly comparable to assess the feasibility of obtaining a truly universal relationship for $\bar{\alpha}$.

The current results provide a first order estimate of α for a given set of parameters at the micro and nanoscale with no macroscale assumptions. Increasing pressure influences the peak of the ionization coefficient trends when plotted, but more data points are needed to more accurately determine the peak and assess the trend. Future work will expand both the number of data points and the number of gases simulated to generate a large data set to derive updated semi-empirical relationships to apply to microscale gas breakdown theories³².

5. FUTURE WORK AND CONCLUSION

This dissertation has focused on characterizing the implications of nanoscale features on gas breakdown and electron emission by performing experiments and simulations to guide an improved phenomenological understanding to drive theoretical development and device design. In the process, this dissertation characterizes the changes in gas breakdown at microscale gaps and atmospheric pressure for different degrees of surface roughness, assesses nanoscale gas breakdown for different protrusions and gap distances at atmospheric pressure to characterize electron emission regime and breakdown limits, and performs 1-D PIC-MCC simulations to characterize ionization coefficient at electric fields where common semi-empirical methods fail. The major findings are summarized below, followed by suggestions for future work.

5.1 Summary

Chapter 2 examined the dependence of breakdown voltage on repeated breakdown events for a pin-to-plate configuration at microscale gaps and atmospheric pressure. Figure 2.5 through Figure 2.7 show that the change in breakdown voltage due to surface roughness for a fixed gap distance or due to gap distance for a fixed surface roughness were not statistically significant. The major change in behavior involved the variation in breakdown voltage due to cathode crater formation. AFM and optical imaging before and after the breakdown events showed that the cathodes changed from having average surface feature heights ranging from 0.24 to 1.47 μm before the events to containing small ablated regions with crater depths ranging from 3 to 50 μm (cf. Table 2.2). The combination of initial surface feature height and the ablation/melting of surface material changed the effective gap distance of the system. Cathode crater formation drove the changes by increasing the effective gap distance, which increased breakdown voltage for multiple breakdown events. We observed similar breakdown voltages for similar effective gap distances independent of the interelectrode spacing. Applying a matched asymptotic analysis to the experimental results demonstrated that the breakdown voltage was a function of the effective gap distance and that the transition from field emission to Townsend avalanche occurred at effective gap distances equivalent to the gap distances observed for single breakdown studies^{26,39}. Moreover,

β varied linearly with gap distance in the field emission regime before becoming constant at the transition to the Townsend avalanche, as observed for single breakdown studies³⁹.

Chapter 3 expanded the parameter range from Chapter 2 by going to nanoscale gap distances and examining protrusions with different degrees of sharpness rather than a fixed pin-to-plate geometry. Experiments involved electrical tests similar to reverse bias diode testing, where voltage was applied to the side of the device with the protrusion and leakage current measured across the nano-scale gap of the device. Current (amperes) and voltage (volts) were measured and then examined to demonstrate scaling with the Fowler-Nordheim curve at low voltages for gap distances down to 28 nm. Raising voltage resulted in direct transition from field emission to gas breakdown at 28 nm and 450 nm. For 125 nm gaps, emission began to transition to space-charge limited emission before undergoing gas breakdown. Examining the intersection between the Fowler-Nordheim law for field emission and the Mott-Gurney law for space-charge limited emission with collisions shows that a minimum voltage occurs at ~ 125 nm, which may play a role in the sensitivity of electron emission for this device size.

Chapter 4 summarizes the application of the 1-D PIC/MCC code XPDP1 to obtain a large data set to study the behavior of the ionization coefficient at microscale gap lengths. The ionization coefficient is an important quantity in predicting Townsend avalanche, which is the mechanism that drives Paschen's law. Typically calculated using (4.1), A_p and B_p are empirical constants that are only valid over a certain range of E/P , which is not within the range common for microscale and nanoscale gas breakdown. Thus, to better theoretically predict microscale gas breakdown and guide experimental development and characterization, Chapter 4 focused on using PIC/MCC to determine the ionization coefficient α of argon and helium at pressures of 76 Torr, 190 Torr, 380 torr, and 760 Torr for gaps of 15 μm , 5 μm , and 1 μm . Figure 4.3 and Figure 4.4 show that α decreases with increasing E/P , as observed previously. To directly compare the two gases, we nondimensionalized the parameters to eliminate gas and electrode material dependence by using the appropriate scaling constant from (4.3) and the given simulation parameters. Increasing pressure appears to influence the peak of the ionization coefficient but more data points are needed to fill out the trend. Moreover, simulations need to be performed for multiple gases at the same nondimensionalized pressures and gap distances for several gases to truly determine a universal ionization coefficient for incorporation into microscale gas breakdown theory. Chapter 4 provides the first step in acquiring a sufficiently large dataset to develop this comprehensive theory.

5.2 Future Work

The natural extension of these studies is to explore the dependence of emission as a function of pressure. From one perspective, reducing pressure from atmospheric pressure will reduce the number of gas atoms in the gap, reducing the collisions, and gradually approaching a vacuum type condition at a rate dependent on the gap distance. From a vacuum electronics perspective, any sort of “dirty vacuum” due to leakage will result in increasing pressure. Thus, from either perspective, characterizing emission and breakdown a function of pressure, particularly at nano- and microscale gaps, is critical.

To perform this pressure study, Figure 5.1 shows a new mount for the chips that will allow each device to be directly connected to a probe pin that can be connected to breadboard and chamber fed through for easy measurement. Pin-Grid Arrays (PGA) [Spectrum Semiconductor Materials Inc., California], similar to how the central processing unit mounts (CPU) in commercial computers have been used to wirebond directly to the device pads. Wirebonding to the PGA eliminates the need for a probe station and hand manipulation of the probe electrodes, which minimizes human error and provides a much more stable connection to the devices. A breakout board was custom fabricated [Aries Electronics, Pennsylvania] to mate with the PGA to allow easy connection to the PGA pins. Figure 7 shows these two devices.

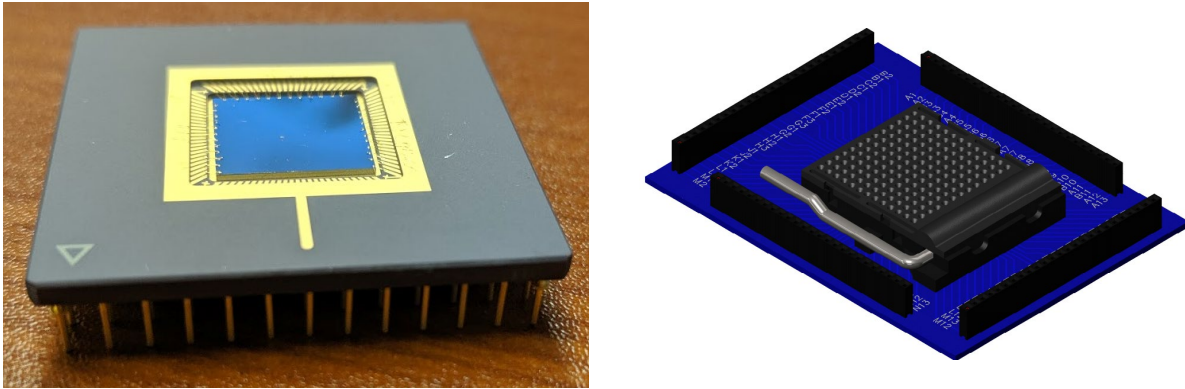


Figure 5.1 New chip carrier with pin connections to connect directly to breadboard/feedthrough for testing.

This new setup will allow for deconvoluting the effects of pressure and work function by selecting different metals, and field enhancement by designing devices with sharp or blunt tips. Controlling more variables allows the deconvolution of their effects to assess their individual importance on the breakdown process.

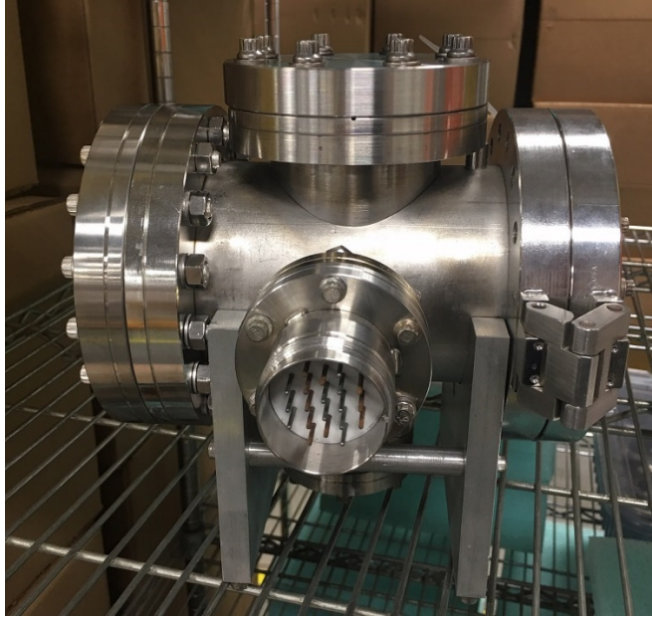


Figure 5.2: New vacuum chamber from Varex Imaging with feed through connections that will allow easy testing of multiple devices.

Figure 5.2 shows a vacuum chamber donated by Varex Imaging with feedthroughs that will be used to connect to the new devices. The new chamber with multiple feedthroughs will allow for multiple devices to be connected directly to a breadboard setup. This will allow for testing at a faster rate than with the traditional probe station. A T-Station 85 from Edwards has been connected to the system to allow for rapid depressurization. The system consists of a roughing pump and turbomolecular pump connected to a controller to automate pumping, as shown in Figure 5.3.

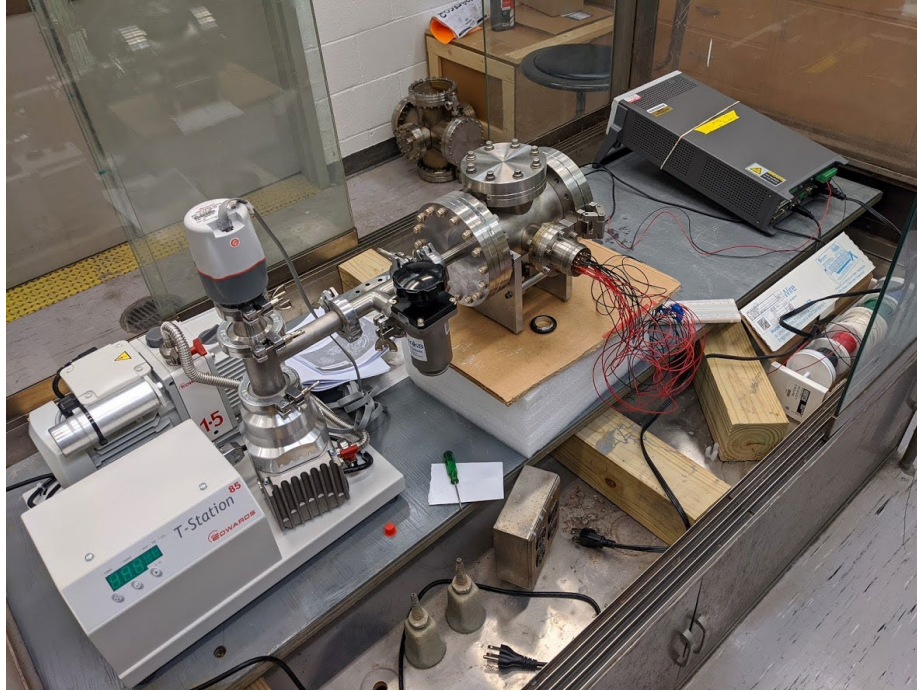


Figure 5.3: Pumping station connected to entire testing system used for benchmarking new device fabrication .

In addition to the devices constructed at Birck Nanotechnology Center in Chapter 3, we have tested devices constructed by the University of Notre Dame and University of Chicago. This also allowed us to test the new SMU and chip/carrier assembly without sacrificing devices to ensure the new test setup functioned properly. Figure 5.4 compares the Notre Dame FN curve (left) and the University of Chicago FN curve (right).

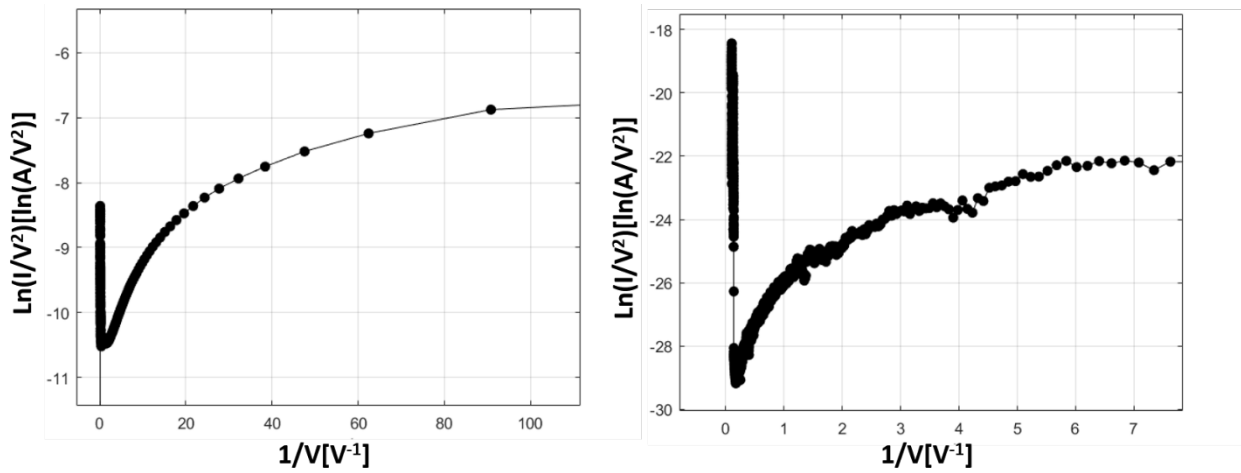


Figure 5.4: Fowler-Nordheim curves for the Notre Dame (left) and University of Chicago (right).

The chip from Notre Dame provided two viable devices that gave FN curves. The curve exhibited a sharp decrease at its minimum, indicating some change in the device during testing. The University of Chicago chips yielded at least eight devices that produced FN curves. The fabrication facility also ran SEM on these devices to ensure tight tolerances on the final devices fabricated. Due to the better quality and design methods of the University of Chicago fabrication process, we selected them to fabricate the actual devices to replicate testing of the electron emission transition. The testing of initial devices was performed flawlessly at atmospheric pressure. Table 5.1 summarizes the parameter space requested for devices with shape shown in Figure 5.1.

Table 5.1: Parameter space for variable listed in Figure 3.1.

d_{eff} (nm)	h (nm)	d (nm)	a/h	a (nm)	α (deg)
20	500	520	0.05	25	45
40		540	0.25	125	
60		560	1	500	
100		600			
200		700			
250		750			
300		800			
400		900			
700		1200			
800		1300			

Five replicates at ten different d_{eff} and three values of a with five replicates will be constructed for a total of 150 devices. We are having this done twice for a total of 300 devices on six carriers so we can run a set of five replicates at atmospheric pressure and a set of five at rough vacuum pressure. Fabrication issues at the University of Chicago and COVID-19 delayed completion of fabrication and delivery. Although initial benchmarking of system operation was successful, the full parametric study will be completed in future work.

Another important consideration in these experiments is the impact of heating the electrodes, which may happen either due to thermionic emission or due to general heating during voltage application. This motivates interest in specifically characterizing the impact of cathode heating and thermionic emission on breakdown and emission regime transition⁷⁶. Figure 5.5 shows

a proposed experimental setup for testing emission under increased temperature conditions using the same electrode design as in previous experiments. We propose to use a cathode material capable of undergoing thermionic emission, such as thoriated tungsten, which is robust to air for transport and for considering the behavior as a function of both temperature and pressure. The anode would most likely be made of gold or another standard material depending upon fabrication convenience and availability. We then have an electrical insulation material (SiO_2) and a silicon substrate layer.

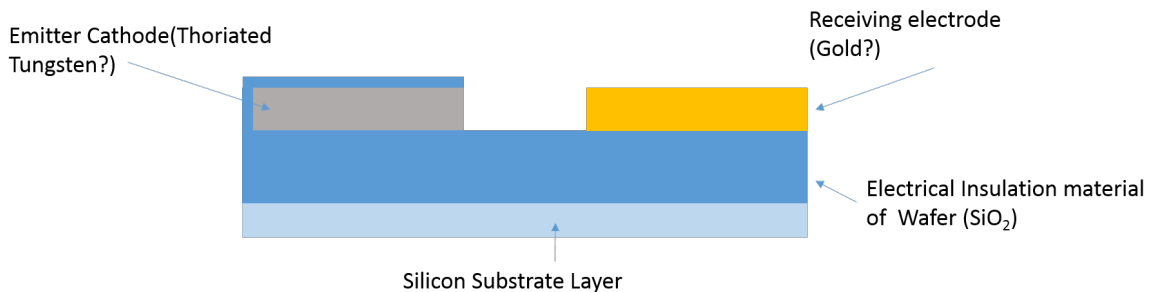


Figure 5.5: Proposed nanoscale chip design for thermionic emission experiments.

The proposed future work will expand the base laid out in Chapters 2 and 4, as well as the group's theoretical work^{32,54,76,94} incorporating more forms of electron emission into the theories for breakdown and electron emission. Currently, predicting breakdown for microscale and smaller devices requires complicated simulations, semi-empirical fitting parameters, or prior knowledge for a very specific set of experimental conditions. This dissertation has extended experimental understanding of breakdown and electron emission from 28 nm to microscale and provided the ground work for better characterizing ionization coefficient to more accurately represent the physical conditions. This work and the proposed experiments above will provide a way to couple all relevant phenomena, including heating, surface modification, protrusion shape, and electric field driven ionization, into a standard theory to guide nano- and microdevice design.

APPENDIX A. NANOSCALE DATA PROCESSING

The data was imported and processed using the following MATLAB script to construct the Fowler-Nordheim plots.

Contents

- [Initialize](#)
- [Separate and average data](#)
- [GAP PLOTS](#)
- [Width PLOTS](#)

user guide:

```
clear all

fontsize=24;
labelfontsize=18;
legendFontSize=16;
markerSize=8;
markerSize2=11;
lineWidth=2;
lineWidth2=2;
markerWidth=1.1;
fontname='Times New Roman';
ticky=0.015;
tickx=0.015;
```

Initialize

```
myfile1 = 'C:\Users\rbray\Google Drive\Research\ONR_YIP\Nano
data\air\Birck\chip3_4_27_2020'; %Change the file directory when plotting another series
of data
fileList1 = dir(fullfile(myfile1, '*.csv'));
num_files = length(fileList1);

T = 0;
```

Separate and average data

```
%This part imports the data
for(T = 1:1:num_files)
    name1 = strcat(fullfile(fileList1(T).folder, "\", fileList1(T).name);
    file1 = csvread(name1,0,0); % read the file
    volt_all(T).name=fileList1(T).name;
    volt_all(T).data=file1(:,1);
    current_all(T).name = fileList1(T).name;
```

```

current_all(T).data=file1(:,2);
end

%This section separates the data into cell structures
for(x = 1:1:40)
    q=1;
    current(x).name = num2str(x);
    volt(x).name= num2str(x);
    for(T = 1:1:num_files)
        if(length(current_all(T).name) == 9)
            if(str2num(current_all(T).name(1:end-8)) == x)
                current(x).data{q}=current_all(T).data;
                volt(x).data{q}=volt_all(T).data;
                q=q+1;
            end
        end
        if(length(current_all(T).name) == 10)
            if(str2num(current_all(T).name(1:end-8)) == x)
                current(x).data{q}=current_all(T).data;
                volt(x).data{q}=volt_all(T).data;
                q=q+1;
            end
        end
    end
end

%Makes all data vectors the same length by adding NaN to vectors that are
%too shrot
for (x=1:1:40)
    for (t=1:1:length(current(x).data))
        curlength(t) = length(current(x).data{t});
    end

    for (t=1:1:length(volt(x).data))
        vollength(t) = length(volt(x).data{t});
    end

    maxcur=max(curlength);
    maxvol=max(vollength);

    for (t=1:1:length(current(x).data))
        current(x).data{t}(length(current(x).data{t})+1:maxcur) = NaN;
    end

    for (t=1:1:length(volt(x).data))
        volt(x).data{t}(length(volt(x).data{t})+1:maxvol) = NaN;
    end
end

```

```

clear curlength
clear vollength

end

%Averages the runs for each set of replicates together
for(x=1:1:40)
    avg_current{x}=mean(cell2mat(current(x).data),2);
    temp=cell2mat(current(x).data);
    bars{x}=std(temp,0,2);
    clear temp
    avg_vol{x}=mean(cell2mat(volt(x).data),2);
end
d=[230 230      230      230      230      500      500      500      500      750
    750      750      950      900      115      145      115      115      250
    250      250      375      375      375      450      450      57      125
    57      125      187      225      57      126      187      28      62
    28      62      93];

a=[384  76      38      192      769      50      125      250      500      62
   125      250      100      100      38      96      192      384      62
   125      250      31      62      125      25      50      48      31
   96      62      31      25      192      125      62      48      62
   96      31      31];

```

GAP PLOTS

```

x=[100 32 121];%identifies indivisual data in _all variables
f=[33 17 4]; %gap from device #
% x=[107];%identifies indivisual data in _all variables
% f=[36]; %gap from device #

for t=1:length(f)
str{t}=strcat('gap = ',num2str(d(f(t))),'nm');
end

for p=1:length(x)
semilogx(1./ (volt_all(x(p)).data),log(movmean(current_all(x(p)).data,200)./volt_all(x(
p)).data.^2),'-x','LineWidth',lineWidth,'MarkerSize',markerSize)
set(gca,'linewidth',lineWidth,'TickDir','both','TickLength',
[tickx,ticky],'XMinorTick','off','YMinorTick',
'off','FontName',fontname,'FontSize',fontsize,'FontWeight','bold')
hold on
end
title("FN Curve");
ylabel('ln(I/V^{2}) [A/V^{2}]','Interpreter','tex')
xlabel('1/V','Interpreter','tex')

```

```

legend(str);
grid on;

figure

for p=1:length(x)
semilogx(volt_all(x(p)).data.^2,movmean(current_all(x(p)).data,5),'-
o','LineWidth',lineWidth,'MarkerSize',markerSize);
hold on
end
title("MG Curve");
xlabel('V^{3/2} [V^2]','Interpreter','tex');
legend(str)
ylabel('I [A]','Interpreter','tex');
set(gca,'linewidth',lineWidth,'TickDir','both','TickLength',
[tickx,ticky],'XMinorTick','off','YMinorTick',
'off','FontName',fontname,'FontSize',fontsize,'FontWeight','bold')
grid on;

figure

for p=1:length(x)
plot(volt_all(x(p)).data,movmean(current_all(x(p)).data,5),'-
o','LineWidth',lineWidth,'MarkerSize',markerSize);
hold on
end
title("IV Curve");
xlabel('V [V]','Interpreter','tex');
legend(str)
ylabel('I [A]','Interpreter','tex');
set(gca,'linewidth',lineWidth,'TickDir','both','TickLength',
[tickx,ticky],'XMinorTick','off','YMinorTick',
'off','FontName',fontname,'FontSize',fontsize,'FontWeight','bold')
grid on;

% old figures kept just in case they are needed again
%
% loglog(avg_vol{x(p)}.^(3/2),avg_current{x(p)},'-ko','markerfacecolor','k');
% hold on
% loglog(avg_vol{x(q)}.^(3/2),avg_current{x(q)},'-go','markerfacecolor','g');
% hold on
% loglog(avg_vol{x(r)}.^(3/2),avg_current{x(r)},'-ro','markerfacecolor','r');
% title("CL Curve");
% xlabel('V^{3/2} [V^{3/2}]','Interpreter','tex');
% legend(strcat('gap = ',num2str(d(p)*10^9),'{ /a = }',num2str(a(p))),strcat('gap =
',num2str(d(q)*10^9),'{ /a = }',num2str(a(q))),strcat('gap = ',num2str(d(r)*10^9),'{ /a
= }',num2str(a(r))))
% ylabel('I [A]','Interpreter','Latex');
% grid on;
%
% figure

```

```

%
% loglog(avg_vol{x(p)},avg_current{x(p)},'-ko')
% hold on
% loglog(avg_vol{x(q)},avg_current{x(q)},'-go')
% hold on
% loglog(avg_vol{x(r)},avg_current{x(r)},'-ro')
% title("LOGLOG IV");
% xlabel('V[V]','Interpreter','tex');
% legend(strcat('gap = ',num2str(d(p)*10^9),'{ /a = }',num2str(a(p))),strcat('gap = ',num2str(d(q)*10^9),'{ /a = }',num2str(a(q))),strcat('gap = ',num2str(d(r)*10^9),'{ /a = }',num2str(a(r))))
% ylabel('I[A]','Interpreter','tex');
% grid on;

% figure
%
% plot(avg_vol{x(p)},avg_current{x(p)},'-ko')
% hold on
% plot(avg_vol{x(q)},avg_current{x(q)},'-go')
% hold on
% plot(avg_vol{x(r)},avg_current{x(r)},'-ro')
% title("IV");
% xlabel('Log(V) [V]','Interpreter','tex');
% legend(strcat('gap = ',num2str(d(p)*10^9),'{ /a = }',num2str(a(p))),strcat('gap = ',num2str(d(q)*10^9),'{ /a = }',num2str(a(q))),strcat('gap = ',num2str(d(r)*10^9),'{ /a = }',num2str(a(r))))
% ylabel('Log(I) [A]','Interpreter','tex');
% grid on;

```

Width PLOTS

```

clear x f str t
x=[26 33 37];

f=[15 17 18]; %width trend
for t=1:length(f)
str{t}=strcat('a = ',num2str(a(f(t))),'nm');
end

figure

for p=1:length(x)
semilogx(1./(volt_all(x(p)).data),log(movmean(current_all(x(p)).data,200)./volt_all(x(p)).data.^2),'-x','LineWidth',lineWidth,'MarkerSize',markerSize)
hold on
end
title("FN Curve");
ylabel('ln(I/V^{2}) [A/V^{2}]','Interpreter','tex')
xlabel('1/V','Interpreter','tex')

```

```

set(gca,'linewidth',lineWidth,          'TickDir',          'both',          'TickLength',
[tickx,ticky],'XMinorTick',            'off',            'YMinorTick',
'off','FontName',fontname,'FontSize',fontsize,'FontWeight','bold')
legend(str);
grid on;

figure

for p=1:length(x)
semilogx(volt_all(x(p)).data.^2,movmean(current_all(x(p)).data,5),'-
o','LineWidth',lineWidth,'MarkerSize',markerSize);
hold on
end
title("MG Curve");
xlabel('V^{3/2} [V^{2}]','Interpreter','tex');
legend(str)
ylabel('I [A]','Interpreter','tex');
set(gca,'linewidth',lineWidth,          'TickDir',          'both',          'TickLength',
[tickx,ticky],'XMinorTick',            'off',            'YMinorTick',
'off','FontName',fontname,'FontSize',fontsize,'FontWeight','bold')
grid on;

figure

for p=1:length(x)
plot(volt_all(x(p)).data,movmean(current_all(x(p)).data,5),'-
o','LineWidth',lineWidth,'MarkerSize',markerSize);
hold on
end
title("IV Curve");
xlabel('V [V]','Interpreter','tex');
legend(str)
ylabel('I [A]','Interpreter','tex');
set(gca,'linewidth',lineWidth,          'TickDir',          'both',          'TickLength',
[tickx,ticky],'XMinorTick',            'off',            'YMinorTick',
'off','FontName',fontname,'FontSize',fontsize,'FontWeight','bold')
grid on;

```

Published with MATLAB® R2017a

APPENDIX B. PIC/MCC SIMULATION PARAMETERS

Table A.B.2 presents the entire simulation space for argon that created the large data set for ionization coefficient with nondimensional constants.

Table A.B.2: Parameter space used to create argon simulations and nondimensional constants.

Gap (m)	Pressure (Torr)	L (m)	Pstar (Torr)	Vstar (V)	Pb	db	Pb*db/Vb	Vb	V (Volts)	pb/Eb
2.50E-07	76	2.42E-12	3.44E+08	1.50E+01	2.21E-07	1.03E+05	1.00E-04	2.28E+02	3.42E+03	1.00E-04
2.50E-07	76	2.42E-12	3.44E+08	1.50E+01	2.21E-07	1.03E+05	1.00E-03	2.28E+01	3.42E+02	1.00E-03
2.50E-07	76	2.42E-12	3.44E+08	1.50E+01	2.21E-07	1.03E+05	1.00E-02	2.28E+00	3.42E+01	1.00E-02
2.50E-07	76	2.42E-12	3.44E+08	1.50E+01	2.21E-07	1.03E+05	1.00E-01	2.28E+01	3.42E+00	1.00E-01
2.50E-07	76	2.42E-12	3.44E+08	1.50E+01	2.21E-07	1.03E+05	1.00E+00	2.28E-02	3.42E-01	1.00E+00
2.50E-07	190	2.42E-12	3.44E+08	1.50E+01	5.52E-07	1.03E+05	1.00E-04	5.71E+02	8.56E+03	1.00E-04
2.50E-07	190	2.42E-12	3.44E+08	1.50E+01	5.52E-07	1.03E+05	1.00E-03	5.71E+01	8.56E+02	1.00E-03
2.50E-07	190	2.42E-12	3.44E+08	1.50E+01	5.52E-07	1.03E+05	1.00E-02	5.71E+00	8.56E+01	1.00E-02
2.50E-07	190	2.42E-12	3.44E+08	1.50E+01	5.52E-07	1.03E+05	1.00E-01	5.71E-01	8.56E+00	1.00E-01
2.50E-07	190	2.42E-12	3.44E+08	1.50E+01	5.52E-07	1.03E+05	1.00E+00	5.71E-02	8.56E-01	1.00E+00
2.50E-07	380	2.42E-12	3.44E+08	1.50E+01	1.10E-06	1.03E+05	1.00E-04	1.14E+03	1.71E+04	1.00E-04
2.50E-07	380	2.42E-12	3.44E+08	1.50E+01	1.10E-06	1.03E+05	1.00E-03	1.14E+02	1.71E+03	1.00E-03
2.50E-07	380	2.42E-12	3.44E+08	1.50E+01	1.10E-06	1.03E+05	1.00E-02	1.14E+01	1.71E+02	1.00E-02
2.50E-07	380	2.42E-12	3.44E+08	1.50E+01	1.10E-06	1.03E+05	1.00E-01	1.14E+00	1.71E+01	1.00E-01
2.50E-07	380	2.42E-12	3.44E+08	1.50E+01	1.10E-06	1.03E+05	1.00E+00	1.14E-01	1.71E+00	1.00E+00
2.50E-07	760	2.42E-12	3.44E+08	1.50E+01	2.21E-06	1.03E+05	1.00E-04	2.28E+03	3.42E+04	1.00E-04
2.50E-07	760	2.42E-12	3.44E+08	1.50E+01	2.21E-06	1.03E+05	1.00E-03	2.28E+02	3.42E+03	1.00E-03
2.50E-07	760	2.42E-12	3.44E+08	1.50E+01	2.21E-06	1.03E+05	1.00E-02	2.28E+01	3.42E+02	1.00E-02
2.50E-07	760	2.42E-12	3.44E+08	1.50E+01	2.21E-06	1.03E+05	1.00E-01	2.28E+00	3.42E+01	1.00E-01
2.50E-07	760	2.42E-12	3.44E+08	1.50E+01	2.21E-06	1.03E+05	1.00E+00	2.28E-01	3.42E+00	1.00E+00
5.00E-07	76	2.42E-12	3.44E+08	1.50E+01	2.21E-07	2.07E+05	1.00E-04	4.56E+02	6.85E+03	1.00E-04
5.00E-07	76	2.42E-12	3.44E+08	1.50E+01	2.21E-07	2.07E+05	1.00E-03	4.56E+01	6.85E+02	1.00E-03
5.00E-07	76	2.42E-12	3.44E+08	1.50E+01	2.21E-07	2.07E+05	1.00E-02	4.56E+00	6.85E+01	1.00E-02
5.00E-07	76	2.42E-12	3.44E+08	1.50E+01	2.21E-07	2.07E+05	1.00E-01	4.56E-01	6.85E+00	1.00E-01
5.00E-07	76	2.42E-12	3.44E+08	1.50E+01	2.21E-07	2.07E+05	1.00E+00	4.56E-02	6.85E-01	1.00E+00
5.00E-07	190	2.42E-12	3.44E+08	1.50E+01	5.52E-07	2.07E+05	1.00E-04	1.14E+03	1.71E+04	1.00E-04
5.00E-07	190	2.42E-12	3.44E+08	1.50E+01	5.52E-07	2.07E+05	1.00E-03	1.14E+02	1.71E+03	1.00E-03
5.00E-07	190	2.42E-12	3.44E+08	1.50E+01	5.52E-07	2.07E+05	1.00E-02	1.14E+01	1.71E+02	1.00E-02
5.00E-07	190	2.42E-12	3.44E+08	1.50E+01	5.52E-07	2.07E+05	1.00E-01	1.14E+00	1.71E+01	1.00E-01
5.00E-07	190	2.42E-12	3.44E+08	1.50E+01	5.52E-07	2.07E+05	1.00E+00	1.14E-01	1.71E+00	1.00E+00
5.00E-07	380	2.42E-12	3.44E+08	1.50E+01	1.10E-06	2.07E+05	1.00E-04	2.28E+03	3.42E+04	1.00E-04
5.00E-07	380	2.42E-12	3.44E+08	1.50E+01	1.10E-06	2.07E+05	1.00E-03	2.28E+02	3.42E+03	1.00E-03
5.00E-07	380	2.42E-12	3.44E+08	1.50E+01	1.10E-06	2.07E+05	1.00E-02	2.28E+01	3.42E+02	1.00E-02
5.00E-07	380	2.42E-12	3.44E+08	1.50E+01	1.10E-06	2.07E+05	1.00E-01	2.28E+00	3.42E+01	1.00E-01
5.00E-07	380	2.42E-12	3.44E+08	1.50E+01	1.10E-06	2.07E+05	1.00E+00	2.28E-01	3.42E+00	1.00E+00
5.00E-07	760	2.42E-12	3.44E+08	1.50E+01	2.21E-06	2.07E+05	1.00E-04	4.56E+03	6.85E+04	1.00E-04
5.00E-07	760	2.42E-12	3.44E+08	1.50E+01	2.21E-06	2.07E+05	1.00E-03	4.56E+02	6.85E+03	1.00E-03
5.00E-07	760	2.42E-12	3.44E+08	1.50E+01	2.21E-06	2.07E+05	1.00E-02	4.56E+01	6.85E+02	1.00E-02
5.00E-07	760	2.42E-12	3.44E+08	1.50E+01	2.21E-06	2.07E+05	1.00E-01	4.56E+00	6.85E+01	1.00E-01
5.00E-07	760	2.42E-12	3.44E+08	1.50E+01	2.21E-06	2.07E+05	1.00E+00	4.56E-01	6.85E+00	1.00E+00
1.00E-06	76	2.42E-12	3.44E+08	1.50E+01	2.21E-07	4.13E+05	1.00E-04	9.13E+02	1.37E+04	1.00E-04
1.00E-06	76	2.42E-12	3.44E+08	1.50E+01	2.21E-07	4.13E+05	1.00E-03	9.13E+01	1.37E+03	1.00E-03
1.00E-06	76	2.42E-12	3.44E+08	1.50E+01	2.21E-07	4.13E+05	1.00E-02	9.13E+00	1.37E+02	1.00E-02
1.00E-06	76	2.42E-12	3.44E+08	1.50E+01	2.21E-07	4.13E+05	1.00E-01	9.13E-01	1.37E+01	1.00E-01
1.00E-06	76	2.42E-12	3.44E+08	1.50E+01	2.21E-07	4.13E+05	1.00E+00	9.13E-02	1.37E+00	1.00E+00
1.00E-06	190	2.42E-12	3.44E+08	1.50E+01	5.52E-07	4.13E+05	1.00E-04	2.28E+03	3.42E+04	1.00E-04
1.00E-06	190	2.42E-12	3.44E+08	1.50E+01	5.52E-07	4.13E+05	1.00E-03	2.28E+02	3.42E+03	1.00E-03
1.00E-06	190	2.42E-12	3.44E+08	1.50E+01	5.52E-07	4.13E+05	1.00E-02	2.28E+01	3.42E+02	1.00E-02
1.00E-06	190	2.42E-12	3.44E+08	1.50E+01	5.52E-07	4.13E+05	1.00E-01	2.28E+00	3.42E+01	1.00E-01
1.00E-06	190	2.42E-12	3.44E+08	1.50E+01	5.52E-07	4.13E+05	1.00E+00	2.28E-01	3.42E+00	1.00E+00

Table A.B.1 Continued.

Gap (m)	Pressure (Torr)	L (m)	Pstar (Torr)	Vstar (V)	Pb	db	Pb*db/Vb	Vb	V (Volts)	pb/Eb
1.00E-06	380	2.42E-12	3.44E+08	1.50E+01	1.10E-06	4.13E+05	1.00E-04	4.56E+03	6.85E+04	1.00E-04
1.00E-06	380	2.42E-12	3.44E+08	1.50E+01	1.10E-06	4.13E+05	1.00E-03	4.56E+02	6.85E+03	1.00E-03
1.00E-06	380	2.42E-12	3.44E+08	1.50E+01	1.10E-06	4.13E+05	1.00E-02	4.56E+01	6.85E+02	1.00E-02
1.00E-06	380	2.42E-12	3.44E+08	1.50E+01	1.10E-06	4.13E+05	1.00E-01	4.56E+00	6.85E+01	1.00E-01
1.00E-06	380	2.42E-12	3.44E+08	1.50E+01	1.10E-06	4.13E+05	1.00E+00	4.56E-01	6.85E+00	1.00E+00
1.00E-06	760	2.42E-12	3.44E+08	1.50E+01	2.21E-06	4.13E+05	1.00E-04	9.13E+03	1.37E+05	1.00E-04
1.00E-06	760	2.42E-12	3.44E+08	1.50E+01	2.21E-06	4.13E+05	1.00E-03	9.13E+02	1.37E+04	1.00E-03
1.00E-06	760	2.42E-12	3.44E+08	1.50E+01	2.21E-06	4.13E+05	1.00E-02	9.13E+01	1.37E+03	1.00E-02
1.00E-06	760	2.42E-12	3.44E+08	1.50E+01	2.21E-06	4.13E+05	1.00E-01	9.13E+00	1.37E+02	1.00E-01
1.00E-06	760	2.42E-12	3.44E+08	1.50E+01	2.21E-06	4.13E+05	1.00E+00	9.13E-01	1.37E+01	1.00E+00
5.00E-06	76	2.42E-12	3.44E+08	1.50E+01	2.21E-07	2.07E+06	1.00E-04	4.56E+03	6.85E+04	1.00E-04
5.00E-06	76	2.42E-12	3.44E+08	1.50E+01	2.21E-07	2.07E+06	1.00E-03	4.56E+02	6.85E+03	1.00E-03
5.00E-06	76	2.42E-12	3.44E+08	1.50E+01	2.21E-07	2.07E+06	1.00E-02	4.56E+01	6.85E+02	1.00E-02
5.00E-06	76	2.42E-12	3.44E+08	1.50E+01	2.21E-07	2.07E+06	1.00E-01	4.56E+00	6.85E+01	1.00E-01
5.00E-06	76	2.42E-12	3.44E+08	1.50E+01	2.21E-07	2.07E+06	1.00E+00	4.56E-01	6.85E+00	1.00E+00
5.00E-06	190	2.42E-12	3.44E+08	1.50E+01	5.52E-07	2.07E+06	1.00E-04	1.14E+04	1.71E+05	1.00E-04
5.00E-06	190	2.42E-12	3.44E+08	1.50E+01	5.52E-07	2.07E+06	1.00E-03	1.14E+03	1.71E+04	1.00E-03
5.00E-06	190	2.42E-12	3.44E+08	1.50E+01	5.52E-07	2.07E+06	1.00E-02	1.14E+02	1.71E+03	1.00E-02
5.00E-06	190	2.42E-12	3.44E+08	1.50E+01	5.52E-07	2.07E+06	1.00E-01	1.14E+01	1.71E+02	1.00E-01
5.00E-06	190	2.42E-12	3.44E+08	1.50E+01	5.52E-07	2.07E+06	1.00E+00	1.14E+00	1.71E+01	1.00E+00
5.00E-06	380	2.42E-12	3.44E+08	1.50E+01	1.10E-06	2.07E+06	1.00E-04	2.28E+04	3.42E+05	1.00E-04
5.00E-06	380	2.42E-12	3.44E+08	1.50E+01	1.10E-06	2.07E+06	1.00E-03	2.28E+03	3.42E+04	1.00E-03
5.00E-06	380	2.42E-12	3.44E+08	1.50E+01	1.10E-06	2.07E+06	1.00E-02	2.28E+02	3.42E+03	1.00E-02
5.00E-06	380	2.42E-12	3.44E+08	1.50E+01	1.10E-06	2.07E+06	1.00E-01	2.28E+01	3.42E+02	1.00E-01
5.00E-06	380	2.42E-12	3.44E+08	1.50E+01	1.10E-06	2.07E+06	1.00E+00	2.28E+00	3.42E+01	1.00E+00
5.00E-06	760	2.42E-12	3.44E+08	1.50E+01	2.21E-06	2.07E+06	1.00E-04	4.56E+04	6.85E+05	1.00E-04
5.00E-06	760	2.42E-12	3.44E+08	1.50E+01	2.21E-06	2.07E+06	1.00E-03	4.56E+03	6.85E+04	1.00E-03
5.00E-06	760	2.42E-12	3.44E+08	1.50E+01	2.21E-06	2.07E+06	1.00E-02	4.56E+02	6.85E+03	1.00E-02
5.00E-06	760	2.42E-12	3.44E+08	1.50E+01	2.21E-06	2.07E+06	1.00E-01	4.56E+01	6.85E+02	1.00E-01
5.00E-06	760	2.42E-12	3.44E+08	1.50E+01	2.21E-06	2.07E+06	1.00E+00	4.56E+00	6.85E+01	1.00E+00
1.50E-05	76	2.42E-12	3.44E+08	1.50E+01	2.21E-07	6.20E+06	1.00E-04	1.37E+03	2.05E+05	1.00E-04
1.50E-05	76	2.42E-12	3.44E+08	1.50E+01	2.21E-07	6.20E+06	1.00E-03	1.37E+03	2.05E+04	1.00E-03
1.50E-05	76	2.42E-12	3.44E+08	1.50E+01	2.21E-07	6.20E+06	1.00E-02	1.37E+02	2.05E+03	1.00E-02
1.50E-05	76	2.42E-12	3.44E+08	1.50E+01	2.21E-07	6.20E+06	1.00E-01	1.37E+01	2.05E+02	1.00E-01
1.50E-05	76	2.42E-12	3.44E+08	1.50E+01	2.21E-07	6.20E+06	1.00E+00	1.37E+00	2.05E+01	1.00E+00
1.50E-05	190	2.42E-12	3.44E+08	1.50E+01	5.52E-07	6.20E+06	1.00E-04	3.42E+04	5.14E+05	1.00E-04
1.50E-05	190	2.42E-12	3.44E+08	1.50E+01	5.52E-07	6.20E+06	1.00E-03	3.42E+03	5.14E+04	1.00E-03
1.50E-05	190	2.42E-12	3.44E+08	1.50E+01	5.52E-07	6.20E+06	1.00E-02	3.42E+02	5.14E+03	1.00E-02
1.50E-05	190	2.42E-12	3.44E+08	1.50E+01	5.52E-07	6.20E+06	1.00E-01	3.42E+01	5.14E+02	1.00E-01
1.50E-05	190	2.42E-12	3.44E+08	1.50E+01	5.52E-07	6.20E+06	1.00E+00	3.42E+00	5.14E+01	1.00E+00
1.50E-05	380	2.42E-12	3.44E+08	1.50E+01	1.10E-06	6.20E+06	1.00E-04	6.85E+04	1.03E+06	1.00E-04
1.50E-05	380	2.42E-12	3.44E+08	1.50E+01	1.10E-06	6.20E+06	1.00E-03	6.85E+03	1.03E+05	1.00E-03
1.50E-05	380	2.42E-12	3.44E+08	1.50E+01	1.10E-06	6.20E+06	1.00E-02	6.85E+02	1.03E+04	1.00E-02
1.50E-05	380	2.42E-12	3.44E+08	1.50E+01	1.10E-06	6.20E+06	1.00E-01	6.85E+01	1.03E+03	1.00E-01
1.50E-05	380	2.42E-12	3.44E+08	1.50E+01	1.10E-06	6.20E+06	1.00E+00	6.85E+00	1.03E+02	1.00E+00
1.50E-05	760	2.42E-12	3.44E+08	1.50E+01	2.21E-06	6.20E+06	1.00E-04	1.37E+05	2.05E+06	1.00E-04
1.50E-05	760	2.42E-12	3.44E+08	1.50E+01	2.21E-06	6.20E+06	1.00E-03	1.37E+04	2.05E+05	1.00E-03
1.50E-05	760	2.42E-12	3.44E+08	1.50E+01	2.21E-06	6.20E+06	1.00E-02	1.37E+03	2.05E+04	1.00E-02
1.50E-05	760	2.42E-12	3.44E+08	1.50E+01	2.21E-06	6.20E+06	1.00E-01	1.37E+02	2.05E+03	1.00E-01
1.50E-05	760	2.42E-12	3.44E+08	1.50E+01	2.21E-06	6.20E+06	1.00E+00	1.37E+01	2.05E+02	1.00E+00

Table A.B.3 presents the entire simulation space for helium that created the large data set for ionization coefficient with nondimensional constants.

Table A.B.3: Parameter space used to create argon simulations and nondimensional constants.

Gap (m)	Pressure (Torr)	L (m)	Pstar (Torr)	Vstar (V)	Pb	db	Pb*db/Vb	Vb	V (Volts)	pb/Eb
2.50E-07	76	1.83E-12	1.82E+09	1.13E+01	4.17E-08	1.37E+05	1.00E-04	5.70E+01	6.46E+02	1.00E-04
2.50E-07	76	1.83E-12	1.82E+09	1.13E+01	4.17E-08	1.37E+05	1.00E-03	5.70E+00	6.46E+01	1.00E-03
2.50E-07	76	1.83E-12	1.82E+09	1.13E+01	4.17E-08	1.37E+05	1.00E-02	5.70E-01	6.46E+00	1.00E-02
2.50E-07	76	1.83E-12	1.82E+09	1.13E+01	4.17E-08	1.37E+05	1.00E-01	5.70E-02	6.46E-01	1.00E-01
2.50E-07	76	1.83E-12	1.82E+09	1.13E+01	4.17E-08	1.37E+05	1.00E+00	5.70E-03	6.46E-02	1.00E+00
2.50E-07	190	1.83E-12	1.82E+09	1.13E+01	1.04E-07	1.37E+05	1.00E-04	1.43E+02	1.62E+03	1.00E-04
2.50E-07	190	1.83E-12	1.82E+09	1.13E+01	1.04E-07	1.37E+05	1.00E-03	1.43E+01	1.62E+02	1.00E-03
2.50E-07	190	1.83E-12	1.82E+09	1.13E+01	1.04E-07	1.37E+05	1.00E-02	1.43E+00	1.62E+01	1.00E-02
2.50E-07	190	1.83E-12	1.82E+09	1.13E+01	1.04E-07	1.37E+05	1.00E-01	1.43E-01	1.62E+00	1.00E-01
2.50E-07	190	1.83E-12	1.82E+09	1.13E+01	1.04E-07	1.37E+05	1.00E+00	1.43E-02	1.62E-01	1.00E+00
2.50E-07	380	1.83E-12	1.82E+09	1.13E+01	2.08E-07	1.37E+05	1.00E-04	2.85E+02	3.23E+03	1.00E-04
2.50E-07	380	1.83E-12	1.82E+09	1.13E+01	2.08E-07	1.37E+05	1.00E-03	2.85E+01	3.23E+02	1.00E-03
2.50E-07	380	1.83E-12	1.82E+09	1.13E+01	2.08E-07	1.37E+05	1.00E-02	2.85E+00	3.23E+01	1.00E-02
2.50E-07	380	1.83E-12	1.82E+09	1.13E+01	2.08E-07	1.37E+05	1.00E-01	2.85E-01	3.23E+00	1.00E-01
2.50E-07	380	1.83E-12	1.82E+09	1.13E+01	2.08E-07	1.37E+05	1.00E+00	2.85E-02	3.23E-01	1.00E+00
2.50E-07	760	1.83E-12	1.82E+09	1.13E+01	4.17E-07	1.37E+05	1.00E-04	5.70E+02	6.46E+03	1.00E-04
2.50E-07	760	1.83E-12	1.82E+09	1.13E+01	4.17E-07	1.37E+05	1.00E-03	5.70E+01	6.46E+02	1.00E-03
2.50E-07	760	1.83E-12	1.82E+09	1.13E+01	4.17E-07	1.37E+05	1.00E-02	5.70E+00	6.46E+01	1.00E-02
2.50E-07	760	1.83E-12	1.82E+09	1.13E+01	4.17E-07	1.37E+05	1.00E-01	5.70E-01	6.46E+00	1.00E-01
2.50E-07	760	1.83E-12	1.82E+09	1.13E+01	4.17E-07	1.37E+05	1.00E+00	5.70E-02	6.46E-01	1.00E+00
5.00E-07	76	1.83E-12	1.82E+09	1.13E+01	4.17E-08	2.74E+05	1.00E-04	1.14E+02	1.29E+03	1.00E-04
5.00E-07	76	1.83E-12	1.82E+09	1.13E+01	4.17E-08	2.74E+05	1.00E-03	1.14E+01	1.29E+02	1.00E-03
5.00E-07	76	1.83E-12	1.82E+09	1.13E+01	4.17E-08	2.74E+05	1.00E-02	1.14E+00	1.29E+01	1.00E-02
5.00E-07	76	1.83E-12	1.82E+09	1.13E+01	4.17E-08	2.74E+05	1.00E-01	1.14E-01	1.29E+00	1.00E-01
5.00E-07	76	1.83E-12	1.82E+09	1.13E+01	4.17E-08	2.74E+05	1.00E+00	1.14E-02	1.29E-01	1.00E+00
5.00E-07	190	1.83E-12	1.82E+09	1.13E+01	1.04E-07	2.74E+05	1.00E-04	2.85E+02	3.23E+03	1.00E-04
5.00E-07	190	1.83E-12	1.82E+09	1.13E+01	1.04E-07	2.74E+05	1.00E-03	2.85E+01	3.23E+02	1.00E-03
5.00E-07	190	1.83E-12	1.82E+09	1.13E+01	1.04E-07	2.74E+05	1.00E-02	2.85E+00	3.23E+01	1.00E-02
5.00E-07	190	1.83E-12	1.82E+09	1.13E+01	1.04E-07	2.74E+05	1.00E-01	2.85E-01	3.23E+00	1.00E-01
5.00E-07	190	1.83E-12	1.82E+09	1.13E+01	1.04E-07	2.74E+05	1.00E+00	2.85E-02	3.23E-01	1.00E+00
5.00E-07	380	1.83E-12	1.82E+09	1.13E+01	2.08E-07	2.74E+05	1.00E-04	5.70E+02	6.46E+03	1.00E-04
5.00E-07	380	1.83E-12	1.82E+09	1.13E+01	2.08E-07	2.74E+05	1.00E-03	5.70E+01	6.46E+02	1.00E-03
5.00E-07	380	1.83E-12	1.82E+09	1.13E+01	2.08E-07	2.74E+05	1.00E-02	5.70E+00	6.46E+01	1.00E-02
5.00E-07	380	1.83E-12	1.82E+09	1.13E+01	2.08E-07	2.74E+05	1.00E-01	5.70E-01	6.46E+00	1.00E-01
5.00E-07	380	1.83E-12	1.82E+09	1.13E+01	2.08E-07	2.74E+05	1.00E+00	5.70E-02	6.46E-01	1.00E+00
5.00E-07	760	1.83E-12	1.82E+09	1.13E+01	4.17E-07	2.74E+05	1.00E-04	1.14E+03	1.29E+04	1.00E-04
5.00E-07	760	1.83E-12	1.82E+09	1.13E+01	4.17E-07	2.74E+05	1.00E-03	1.14E+02	1.29E+03	1.00E-03
5.00E-07	760	1.83E-12	1.82E+09	1.13E+01	4.17E-07	2.74E+05	1.00E-02	1.14E+01	1.29E+02	1.00E-02
5.00E-07	760	1.83E-12	1.82E+09	1.13E+01	4.17E-07	2.74E+05	1.00E-01	1.14E+00	1.29E+01	1.00E-01
5.00E-07	760	1.83E-12	1.82E+09	1.13E+01	4.17E-07	2.74E+05	1.00E+00	1.14E-01	1.29E+00	1.00E+00
1.00E-06	76	1.83E-12	1.82E+09	1.13E+01	4.17E-08	5.47E+05	1.00E-04	2.28E+02	2.58E+03	1.00E-04
1.00E-06	76	1.83E-12	1.82E+09	1.13E+01	4.17E-08	5.47E+05	1.00E-03	2.28E+01	2.58E+02	1.00E-03
1.00E-06	76	1.83E-12	1.82E+09	1.13E+01	4.17E-08	5.47E+05	1.00E-02	2.28E+00	2.58E+01	1.00E-02
1.00E-06	76	1.83E-12	1.82E+09	1.13E+01	4.17E-08	5.47E+05	1.00E-01	2.28E-01	2.58E+00	1.00E-01
1.00E-06	76	1.83E-12	1.82E+09	1.13E+01	4.17E-08	5.47E+05	1.00E+00	2.28E-02	2.58E-01	1.00E+00
1.00E-06	190	1.83E-12	1.82E+09	1.13E+01	1.04E-07	5.47E+05	1.00E-04	5.70E+02	6.46E+03	1.00E-04
1.00E-06	190	1.83E-12	1.82E+09	1.13E+01	1.04E-07	5.47E+05	1.00E-03	5.70E+01	6.46E+02	1.00E-03
1.00E-06	190	1.83E-12	1.82E+09	1.13E+01	1.04E-07	5.47E+05	1.00E-02	5.70E+00	6.46E+01	1.00E-02
1.00E-06	190	1.83E-12	1.82E+09	1.13E+01	1.04E-07	5.47E+05	1.00E-01	5.70E-01	6.46E+00	1.00E-01
1.00E-06	190	1.83E-12	1.82E+09	1.13E+01	1.04E-07	5.47E+05	1.00E+00	5.70E-02	6.46E-01	1.00E+00

Table A.B.2 Continued.

Gap (m)	Pressure (Torr)	L (m)	Pstar (Torr)	Vstar (V)	Pb	db	Pb*db/Vb	Vb	V (Volts)	pb/Eb
1.00E-06	380	1.83E-12	1.82E+09	1.13E+01	2.08E-07	5.47E+05	1.00E-04	1.14E+03	1.29E+04	1.00E-04
1.00E-06	380	1.83E-12	1.82E+09	1.13E+01	2.08E-07	5.47E+05	1.00E-03	1.14E+02	1.29E+03	1.00E-03
1.00E-06	380	1.83E-12	1.82E+09	1.13E+01	2.08E-07	5.47E+05	1.00E-02	1.14E+01	1.29E+02	1.00E-02
1.00E-06	380	1.83E-12	1.82E+09	1.13E+01	2.08E-07	5.47E+05	1.00E-01	1.14E+00	1.29E+01	1.00E-01
1.00E-06	380	1.83E-12	1.82E+09	1.13E+01	2.08E-07	5.47E+05	1.00E+00	1.14E-01	1.29E+00	1.00E+00
1.00E-06	760	1.83E-12	1.82E+09	1.13E+01	4.17E-07	5.47E+05	1.00E-04	2.28E+03	2.58E+04	1.00E-04
1.00E-06	760	1.83E-12	1.82E+09	1.13E+01	4.17E-07	5.47E+05	1.00E-03	2.28E+02	2.58E+03	1.00E-03
1.00E-06	760	1.83E-12	1.82E+09	1.13E+01	4.17E-07	5.47E+05	1.00E-02	2.28E+01	2.58E+02	1.00E-02
1.00E-06	760	1.83E-12	1.82E+09	1.13E+01	4.17E-07	5.47E+05	1.00E-01	2.28E+00	2.58E+01	1.00E-01
1.00E-06	760	1.83E-12	1.82E+09	1.13E+01	4.17E-07	5.47E+05	1.00E+00	2.28E-01	2.58E+00	1.00E+00
5.00E-06	76	1.83E-12	1.82E+09	1.13E+01	4.17E-08	2.74E+06	1.00E-04	1.14E+03	1.29E+04	1.00E-04
5.00E-06	76	1.83E-12	1.82E+09	1.13E+01	4.17E-08	2.74E+06	1.00E-03	1.14E+02	1.29E+03	1.00E-03
5.00E-06	76	1.83E-12	1.82E+09	1.13E+01	4.17E-08	2.74E+06	1.00E-02	1.14E+01	1.29E+02	1.00E-02
5.00E-06	76	1.83E-12	1.82E+09	1.13E+01	4.17E-08	2.74E+06	1.00E-01	1.14E+00	1.29E+01	1.00E-01
5.00E-06	76	1.83E-12	1.82E+09	1.13E+01	4.17E-08	2.74E+06	1.00E+00	1.14E-01	1.29E+00	1.00E+00
5.00E-06	190	1.83E-12	1.82E+09	1.13E+01	1.04E-07	2.74E+06	1.00E-04	2.85E+03	3.23E+04	1.00E-04
5.00E-06	190	1.83E-12	1.82E+09	1.13E+01	1.04E-07	2.74E+06	1.00E-03	2.85E+02	3.23E+03	1.00E-03
5.00E-06	190	1.83E-12	1.82E+09	1.13E+01	1.04E-07	2.74E+06	1.00E-02	2.85E+01	3.23E+02	1.00E-02
5.00E-06	190	1.83E-12	1.82E+09	1.13E+01	1.04E-07	2.74E+06	1.00E-01	2.85E+00	3.23E+01	1.00E-01
5.00E-06	190	1.83E-12	1.82E+09	1.13E+01	1.04E-07	2.74E+06	1.00E+00	2.85E-01	3.23E+00	1.00E+00
5.00E-06	380	1.83E-12	1.82E+09	1.13E+01	2.08E-07	2.74E+06	1.00E-04	5.70E+03	6.46E+04	1.00E-04
5.00E-06	380	1.83E-12	1.82E+09	1.13E+01	2.08E-07	2.74E+06	1.00E-03	5.70E+02	6.46E+03	1.00E-03
5.00E-06	380	1.83E-12	1.82E+09	1.13E+01	2.08E-07	2.74E+06	1.00E-02	5.70E+01	6.46E+02	1.00E-02
5.00E-06	380	1.83E-12	1.82E+09	1.13E+01	2.08E-07	2.74E+06	1.00E-01	5.70E+00	6.46E+01	1.00E-01
5.00E-06	380	1.83E-12	1.82E+09	1.13E+01	2.08E-07	2.74E+06	1.00E+00	5.70E-01	6.46E+00	1.00E+00
5.00E-06	760	1.83E-12	1.82E+09	1.13E+01	4.17E-07	2.74E+06	1.00E-04	1.14E+04	1.29E+05	1.00E-04
5.00E-06	760	1.83E-12	1.82E+09	1.13E+01	4.17E-07	2.74E+06	1.00E-03	1.14E+03	1.29E+04	1.00E-03
5.00E-06	760	1.83E-12	1.82E+09	1.13E+01	4.17E-07	2.74E+06	1.00E-02	1.14E+02	1.29E+03	1.00E-02
5.00E-06	760	1.83E-12	1.82E+09	1.13E+01	4.17E-07	2.74E+06	1.00E-01	1.14E+01	1.29E+02	1.00E-01
5.00E-06	760	1.83E-12	1.82E+09	1.13E+01	4.17E-07	2.74E+06	1.00E+00	1.14E+00	1.29E+01	1.00E+00
1.50E-05	76	1.83E-12	1.82E+09	1.13E+01	4.17E-08	8.21E+06	1.00E-04	3.42E+03	3.88E+04	1.00E-04
1.50E-05	76	1.83E-12	1.82E+09	1.13E+01	4.17E-08	8.21E+06	1.00E-03	3.42E+02	3.88E+03	1.00E-03
1.50E-05	76	1.83E-12	1.82E+09	1.13E+01	4.17E-08	8.21E+06	1.00E-02	3.42E+01	3.88E+02	1.00E-02
1.50E-05	76	1.83E-12	1.82E+09	1.13E+01	4.17E-08	8.21E+06	1.00E-01	3.42E+00	3.88E+01	1.00E-01
1.50E-05	76	1.83E-12	1.82E+09	1.13E+01	4.17E-08	8.21E+06	1.00E+00	3.42E-01	3.88E+00	1.00E+00
1.50E-05	190	1.83E-12	1.82E+09	1.13E+01	1.04E-07	8.21E+06	1.00E-04	8.55E+03	9.69E+04	1.00E-04
1.50E-05	190	1.83E-12	1.82E+09	1.13E+01	1.04E-07	8.21E+06	1.00E-03	8.55E+02	9.69E+03	1.00E-03
1.50E-05	190	1.83E-12	1.82E+09	1.13E+01	1.04E-07	8.21E+06	1.00E-02	8.55E+01	9.69E+02	1.00E-02
1.50E-05	190	1.83E-12	1.82E+09	1.13E+01	1.04E-07	8.21E+06	1.00E-01	8.55E+00	9.69E+01	1.00E-01
1.50E-05	190	1.83E-12	1.82E+09	1.13E+01	1.04E-07	8.21E+06	1.00E+00	8.55E-01	9.69E+00	1.00E+00
1.50E-05	380	1.83E-12	1.82E+09	1.13E+01	2.08E-07	8.21E+06	1.00E-04	1.71E+04	1.94E+05	1.00E-04
1.50E-05	380	1.83E-12	1.82E+09	1.13E+01	2.08E-07	8.21E+06	1.00E-03	1.71E+03	1.94E+04	1.00E-03
1.50E-05	380	1.83E-12	1.82E+09	1.13E+01	2.08E-07	8.21E+06	1.00E-02	1.71E+02	1.94E+03	1.00E-02
1.50E-05	380	1.83E-12	1.82E+09	1.13E+01	2.08E-07	8.21E+06	1.00E-01	1.71E+01	1.94E+02	1.00E-01
1.50E-05	380	1.83E-12	1.82E+09	1.13E+01	2.08E-07	8.21E+06	1.00E+00	1.71E+00	1.94E+01	1.00E+00
1.50E-05	760	1.83E-12	1.82E+09	1.13E+01	4.17E-07	8.21E+06	1.00E-04	3.42E+04	3.88E+05	1.00E-04
1.50E-05	760	1.83E-12	1.82E+09	1.13E+01	4.17E-07	8.21E+06	1.00E-03	3.42E+03	3.88E+04	1.00E-03
1.50E-05	760	1.83E-12	1.82E+09	1.13E+01	4.17E-07	8.21E+06	1.00E-02	3.42E+02	3.88E+03	1.00E-02
1.50E-05	760	1.83E-12	1.82E+09	1.13E+01	4.17E-07	8.21E+06	1.00E-01	3.42E+01	3.88E+02	1.00E-01
1.50E-05	760	1.83E-12	1.82E+09	1.13E+01	4.17E-07	8.21E+06	1.00E+00	3.42E+00	3.88E+01	1.00E+00

APPENDIX C. PIC/MCC SIMULATION SAMPLE CODES

The following is an example of the shell scripts and XPDP1 input decks used to run the test cases described in Appendix 2.

```

C:\Users\russell\Google Drive\PhD Dissertation\chapters\appendices\new 1.txt
Thursday, June 25, 2020 11:57 AM
#!/bin/bash
#This script shows an example of the input deck used as well as the code that generates it for
each case as shown in the previous tables

declare -a volt
declare -a press
declare -a gap

volt=(3.42E+03 3.42E+02 3.42E+01 3.42E+00 3.42E-01 8.56E+03 8.56E+02
8.56E+01
8.56E+00 8.56E-01 1.71E+04 1.71E+03 1.71E+02 1.71E+01 1.71E+00 3.42E+04
3.42E+03 3.42E+02 3.42E+01 3.42E+00 6.85E+03 6.85E+02 6.85E+01 6.85E+00
6.85E-01 1.71E+04 1.71E+03 1.71E+02 1.71E+01 1.71E+00 3.42E+04 3.42E+03
3.42E+02 3.42E+01 3.42E+00 6.85E+04 6.85E+03 6.85E+02 6.85E+01 6.85E+00
1.37E+04 1.37E+03 1.37E+02 1.37E+01 1.37E+00 3.42E+04 3.42E+03 3.42E+02
3.42E+01 3.42E+00 6.85E+04 6.85E+03 6.85E+02 6.85E+01 6.85E+00 1.37E+05
1.37E+04 1.37E+03 1.37E+02 1.37E+01 6.85E+04 6.85E+03 6.85E+02 6.85E+01
6.85E+00 1.71E+05 1.71E+04 1.71E+03 1.71E+02 1.71E+01 3.42E+05 3.42E+04
3.42E+03 3.42E+02 3.42E+01 6.85E+05 6.85E+04 6.85E+03 6.85E+02 6.85E+01
2.05E+05 2.05E+04 2.05E+03 2.05E+02 2.05E+01 5.14E+05 5.14E+04 5.14E+03
5.14E+02 5.14E+01 1.03E+06 1.03E+05 1.03E+04 1.03E+03 1.03E+02 2.05E+06
2.05E+05 2.05E+04 2.05E+03 2.05E+02)

press=(76 76 76 76 76 190 190 190 190 190 380 380 380 380 380 760 760 760 760 76 76
76 76 190 190 190 190 190 380 380 380 380 380 760 760 760 76 76 76 76 76 190
190 190 190 380 380 380 380 380 760 760 760 760 760 76 76 76 76 190 190 190 190
380 380 380 380 380 760 760 760 760 76 76 76 76 190 190 190 190 380 380 380
380 760 760 760 760 760)

gap=(2.50E-07 2.50E-07 2.50E-07 2.50E-07 2.50E-07 2.50E-07 2.50E-07 2.50E-07
2.50E-07 2.50E-07 2.50E-07 2.50E-07 2.50E-07 2.50E-07 2.50E-07 2.50E-07
2.50E-07 2.50E-07 2.50E-07 5.00E-07 5.00E-07 5.00E-07 5.00E-07 5.00E-07
5.00E-07 5.00E-07 5.00E-07 5.00E-07 5.00E-07 5.00E-07 5.00E-07 5.00E-07
1.00E-06 1.00E-06 1.00E-06 1.00E-06 1.00E-06 1.00E-06 1.00E-06 1.00E-06
1.00E-06 1.00E-06 1.00E-06 1.00E-06 1.00E-06 1.00E-06 1.00E-06 1.00E-06
1.00E-06 1.00E-06 1.00E-06 5.00E-06 5.00E-06 5.00E-06 5.00E-06 5.00E-06
5.00E-06 5.00E-06 5.00E-06 5.00E-06 5.00E-06 5.00E-06 5.00E-06 5.00E-06
1.50E-05 1.50E-05 1.50E-05 1.50E-05 1.50E-05 1.50E-05 1.50E-05 1.50E-05
1.50E-05 1.50E-05 1.50E-05 1.50E-05 1.50E-05 1.50E-05 1.50E-05 1.50E-05
1.50E-05 1.50E-05 1.50E-05 1.50E-05)

arraylength=${#volt[@]}

for (( i=1; i<${arraylength}+1; i++ ))
do
    mkdir /home/helios/a/mlovele/Documents/russ_pdp1/alpha/argon_2/$i
done

for (( d=1; d<${arraylength}+1; d++ ))
do
    echo "RF DISCHARGE(IN MKS UNITS)

```

```

--v0y[m/s]---vty[m/s]---vyloader---v0z[m/s]---vtz[m/s]---vzloader--
    0.0          1.4e4          0          0.0          1.4e4          0

--nbin----Emin[eV]----Emax[ev]---max-np--
    150          0.0          200.0          20000000

-For-Mid-Diagnostic---nbin----Emin[eV]---Emax[ev]----XStart--XFinish--
                                100          0.0          10.0          .020          .030

-For-vel_dist---vx_lower--vx_upper--nxbin--vy_lower--vy_upper--nybin--vz_lower--vz_upper--nzbin-
                    -1.5e6  1.5e6          0          -1.5e6  1.5e6          0          -1.5e6  1.5e6          0

" >> /home/helios/a/mlovele/Documents/russ_pdp1/alpha/argon_2/$d/argon_$d.inp
done

# create job script for job scheduler on machine

for d in {1..100};
do
echo "
#!/bin/bash
#PBS -k o
#PBS -l nodes=1:ppn=1,walltime=12:00:00
#PBS -M rbrayfie@purdue.edu
#PBS -m abe
#PBS -N test
#PBS -j oe
cd /home/helios/a/mlovele/Documents/russ_pdp1/alpha/argon_2/"$d"
/home/helios/a/mlovele/Documents/XPDP1_files/XPDP1-130422/xpdp1.linux -nox -i argon_"$d".inp
-s 50000
" >> /home/helios/a/mlovele/Documents/russ_pdp1/alpha/argon_2/$d/job_$d.script
done

# Submit jobs to scheduler

for i in {1..100}; do
cd /home/helios/a/mlovele/Documents/russ_pdp1/alpha/argon_2/$i
qsub job_$i.script
done

```

Voltage-driven with electron-neutral collisions (argon)

```

-nsp---nc---nc2p---dt[s]---length[m]--area[m^2]--epsilon---B[Tesla]---PSI[D]--
  2   100 5e5  2E-14 " ${gap[$d-1]} " 1.0   1.0   0.0   0.0

-rhoback[C/m^3]---backj[Amp/m^2]---dde--extR[Ohm]--extL[H]---extC[F]---q0[C]-
  0.0   0   0.0   0.0   0.0   1.0   0.0

-dcramped--source--dc[V|Amp]--ramp[(V|Amp)/s]---ac[V|Amp]---f0[Hz]--theta0[D]-
  0     V   "${volt[$d-1]}" 0.0   0.0   0.0   0.0

--secondary---e_collisional---i_collisional---reflux---nfft--n_ave--nsmoothing--ntimestep--
  0     1     2     0     0  25000  6     0

--seec(electrons)---seec(ions)---ion species----Gpressure[Torr]---GTemp[eV]---imp--metal_conc
  0.0   0.0   2     "${press[$d-1]}" .026  0     0.0

--field_emission(0 or 1)---beta_fe---phi_fe
  0     55.0  5.1

---GAS---psource--nstrt--vol_source--begin_pt--end_pt--ionization_energy
  2     0     0     0     0     0.03  0

SPECIES 1

----q[C]-----m[Kg]---j0L[Amp/m^2]---j0R[Amp/m^2]----initn[m^-3]----k---
-1.602e-19  9.11e-31  0     1000     1e15  1

--vx0L[m/s]---vxtL[m/s]--vxcL[m/s]---vxLloader(0=RNDM,1=QS)--
  0.0   4.19e5  0.0   1

--vx0R[m/s]---vxtR[m/s]--vxcR[m/s]---vxRloader
  0.0   4.19e5  0     1

--v0y[m/s]---vty[m/s]---vyloader---v0z[m/s]---vtz[m/s]--vzloader--
  0.0   4.19e5  1     0.0   4.19e5  1

--nbin----Emin[eV]----Emax[eV]---max-np--
  150   0.0   50.0  15000000

-For-Mid-Diagnostic---nbin----Emin[eV]---Emax[eV]----XStart--XFinish--
  100   0.0   15.0  .020  .030

-For-vel_dist---vx_lower--vx_upper--nxbin--vy_lower--vy_upper--nybin--vz_lower--vz_upper--nzbin-
  -1.5e6  1.5e6  0     -1.5e6  1.5e6  0     -1.5e6  1.5e6  0

SPECIES 2

----q[C] -----m[Kg]---j0L[Amp/m^2]---j0R[Amp/m^2]----initn[m^-3]----k---
  1.602e-19  6.634e-26  0     1000     1e15  1

--vx0L[m/s]---vxtL[m/s]--vxcL[m/s]---vxLloader(0=RNDM,1=QS)--
  0.0   1.4e4  0.   0

--vx0R[m/s]---vxtR[m/s]--vxcR[m/s]---vxRloader
  0.0   1.4e4  0     0

```

The following MATLAB code was used to process the argon simulation results to calculate the ionization coefficient and the nondimensional ionization coefficient.

Contents

- Import data from text file.
- Initialize variables.
- Read columns of data as text:
- Open the text file.
- Read columns of data according to the format.
- Close the text file.
- Convert the contents of columns containing numeric text to numbers.
- Exclude rows with non-numeric cells
- Allocate imported array to column variable names
- Clear temporary variables

```
clear all  
  
for g=1:100
```

Import data from text file.

Script for importing data from the following text file:

```
C:\Users\rbray\Desktop\helium\1\output_ave.plt
```

To extend the code to different selected data or a different text file, generate a function instead of a script.

```
% Auto-generated by MATLAB on 2020/05/11 12:20:58
```

Initialize variables.

```
vars=["X"  
"Time Ave n_e"  
"Time Ave n_i"  
"Time Ave Ux_e"  
"Time Ave Ux_i"  
"Time Ave Uy_e"  
"Time Ave Uy_i"  
"Time Ave Uz_e"  
"Time Ave Uz_i"  
"Time Ave Jx_e"  
"Time Ave Jx_i"  
"Time Ave Jy_e"  
"Time Ave Jy_i"  
"Time Ave Jz_e"  
"Time Ave Jz_i"]
```

```

"Time Ave KEx_e"
"Time Ave KEx_i"
"Time Ave KEy_e"
"Time Ave KEy_i"
"Time Ave KEz_e"
"Time Ave KEz_i"
"Time Ave T_e"
"Time Ave T_i"
"Time Ave Tx_e"
"Time Ave Tx_i"
"Time Ave Ty_e"
"Time Ave Ty_i"
"Time Ave Tz_e"
"Time Ave Tz_i"
"Time Ave jdisp"];

```

```

fontsize=18;
labelfontsize=18;
legendFontSize=16;
markerSize=8;
markerSize2=11;
lineWidth=2;
lineWidth2=2;
markerWidth=1.1;
fontname='Times New Roman';
ticky=0.015;
tickx=0.015;

```

```

for t=1:30
imp_data(t).name=vars(t);
end

```

```

p=[76    76    76    76    76    190    190    190    190    190
   380    380    380    380    380    380    760    760    760    760
   760    76    76    76    76    76    76    190    190    190
   190    190    380    380    380    380    380    380    760    760
   760    760    760    76    76    76    76    76    76    190
   190    190    190    190    380    380    380    380    380    380
   760    760    760    760    760    76    76    76    76    76
   76    190    190    190    190    190    380    380    380    380
   380    380    760    760    760    760    760    76    76    76
   76    76    76    190    190    190    190    190    190    380
   380    380    380    380    760    760    760    760    760    760];
v=[3.42E+03    3.42E+02    3.42E+01    3.42E+00    3.42E-01 8.56E+03
   8.56E+02    8.56E+01    8.56E+00    8.56E-01 1.71E+04
   1.71E+03    1.71E+02    1.71E+01    1.71E+00    1.71E+00    3.42E+04

```


Close the text file.

```
fclose(fileID);
```

Convert the contents of columns containing numeric text to numbers.

Replace non-numeric text with NaN.

```
raw = repmat( {},length(dataArray{1}),length(dataArray)-1);
for col=1:length(dataArray)-1
    raw(1:length(dataArray{col}),col) = mat2cell(dataArray{col}, ones(length(dataArray{col}),
1));
end
numericData = NaN(size(dataArray{1},1),size(dataArray,2));

for col=[1,2,3,4,5,6,7,8,9,10,11,12,13,14,15,16,17,18,19,20,21,22,23,24,25,26,27,28,29,30]
    % Converts text in the input cell array to numbers. Replaced non-numeric
    % text with NaN.
    rawData = dataArray{col};
    for row=1:size(rawData, 1)
        % Create a regular expression to detect and remove non-numeric prefixes and
        % suffixes.
        regexstr = '(?<prefix>.*?)(?<numbers>([-]*\d+[\,]*)+[\.]{0,1}\d*[eEdD]{0,1}[-
+]*\d*[i]{0,1})|([-]*\d+[\,]*)*[\.]{1,1}\d+[eEdD]{0,1}[-+]*\d*[i]{0,1})(?<suffix>.*?);
        try
            result = regexp(rawData(row), regexstr, 'names');
            numbers = result.numbers;

            % Detected commas in non-thousand locations.
            invalidThousandsSeparator = false;
            if numbers.contains(',')
                thousandsRegExp = '^\\d+?(\\,\\d{3})*\\. {0,1}\\d*$';
                if isempty(regexp(numbers, thousandsRegExp, 'once'))
                    numbers = NaN;
                    invalidThousandsSeparator = true;
                end
            end
            % Convert numeric text to numbers.
            if ~invalidThousandsSeparator
                numbers = textscan(char(strep(numbers, ',', '')), '%f');
                numericData(row, col) = numbers{1};
                raw{row, col} = numbers{1};
            end
        catch
            raw{row, col} = rawData{row};
        end
    end
end
```

```
end
end
end
```

Exclude rows with non-numeric cells

```
I = ~all(cellfun(@(x) (isnumeric(x) || islogical(x)) && ~isnan(x),raw),2); % Find rows with non-
numeric cells
raw(I,:) = [];
```

Allocate imported array to column variable names

```
for t=1:30
    imp_data(t).data=cell2mat(raw(:,t));
end
```

```
J_x_e(g).data=imp_data(10).data;
gap(g).data=imp_data(1).data;
```

Clear temporary variables

```
clearvars imp_data filename delimiter formatSpec fileID dataArray ans raw col numericData
rowData row regexstr result numbers invalidThousandsSeparator thousandsRegExp I J K;
end
%Calculate alpha values
for g=1:100
alpha1(g).data=mean((diff(J_x_e(g).data)./(gap(g).data(2)-
gap(g).data(1)))./(diff(gap(g).data)./(gap(g).data(2)-gap(g).data(1))))/mean(J_x_e(g).data);
alpha2(g).data=mean((gradient(J_x_e(g).data,(gap(g).data(2)-
gap(g).data(1)))./gradient(gap(g).data,(gap(g).data(2)-gap(g).data(1))))./J_x_e(g).data);
alphatest(g).data=(1/(gap(g).data(101)))*log(J_x_e(g).data(101)/J_x_e(g).data(1));
end

%Removes values where simulation had no ionization
for h=1:100

    if alphatest(h).data>0
        alphatest(h).data=NaN;
    end

end

alpha3=zeros(1,100);

for h=1:100
```

```

alpha3(h)=alphatest(h).data;

end

%Nondimensional alpha calculation
alphabar=alpha3.*L;
%combined gaps

subplot(2,2,1)
plot(((p(41:45))./(v(41:45)./gap(41).data(end))).^(1),log(-(alpha3(41:45)./p(41:45))),'b-
o','LineWidth',lineWidth,'MarkerSize',markerSize)
hold on
plot(((p(61:65))./(v(61:65)./gap(61).data(end))).^(1),log(-(alpha3(61:65)./p(61:65))),'r-
x','LineWidth',lineWidth,'MarkerSize',markerSize)
hold on
plot(((p(81:85))./(v(81:85)./gap(81).data(end))).^(1),log(-(alpha3(81:85)./p(81:85))),'g-
*','LineWidth',lineWidth,'MarkerSize',markerSize)
title("76 Torr");
ylabel('ln(\alpha/P)[ln(1/Torr/m)]','Interpreter','tex')
xlabel(['p/E [Torr] \cdot m/V'],'Interpreter','tex')
ylim([0 8])
set(gca,'linewidth',lineWidth, 'TickDir', 'both', 'TickLength', [tickx,ticky], 'XMinorTick', 'off',
'YMinorTick', 'off', 'FontName', fontname, 'FontSize', fontsize, 'FontWeight', 'bold')
legend('1 micron','5 micron','15 micron');
grid on;
subplot(2,2,2)
plot(((p(46:50))./(v(46:50)./gap(41).data(end))).^(1),log(-(alpha3(46:50)./p(46:50))),'b-
o','LineWidth',lineWidth,'MarkerSize',markerSize)
hold on
plot(((p(66:70))./(v(66:70)./gap(61).data(end))).^(1),log(-(alpha3(66:70)./p(66:70))),'r-
x','LineWidth',lineWidth,'MarkerSize',markerSize)
hold on
plot(((p(86:90))./(v(86:90)./gap(81).data(end))).^(1),log(-(alpha3(86:90)./p(86:90))),'g-
*','LineWidth',lineWidth,'MarkerSize',markerSize)
title("190 Torr");
ylabel('ln(\alpha/P)[ln(1/Torr/m)]','Interpreter','tex')
xlabel(['p/E [Torr] \cdot m/V'],'Interpreter','tex')
ylim([0 8])
set(gca,'linewidth',lineWidth, 'TickDir', 'both', 'TickLength', [tickx,ticky], 'XMinorTick', 'off',
'YMinorTick', 'off', 'FontName', fontname, 'FontSize', fontsize, 'FontWeight', 'bold')
legend('1 micron','5 micron','15 micron');
grid on;
subplot(2,2,3)
plot(((p(51:55))./(v(51:55)./gap(41).data(end))).^(1),log(-(alpha3(51:55)./p(51:55))),'b-
o','LineWidth',lineWidth,'MarkerSize',markerSize)

```

```

hold on
plot(((p(71:75))./(v(71:75)./gap(61).data(end))).^(1),log(-(alpha3(71:75)./p(71:75))),'r-
x','LineWidth',lineWidth,'MarkerSize',markerSize)
hold on
plot(((p(91:95))./(v(91:95)./gap(81).data(end))).^(1),log(-(alpha3(91:95)./p(91:95))),'g-
*','LineWidth',lineWidth,'MarkerSize',markerSize)
title("380 Torr");
ylabel('ln(\alpha/P)[ln(1/Torr/m)]','Interpreter','tex')
xlabel(['p/E [Torr] \cdot m/V'],'Interpreter','tex')
ylim([0 8])
set(gca,'linewidth',lineWidth, 'TickDir', 'both', 'TickLength', [tickx,ticky],'XMinorTick', 'off',
'YMinorTick', 'off','FontName',fontname,'FontSize',fontsize,'FontWeight','bold')
legend('1 micron','5 micron','15 micron');
grid on;
subplot(2,2,4)
plot(((p(56:60))./(v(56:60)./gap(41).data(end))).^(1),log(-(alpha3(56:60)./p(56:60))),'b-
o','LineWidth',lineWidth,'MarkerSize',markerSize)
hold on
plot(((p(76:80))./(v(76:80)./gap(61).data(end))).^(1),log(-(alpha3(76:80)./p(76:80))),'r-
x','LineWidth',lineWidth,'MarkerSize',markerSize)
hold on
plot(((p(96:100))./(v(96:100)./gap(81).data(end))).^(1),log(-(alpha3(96:100)./p(96:100))),'g-
*','LineWidth',lineWidth,'MarkerSize',markerSize)
hold on
title("760 Torr");
ylabel('ln(\alpha/P)[ln(1/Torr/m)]','Interpreter','tex')
xlabel(['p/E [Torr] \cdot m/V'],'Interpreter','tex')
ylim([0 8])
set(gca,'linewidth',lineWidth, 'TickDir', 'both', 'TickLength', [tickx,ticky],'XMinorTick', 'off',
'YMinorTick', 'off','FontName',fontname,'FontSize',fontsize,'FontWeight','bold')
legend('1 micron','5 micron','15 micron');
grid on;

figure

subplot(2,2,1)
plot((PbarEbar(41:45)).^(1),log(-(alphabar(41:45)./Pbar(41:45))),'b-
o','LineWidth',lineWidth,'MarkerSize',markerSize)
hold on
plot((PbarEbar(61:65)).^(1),log(-(alphabar(61:65)./Pbar(61:65))),'r-
x','LineWidth',lineWidth,'MarkerSize',markerSize)
hold on
plot((PbarEbar(81:85)).^(1),log(-(alphabar(81:85)./Pbar(81:85))),'g-
*','LineWidth',lineWidth,'MarkerSize',markerSize)
title(['{\boldmath$\bar{p}}$' '\boldmath{= 2.12E-7}}' ],'Interpreter','latex');

```

```

ylabel(['\bf{ln}' '\{\boldmath$\bar{\alpha}$}' '\bf{/}' '\{\boldmath$\bar{p}$}' '\bf{)}'], 'Interpreter', 'latex', 'fontsize', fontsize, 'fontweight', 'bold')
xlabel(['\{\boldmath$\bar{p}$}' '\bf{/}' '\{\boldmath$\bar{E}$}' '\bf{)}'], 'Interpreter', 'latex', 'fontsize', fontsize, 'fontweight', 'bold')
ylim([-6 1])
set(gca, 'linewidth', lineWidth, 'TickDir', 'both', 'TickLength', [tickx, ticky], 'XMinorTick', 'off', 'YMinorTick', 'off', 'FontName', fontname, 'FontSize', fontsize, 'FontWeight', 'bold')
leg1=legend(['\{\boldmath$\bar{d}$}' '\bf{)}' = 5.47e5'], ['\{\boldmath$\bar{d}$}' '\bf{)}' = 2.74e6'], ['\{\boldmath$\bar{d}$}' '\bf{)}' = 8.21e6']);
set(leg1, 'Interpreter', 'latex');
grid on;
subplot(2,2,2)
plot((PbarEbar(46:50)).^(1), log(-(alphabar(46:50)./Pbar(46:50))), 'b-o', 'LineWidth', lineWidth, 'MarkerSize', markerSize)
hold on
plot((PbarEbar(66:70)).^(1), log(-(alphabar(66:70)./Pbar(66:70))), 'r-x', 'LineWidth', lineWidth, 'MarkerSize', markerSize)
hold on
plot((PbarEbar(86:90)).^(1), log(-(alphabar(86:90)./Pbar(86:90))), 'g-*', 'LineWidth', lineWidth, 'MarkerSize', markerSize)
title(['\{\boldmath$\bar{p}$}' '\bf{)}' '\{\boldmath{= 5.52E-7}' '\bf{)}' ], 'Interpreter', 'latex');
ylabel(['\bf{ln}' '\{\boldmath$\bar{\alpha}$}' '\bf{/}' '\{\boldmath$\bar{p}$}' '\bf{)}'], 'Interpreter', 'latex', 'fontsize', fontsize, 'fontweight', 'bold')
xlabel(['\{\boldmath$\bar{p}$}' '\bf{/}' '\{\boldmath$\bar{E}$}' '\bf{)}'], 'Interpreter', 'latex', 'fontsize', fontsize, 'fontweight', 'bold')
ylim([-6 1])
set(gca, 'linewidth', lineWidth, 'TickDir', 'both', 'TickLength', [tickx, ticky], 'XMinorTick', 'off', 'YMinorTick', 'off', 'FontName', fontname, 'FontSize', fontsize, 'FontWeight', 'bold')
leg1=legend(['\{\boldmath$\bar{d}$}' '\bf{)}' = 5.47e5'], ['\{\boldmath$\bar{d}$}' '\bf{)}' = 2.74e6'], ['\{\boldmath$\bar{d}$}' '\bf{)}' = 8.21e6']);
set(leg1, 'Interpreter', 'latex');
grid on;
subplot(2,2,3)
plot((PbarEbar(51:55)).^(1), log(-(alphabar(51:55)./Pbar(51:55))), 'b-o', 'LineWidth', lineWidth, 'MarkerSize', markerSize)
hold on
plot((PbarEbar(71:75)).^(1), log(-(alphabar(71:75)./Pbar(71:75))), 'r-x', 'LineWidth', lineWidth, 'MarkerSize', markerSize)
hold on
plot((PbarEbar(91:95)).^(1), log(-(alphabar(91:95)./Pbar(91:95))), 'g-*', 'LineWidth', lineWidth, 'MarkerSize', markerSize)
title(['\{\boldmath$\bar{p}$}' '\bf{)}' '\{\boldmath{= 1.1E-6}' '\bf{)}' ], 'Interpreter', 'latex');
ylabel(['\bf{ln}' '\{\boldmath$\bar{\alpha}$}' '\bf{/}' '\{\boldmath$\bar{p}$}' '\bf{)}'], 'Interpreter', 'latex', 'fontsize', fontsize, 'fontweight', 'bold')
xlabel(['\{\boldmath$\bar{p}$}' '\bf{/}' '\{\boldmath$\bar{E}$}' '\bf{)}'], 'Interpreter', 'latex', 'fontsize', fontsize, 'fontweight', 'bold')

```

```

ylim([-6 1])
set(gca,'linewidth',lineWidth, 'TickDir', 'both', 'TickLength', [tickx,ticky],'XMinorTick', 'off',
'YMinorTick', 'off','FontName',fontname,'FontSize',fontsize,'FontWeight','bold')
leg1=legend(['{\boldmath$\bar{d}$}' ' = 5.47e5'],[{\boldmath$\bar{d}$}' ' =
2.74e6'],[{\boldmath$\bar{d}$}' '= 8.21e6']);
set(leg1,'Interpreter','latex');
grid on;
subplot(2,2,4)
plot((PbarEbar(56:60)).^(1),log(-(alphabar(56:60)./Pbar(56:60))),'b-
o','LineWidth',lineWidth,'MarkerSize',markerSize)
hold on
plot((PbarEbar(76:80)).^(1),log(-(alphabar(76:80)./Pbar(76:80))),'r-
x','LineWidth',lineWidth,'MarkerSize',markerSize)
hold on
plot((PbarEbar(96:100)).^(1),log(-(alphabar(96:100)./Pbar(96:100))),'g-
*','LineWidth',lineWidth,'MarkerSize',markerSize)
hold on
title(['{\boldmath$\bar{p}$}' '\boldmath{= 2.21E-6}' ],'Interpreter','latex');
ylabel(['\bf{ln}' '\boldmath$\bar{\alpha}$}' '\bf{/}' '\boldmath$\bar{p}$}'
'\bf{)'}], 'Interpreter','latex','fontSize',fontSize,'fontWeight','bold')
xlabel(['{\boldmath$\bar{p}$}' '\bf{/}'
'\boldmath$\bar{E}$}'], 'Interpreter','latex','fontSize',fontSize,'fontWeight','bold')
ylim([-6 1])
set(gca,'linewidth',lineWidth, 'TickDir', 'both', 'TickLength', [tickx,ticky],'XMinorTick', 'off',
'YMinorTick', 'off','FontName',fontname,'FontSize',fontsize,'FontWeight','bold')
leg1=legend(['{\boldmath$\bar{d}$}' ' = 5.47e5'],[{\boldmath$\bar{d}$}' ' =
2.74e6'],[{\boldmath$\bar{d}$}' '= 8.21e6']);
set(leg1,'Interpreter','latex');
grid on;

```

The following MATLAB code was used to process the helium simulation results to calculate the ionization coefficient and the nondimensional ionization coefficient.

Contents

- Import data from text file.
- Initialize variables.
- Read columns of data as text:
- Open the text file.
- Read columns of data according to the format.
- Close the text file.
- Convert the contents of columns containing numeric text to numbers.
- Exclude rows with non-numeric cells
- Allocate imported array to column variable names
- Clear temporary variables

```
clear all  
  
for g=1:100
```

Import data from text file.

Script for importing data from the following text file:

```
C:\Users\rbray\Desktop\helium\1\output_ave.plt
```

To extend the code to different selected data or a different text file, generate a function instead of a script.

```
% Auto-generated by MATLAB on 2020/05/11 12:20:58
```

Initialize variables.

```
vars=["X"  
"Time Ave n_e"  
"Time Ave n_i"  
"Time Ave Ux_e"  
"Time Ave Ux_i"  
"Time Ave Uy_e"  
"Time Ave Uy_i"  
"Time Ave Uz_e"  
"Time Ave Uz_i"  
"Time Ave Jx_e"  
"Time Ave Jx_i"  
"Time Ave Jy_e"  
"Time Ave Jy_i"  
"Time Ave Jz_e"  
"Time Ave Jz_i"]
```

```

"Time Ave KEx_e"
"Time Ave KEx_i"
"Time Ave KEy_e"
"Time Ave KEy_i"
"Time Ave KEz_e"
"Time Ave KEz_i"
"Time Ave T_e"
"Time Ave T_i"
"Time Ave Tx_e"
"Time Ave Tx_i"
"Time Ave Ty_e"
"Time Ave Ty_i"
"Time Ave Tz_e"
"Time Ave Tz_i"
"Time Ave jdisp"];

```

```

fontSize=18;
labelfontSize=18;
legendFontSize=16;
markerSize=8;
markerSize2=11;
lineWidth=2;
lineWidth2=2;
markerWidth=1.1;
fontName='Times New Roman';
ticky=0.015;
tickx=0.015;

```

```

for t=1:30
imp_data(t).name=vars(t);
end

```

```

p=[76    76    76    76    76    190    190    190    190    190
   380    380    380    380    380    380    760    760    760    760
   760    76    76    76    76    76    76    190    190    190
   190    190    380    380    380    380    380    380    760    760
   760    760    760    76    76    76    76    76    76    190
   190    190    190    190    380    380    380    380    380    380
   760    760    760    760    760    76    76    76    76    76
   76    190    190    190    190    190    380    380    380    380
   380    380    760    760    760    760    760    76    76    76
   76    76    76    190    190    190    190    190    190    380
   380    380    380    380    760    760    760    760    760    760];
v=[6.46E+02    6.46E+01    6.46E+00    6.46E-01 6.46E-02 1.62E+03
   1.62E+02    1.62E+01    1.62E+00    1.62E-01 3.23E+03
   3.23E+02    3.23E+01    3.23E+00    3.23E-01 6.46E+03

```

6.46E+02	6.46E+01	6.46E+00	6.46E-01	1.29E+03				
1.29E+02	1.29E+01	1.29E+00	1.29E-01	3.23E+03				
3.23E+02	3.23E+01	3.23E+00	3.23E-01	6.46E+03				
6.46E+02	6.46E+01	6.46E+00	6.46E-01	1.29E+04				
1.29E+03	1.29E+02	1.29E+01	1.29E+00	2.58E+03				
2.58E+02	2.58E+01	2.58E+00	2.58E-01	6.46E+03				
6.46E+02	6.46E+01	6.46E+00	6.46E-01	1.29E+04				
1.29E+03	1.29E+02	1.29E+01	1.29E+00	2.58E+04				
2.58E+03	2.58E+02	2.58E+01	2.58E+00	1.29E+04				
1.29E+03	1.29E+02	1.29E+01	1.29E+00	3.23E+04				
3.23E+03	3.23E+02	3.23E+01	3.23E+00	6.46E+04				
6.46E+03	6.46E+02	6.46E+01	6.46E+00	1.29E+05				
1.29E+04	1.29E+03	1.29E+02	1.29E+01	3.88E+04				
3.88E+03	3.88E+02	3.88E+01	3.88E+00	9.69E+04				
9.69E+03	9.69E+02	9.69E+01	9.69E+00	1.94E+05				
1.94E+04	1.94E+03	1.94E+02	1.94E+01	3.88E+05				
3.88E+04	3.88E+03	3.88E+02	3.88E+01];					
PbarEbar=[1.00E-04	1.00E-03	1.00E-02	1.00E-01	1.00E+00	1.00E-04	1.00E-03		
1.00E-02	1.00E-01	1.00E+00	1.00E-04	1.00E-03	1.00E-02	1.00E-01	1.00E+00	
1.00E-04	1.00E-03	1.00E-02	1.00E-01	1.00E+00	1.00E-04	1.00E-03	1.00E-02	
1.00E-01	1.00E+00	1.00E-04	1.00E-03	1.00E-02	1.00E-01	1.00E+00		
1.00E-04	1.00E-03	1.00E-02	1.00E-01	1.00E+00	1.00E-04	1.00E-03	1.00E-02	
1.00E-01	1.00E+00	1.00E-04	1.00E-03	1.00E-02	1.00E-01	1.00E+00		
1.00E-04	1.00E-03	1.00E-02	1.00E-01	1.00E+00	1.00E-04	1.00E-03	1.00E-02	
1.00E-01	1.00E+00	1.00E-04	1.00E-03	1.00E-02	1.00E-01	1.00E+00		
1.00E-04	1.00E-03	1.00E-02	1.00E-01	1.00E+00	1.00E-04	1.00E-03	1.00E-02	
1.00E-01	1.00E+00	1.00E-04	1.00E-03	1.00E-02	1.00E-01	1.00E+00		
1.00E-04	1.00E-03	1.00E-02	1.00E-01	1.00E+00	1.00E-04	1.00E-03	1.00E-02	
1.00E-01	1.00E+00];							
Pbar=[4.17E-08	4.17E-08	4.17E-08	4.17E-08	4.17E-08	1.04E-07	1.04E-07	1.04E-07	1.04E-07
1.04E-07	2.08E-07	2.08E-07	2.08E-07	2.08E-07	2.08E-07	4.17E-07	4.17E-07	4.17E-07
4.17E-07	4.17E-07	4.17E-08	4.17E-08	4.17E-08	4.17E-08	4.17E-08	1.04E-07	1.04E-07
1.04E-07	1.04E-07	1.04E-07	2.08E-07	2.08E-07	2.08E-07	2.08E-07	2.08E-07	4.17E-07
4.17E-07	4.17E-07	4.17E-07	4.17E-07	4.17E-08	4.17E-08	4.17E-08	4.17E-08	4.17E-08
1.04E-07	1.04E-07	1.04E-07	1.04E-07	1.04E-07	2.08E-07	2.08E-07	2.08E-07	2.08E-07
2.08E-07	4.17E-07	4.17E-07	4.17E-07	4.17E-07	4.17E-07	4.17E-08	4.17E-08	4.17E-08
4.17E-08	4.17E-08	1.04E-07	1.04E-07	1.04E-07	1.04E-07	1.04E-07	2.08E-07	2.08E-07
2.08E-07	2.08E-07	2.08E-07	4.17E-07	4.17E-07	4.17E-07	4.17E-07	4.17E-07	4.17E-08
4.17E-08	4.17E-08	4.17E-08	4.17E-08	1.04E-07	1.04E-07	1.04E-07	1.04E-07	1.04E-07
2.08E-07	2.08E-07	2.08E-07	2.08E-07	2.08E-07	4.17E-07	4.17E-07	4.17E-07	4.17E-07
4.17E-07];								
dbar=[1.37E+05	1.37E+05	1.37E+05	1.37E+05	1.37E+05				
1.37E+05	1.37E+05	1.37E+05	1.37E+05	1.37E+05	1.37E+05	1.37E+05	1.37E+05	1.37E+05
1.37E+05	1.37E+05	1.37E+05	1.37E+05	1.37E+05	1.37E+05	1.37E+05	1.37E+05	1.37E+05

Close the text file.

```
fclose(fileID);
```

Convert the contents of columns containing numeric text to numbers.

Replace non-numeric text with NaN.

```
raw = repmat( {},length(dataArray{1}),length(dataArray)-1);
for col=1:length(dataArray)-1
    raw(1:length(dataArray{col}),col) = mat2cell(dataArray{col}, ones(length(dataArray{col}),
1));
end
numericData = NaN(size(dataArray{1},1),size(dataArray,2));

for col=[1,2,3,4,5,6,7,8,9,10,11,12,13,14,15,16,17,18,19,20,21,22,23,24,25,26,27,28,29,30]
    % Converts text in the input cell array to numbers. Replaced non-numeric
    % text with NaN.
    rawData = dataArray{col};
    for row=1:size(rawData, 1)
        % Create a regular expression to detect and remove non-numeric prefixes and
        % suffixes.
        regexstr = '(?<prefix>.*?)(?<numbers>([-]*\d+[\,]*)+[\.]{0,1}\d*[eEdD]{0,1}[-
+]*\d*[i]{0,1})|([-]*\d+[\,]*)*[\.]{1,1}\d+[eEdD]{0,1}[-+]*\d*[i]{0,1})(?<suffix>.*?);
        try
            result = regexp(rawData(row), regexstr, 'names');
            numbers = result.numbers;

            % Detected commas in non-thousand locations.
            invalidThousandsSeparator = false;
            if numbers.contains(',')
                thousandsRegExp = '^\\d+?(\\,\\d{3})*\\. {0,1}\\d*$';
                if isempty(regexp(numbers, thousandsRegExp, 'once'))
                    numbers = NaN;
                    invalidThousandsSeparator = true;
                end
            end
            % Convert numeric text to numbers.
            if ~invalidThousandsSeparator
                numbers = textscan(char(strep(numbers, ',', '')), '%f');
                numericData(row, col) = numbers{1};
                raw{row, col} = numbers{1};
            end
        catch
            raw{row, col} = rawData{row};
        end
    end
end
```

```
end
end
end
```

Exclude rows with non-numeric cells

```
I = ~all(cellfun(@(x) (isnumeric(x) || islogical(x)) && ~isnan(x),raw),2); % Find rows with non-
numeric cells
raw(I,:) = [];
```

Allocate imported array to column variable names

```
for t=1:30
    imp_data(t).data=cell2mat(raw(:,t));
end
```

```
J_x_e(g).data=imp_data(10).data;
gap(g).data=imp_data(1).data;
```

Clear temporary variables

```
clearvars imp_data filename delimiter formatSpec fileID dataArray ans raw col numericData
rowData row regexstr result numbers invalidThousandsSeparator thousandsRegExp I J K;
end
```

```
for g=1:100
alpha1(g).data=mean((diff(J_x_e(g).data)./(gap(g).data(2)-
gap(g).data(1)))./(diff(gap(g).data)./(gap(g).data(2)-gap(g).data(1))))/mean(J_x_e(g).data);
alpha2(g).data=mean((gradient(J_x_e(g).data,(gap(g).data(2)-
gap(g).data(1)))./gradient(gap(g).data,(gap(g).data(2)-gap(g).data(1))))./J_x_e(g).data);
alphatest(g).data=(1/(gap(g).data(101)))*log(J_x_e(g).data(101)/J_x_e(g).data(1));
end
```

```
%Calculate alpha values
```

```
for h=1:100
```

```
    if alphatest(h).data>0
        alphatest(h).data=NaN;
    end
```

```
end
```

```
alpha3=zeros(1,100);
```

```
%Remove values where simulation did not have ionization
```

```
for h=1:100
```

```
    alpha3(h)=alphatest(h).data;
```

```

end
alpha3(44)=NaN;

%Nondimensional alpha calculation
alphabar=alpha3.*L;

%%plots
%combined gaps

subplot(2,2,1)
plot(((p(41:45))./(v(41:45))./gap(41).data(end))).^(1),log(-(alpha3(41:45)./p(41:45))),'b-
o','LineWidth',lineWidth,'MarkerSize',markerSize)
hold on
plot(((p(61:65))./(v(61:65))./gap(61).data(end))).^(1),log(-(alpha3(61:65)./p(61:65))),'r-
x','LineWidth',lineWidth,'MarkerSize',markerSize)
hold on
plot(((p(81:85))./(v(81:85))./gap(81).data(end))).^(1),log(-(alpha3(81:85)./p(81:85))),'g-
*','LineWidth',lineWidth,'MarkerSize',markerSize)
title("76 Torr");
ylabel('ln(\alpha/P)[ln(1/Torr/m)]','Interpreter','tex')
xlabel(['p/E [Torr] \cdot m/V'],'Interpreter','tex')
ylim([2 6])
set(gca,'linewidth',lineWidth, 'TickDir', 'both', 'TickLength', [tickx,ticky],'XMinorTick', 'off',
'YMinorTick', 'off','FontName',fontname,'FontSize',fontsize,'FontWeight','bold')
legend('1 micron','5 micron','15 micron');
grid on;
subplot(2,2,2)
plot(((p(46:50))./(v(46:50))./gap(41).data(end))).^(1),log(-(alpha3(46:50)./p(46:50))),'b-
o','LineWidth',lineWidth,'MarkerSize',markerSize)
hold on
plot(((p(66:70))./(v(66:70))./gap(61).data(end))).^(1),log(-(alpha3(66:70)./p(66:70))),'r-
x','LineWidth',lineWidth,'MarkerSize',markerSize)
hold on
plot(((p(86:90))./(v(86:90))./gap(81).data(end))).^(1),log(-(alpha3(86:90)./p(86:90))),'g-
*','LineWidth',lineWidth,'MarkerSize',markerSize)
title("190 Torr");
ylabel('ln(\alpha/P)[ln(1/Torr/m)]','Interpreter','tex')
xlabel(['p/E [Torr] \cdot m/V'],'Interpreter','tex')
ylim([2 6])
set(gca,'linewidth',lineWidth, 'TickDir', 'both', 'TickLength', [tickx,ticky],'XMinorTick', 'off',
'YMinorTick', 'off','FontName',fontname,'FontSize',fontsize,'FontWeight','bold')
legend('1 micron','5 micron','15 micron');
grid on;

```

```

subplot(2,2,3)
plot(((p(51:55))./(v(51:55))./gap(41).data(end))).^(1),log(-(\alpha3(51:55)./p(51:55))),'b-
o','LineWidth',lineWidth,'MarkerSize',markerSize)
hold on
plot(((p(71:75))./(v(71:75))./gap(61).data(end))).^(1),log(-(\alpha3(71:75)./p(71:75))),'r-
x','LineWidth',lineWidth,'MarkerSize',markerSize)
hold on
plot(((p(91:95))./(v(91:95))./gap(81).data(end))).^(1),log(-(\alpha3(91:95)./p(91:95))),'g-
*','LineWidth',lineWidth,'MarkerSize',markerSize)
title("380 Torr");
ylabel('ln(\alpha/P)[ln(1/Torr/m)]','Interpreter','tex')
xlabel(['p/E [Torr] \cdot m/V'],'Interpreter','tex')
ylim([2 6])
set(gca,'linewidth',lineWidth, 'TickDir', 'both', 'TickLength', [tickx,ticky],'XMinorTick', 'off',
'YMinorTick', 'off','FontName',fontname,'FontSize',fontsize,'FontWeight','bold')
legend('1 micron','5 micron','15 micron');
grid on;
subplot(2,2,4)
plot(((p(56:60))./(v(56:60))./gap(41).data(end))).^(1),log(-(\alpha3(56:60)./p(56:60))),'b-
o','LineWidth',lineWidth,'MarkerSize',markerSize)
hold on
plot(((p(76:80))./(v(76:80))./gap(61).data(end))).^(1),log(-(\alpha3(76:80)./p(76:80))),'r-
x','LineWidth',lineWidth,'MarkerSize',markerSize)
hold on
plot(((p(96:100))./(v(96:100))./gap(81).data(end))).^(1),log(-(\alpha3(96:100)./p(96:100))),'g-
*','LineWidth',lineWidth,'MarkerSize',markerSize)
hold on
title("760 Torr");
ylabel('ln(\alpha/P)[ln(1/Torr/m)]','Interpreter','tex')
xlabel(['p/E [Torr] \cdot m/V'],'Interpreter','tex')
ylim([2 6])
set(gca,'linewidth',lineWidth, 'TickDir', 'both', 'TickLength', [tickx,ticky],'XMinorTick', 'off',
'YMinorTick', 'off','FontName',fontname,'FontSize',fontsize,'FontWeight','bold')
legend('1 micron','5 micron','15 micron');
grid on;

figure

subplot(2,2,1)
plot((PbarEbar(41:45)).^(1),log(-(\alphabar(41:45)./Pbar(41:45))),'b-
o','LineWidth',lineWidth,'MarkerSize',markerSize)
hold on
plot((PbarEbar(61:65)).^(1),log(-(\alphabar(61:65)./Pbar(61:65))),'r-
x','LineWidth',lineWidth,'MarkerSize',markerSize)
hold on

```

```

plot((PbarEbar(81:85)).^(1),log(-(alphabar(81:85)./Pbar(81:85))),'g-
*', 'LineWidth',lineWidth,'MarkerSize',markerSize)
title(['{\boldmath$\bar{p}$}' '\boldmath{= 4.17E-8}' ],'Interpreter','latex');
ylabel(['\bf{ln}' '\boldmath$\bar{\alpha}$' '\bf{/}' '\boldmath$\bar{p}$'
'\bf{)}'], 'Interpreter','latex','fontSize',fontSize,'fontweight','bold')
xlabel(['{\boldmath$\bar{p}$}' '\bf{/}'
'\boldmath$\bar{E}$' },'Interpreter','latex','fontSize',fontSize,'fontweight','bold')
ylim([-4 0])
set(gca,'linewidth',lineWidth, 'TickDir', 'both', 'TickLength', [tickx,ticky],'XMinorTick', 'off',
'YMinorTick', 'off','FontName',fontname,'FontSize',fontSize,'FontWeight','bold')
leg1=legend(['{\boldmath$\bar{d}$}' ' = 5.47e5'],['{\boldmath$\bar{d}$}' ' =
2.74e6'],['{\boldmath$\bar{d}$}' '= 8.21e6']);
set(leg1,'Interpreter','latex');
grid on;
subplot(2,2,2)
plot((PbarEbar(46:50)).^(1),log(-(alphabar(46:50)./Pbar(46:50))),'b-
o','LineWidth',lineWidth,'MarkerSize',markerSize)
hold on
plot((PbarEbar(66:70)).^(1),log(-(alphabar(66:70)./Pbar(66:70))),'r-
x','LineWidth',lineWidth,'MarkerSize',markerSize)
hold on
plot((PbarEbar(86:90)).^(1),log(-(alphabar(86:90)./Pbar(86:90))),'g-
*', 'LineWidth',lineWidth,'MarkerSize',markerSize)
title(['{\boldmath$\bar{p}$}' '\boldmath{= 1.04E-7}' ],'Interpreter','latex');
ylabel(['\bf{ln}' '\boldmath$\bar{\alpha}$' '\bf{/}' '\boldmath$\bar{p}$'
'\bf{)}'], 'Interpreter','latex','fontSize',fontSize,'fontweight','bold')
xlabel(['{\boldmath$\bar{p}$}' '\bf{/}'
'\boldmath$\bar{E}$' },'Interpreter','latex','fontSize',fontSize,'fontweight','bold')
ylim([-4 0])
set(gca,'linewidth',lineWidth, 'TickDir', 'both', 'TickLength', [tickx,ticky],'XMinorTick', 'off',
'YMinorTick', 'off','FontName',fontname,'FontSize',fontSize,'FontWeight','bold')
leg1=legend(['{\boldmath$\bar{d}$}' ' = 5.47e5'],['{\boldmath$\bar{d}$}' ' =
2.74e6'],['{\boldmath$\bar{d}$}' '= 8.21e6']);
set(leg1,'Interpreter','latex');
grid on;
subplot(2,2,3)
plot((PbarEbar(51:55)).^(1),log(-(alphabar(51:55)./Pbar(51:55))),'b-
o','LineWidth',lineWidth,'MarkerSize',markerSize)
hold on
plot((PbarEbar(71:75)).^(1),log(-(alphabar(71:75)./Pbar(71:75))),'r-
x','LineWidth',lineWidth,'MarkerSize',markerSize)
hold on
plot((PbarEbar(91:95)).^(1),log(-(alphabar(91:95)./Pbar(91:95))),'g-
*', 'LineWidth',lineWidth,'MarkerSize',markerSize)
title(['{\boldmath$\bar{p}$}' '\boldmath{= 2.08E-7}' ],'Interpreter','latex');

```

```

ylabel(['\bf{ln('      '\{\boldmath$\bar{\alpha}$}'      '\bf{/}'      '\{\boldmath$\bar{p}$}'
'\bf{)}'}], 'Interpreter', 'latex', 'fontsize', fontsize, 'fontweight', 'bold')
xlabel(['\{\boldmath$\bar{p}$}'      '\bf{/}'
'\{\boldmath$\bar{E}$}''], 'Interpreter', 'latex', 'fontsize', fontsize, 'fontweight', 'bold')
ylim([-4 0])
set(gca, 'linewidth', lineWidth, 'TickDir', 'both', 'TickLength', [tickx, ticky], 'XMinorTick', 'off',
'YMinorTick', 'off', 'FontName', fontname, 'FontSize', fontsize, 'FontWeight', 'bold')
leg1=legend(['\{\boldmath$\bar{d}$}'      ' = 5.47e5'], ['\{\boldmath$\bar{d}$}'      ' =
2.74e6'], ['\{\boldmath$\bar{d}$}'      '= 8.21e6']);
set(leg1, 'Interpreter', 'latex');
grid on;
subplot(2,2,4)
plot((PbarEbar(56:60)).^(1), log(-(alphabar(56:60)./Pbar(56:60))), 'b-
o', 'LineWidth', lineWidth, 'MarkerSize', markerSize)
hold on
plot((PbarEbar(76:80)).^(1), log(-(alphabar(76:80)./Pbar(76:80))), 'r-
x', 'LineWidth', lineWidth, 'MarkerSize', markerSize)
hold on
plot((PbarEbar(96:100)).^(1), log(-(alphabar(96:100)./Pbar(96:100))), 'g-
*', 'LineWidth', lineWidth, 'MarkerSize', markerSize)
hold on
title(['\{\boldmath$\bar{p}$}' '\{\boldmath{= 4.17E-7}' "], 'Interpreter', 'latex');
ylabel(['\bf{ln('      '\{\boldmath$\bar{\alpha}$}'      '\bf{/}'      '\{\boldmath$\bar{p}$}'
'\bf{)}'}], 'Interpreter', 'latex', 'fontsize', fontsize, 'fontweight', 'bold')
xlabel(['\{\boldmath$\bar{p}$}'      '\bf{/}'
'\{\boldmath$\bar{E}$}''], 'Interpreter', 'latex', 'fontsize', fontsize, 'fontweight', 'bold')
ylim([-4 0])
set(gca, 'linewidth', lineWidth, 'TickDir', 'both', 'TickLength', [tickx, ticky], 'XMinorTick', 'off',
'YMinorTick', 'off', 'FontName', fontname, 'FontSize', fontsize, 'FontWeight', 'bold')
leg1=legend(['\{\boldmath$\bar{d}$}'      ' = 5.47e5'], ['\{\boldmath$\bar{d}$}'      ' =
2.74e6'], ['\{\boldmath$\bar{d}$}'      '= 8.21e6']);
set(leg1, 'Interpreter', 'latex');
grid on;

```

REFERENCES

- ¹ K.H. Schoenbach, *Bioelectromagnetics* **39**, 257 (2018).
- ² K.H. Schoenbach and K. Becker, *Eur. Phys. J. D* **70**, 29 (2016).
- ³ R. Pothiraja, J. Lackmann, G. Keil, N. Bibinov, and P. Awakowicz, *Plasma for Bio-Decontamination, Medicine and Food Security* (Springer Netherlands, Dordrecht, 2012).
- ⁴ C.-C. Weng, J.-D. Liao, H.-H. Chen, T.-Y. Lin, and C.-L. Huang, *Int. J. Radiat. Biol.* **87**, 936 (2011).
- ⁵ P.P. Sedghizadeh, M.-T. Chen, C. Schaudinn, A. Gorur, and C. Jiang, *IEEE Trans. Plasma Sci.* **40**, 2879 (2012).
- ⁶ A. Shashurin and M. Keidar, *Phys. Plasmas* **22**, 122002 (2015).
- ⁷ H.J. Park, S.H. Kim, H.W. Ju, H. Lee, Y. Lee, S. Park, H. Yang, S.-J. Park, J.G. Eden, J. Yang, and C.H. Park, *Sci. Rep.* **8**, 2422 (2018).
- ⁸ M.G. Kong, G. Kroesen, G. Morfill, T. Nosenko, T. Shimizu, J. van Dijk, and J.L. Zimmermann, *New J. Phys.* **11**, 115012 (2009).
- ⁹ C.H. Park, J.S. Lee, J.H. Kim, D.-K. Kim, O.J. Lee, H.W. Ju, B.M. Moon, J.H. Cho, M.H. Kim, P.P. Sun, S.-J. Park, and J.G. Eden, *J. Phys. D: Appl. Phys.* **47**, 435402 (2014).
- ¹⁰ P.-L. Shao, J.-D. Liao, T.-W. Wong, Y.-C. Wang, S. Leu, and H.-K. Yip, *PLoS One* **11**, e0156699 (2016).
- ¹¹ X. Tan, S. Zhao, Q. Lei, X. Lu, G. He, and K. Ostrikov, *PLoS One* **9**, e101299 (2014).
- ¹² N. Recek, S. Andjelić, N. Hojnik, G. Filipič, S. Lazović, A. Vesel, G. Primc, M. Mozetič, M. Hawlina, G. Petrovski, and U. Cvelbar, *PLoS One* **11**, e0165883 (2016).
- ¹³ Z. Xiong, S. Zhao, X. Mao, X. Lu, G. He, G. Yang, M. Chen, M. Ishaq, and K. Ostrikov, *Stem Cell Res.* **12**, 387 (2014).
- ¹⁴ P. Norgard, S. Kovaleski, R.S. Brayfield, and A.L. Garner, *IEEE Trans. Plasma Sci.* **47**, 128 (2019).

- ¹⁵ I. V. Adamovich, I. Choi, N. Jiang, J.-H. Kim, S. Keshav, W.R. Lempert, E. Mintusov, M. Nishihara, M. Samimy, and M. Uddi, *Plasma Sources Sci. Technol.* **18**, 034018 (2009).
- ¹⁶ S.J. Beebe, P.M. Fox, L.J. Rec, K. Somers, R.H. Stark, and K.H. Schoenbach, *PPPS 2001 - Pulsed Power Plasma Sci. 2001* **1**, 211 (2002).
- ¹⁷ J. Deng, K.H. Schoenbach, E.S. Buescher, P.S. Hair, P.M. Fox, and S.J. Beebe, *Biophys. J.* **84**, 2709 (2003).
- ¹⁸ R. Nuccitelli, U. Pliquett, X. Chen, W. Ford, R. James Swanson, S.J. Beebe, J.F. Kolb, and K.H. Schoenbach, *Biochem. Biophys. Res. Commun.* **343**, 351 (2006).
- ¹⁹ R. Chen, N.M. Sain, K.T. Harlow, Y.-J. Chen, P.K. Shires, R. Heller, and S.J. Beebe, *Eur. J. Cancer* **50**, 2705 (2014).
- ²⁰ F. Xie, F. Varghese, A.G. Pakhomov, I. Semenov, S. Xiao, J. Philpott, and C. Zemlin, *PLoS One* **10**, e0144833 (2015).
- ²¹ J.F. Kolb, S. Kono, and K.H. Schoenbach, *Bioelectromagnetics* **27**, 172 (2006).
- ²² R. Bogue, *Sens. Rev.* **27**, 7 (2007).
- ²³ H.G. Craighead, in *Encycl. Nanotechnol.* (Springer Netherlands, Dordrecht, 2016), pp. 2356–2356.
- ²⁴ C. Wilson, *High Altitude Electromagnetic Pulse (HEMP) and High Power Microwave (HPM) Devices: Threat Assessments Clay Wilson Specialist in Technology and National Security Foreign Affairs, Defense, and Trade Division High Altitude Electromagnetic Pulse (HEMP) and Hi* (2008).
- ²⁵ M.D. Hogue, R.E. Cox, J. Mulligan, K. Ahmed, J.G. Wilson, and L.M. Calle, *J. Electrostat.* **91**, 21 (2018).
- ²⁶ A.M. Loveless and A.L. Garner, *Phys. Plasmas* **24**, 113522 (2017).
- ²⁷ Yuri P. Raizer, *Gas Discharge Physics* (Springer-Verlag Berlin Heidelberg, 1991).
- ²⁸ L.G.H. Huxley, R.W. Crompton, and M.T. Elford, *Br. J. Appl. Phys.* **17**, 1237 (1966).

- ²⁹ L.K. Warne, R.E. Jorgenson, and S.D. Nicolaysen, 95 (2003).
- ³⁰ F. Paschen, Ann. Phys. **273**, 69 (1889).
- ³¹ A.M. Loveless and A.L. Garner, Phys. Plasmas **24**, 104501 (2017).
- ³² A.L. Garner, A.M. Loveless, J.N. Dahal, and A. Venkattraman, IEEE Trans. Plasma Sci. **48**, 808 (2020).
- ³³ D.B. Go and A. Venkattraman, J. Phys. D. Appl. Phys. **47**, 503001 (2014).
- ³⁴ Z.L. Petrović, N. Škoro, D. Marić, C.M.O. Mahony, P.D. Maguire, M. Radmilović-Rađenović, and G. Malović, J. Phys. D. Appl. Phys. **41**, 194002 (2008).
- ³⁵ M. Radmilović-Radjenović and B. Radjenović, Plasma Sources Sci. Technol. **17**, 024005 (2008).
- ³⁶ Y. Fu, P. Zhang, and J.P. Verboncoeur, Appl. Phys. Lett. **112**, 254102 (2018).
- ³⁷ A. Venkattraman and A.A. Alexeenko, Phys. Plasmas **19**, 123515 (2012).
- ³⁸ A.M. Loveless and A.L. Garner, Appl. Phys. Lett. **108**, 234103 (2016).
- ³⁹ G. Meng, X. Gao, A.M. Loveless, C. Dong, D. Zhang, K. Wang, B. Zhu, Y. Cheng, and A.L. Garner, Phys. Plasmas **25**, 082116 (2018).
- ⁴⁰ A.M. Loveless, G. Meng, Q. Ying, F. Wu, K. Wang, Y. Cheng, and A.L. Garner, Sci. Rep. **9**, 5669 (2019).
- ⁴¹ S. Kovaleski, (2016).
- ⁴² University of Oregon, (n.d.).
- ⁴³ R.H. Fowler and L. Nordheim, Proc. R. Soc. A Math. Phys. Eng. Sci. **119**, 173 (1928).
- ⁴⁴ S.D. Dynako, A.M. Loveless, and A.L. Garner, Phys. Plasmas **25**, 103505 (2018).
- ⁴⁵ W. Li and D.Y. Li, J. Chem. Phys. **122**, 064708 (2005).
- ⁴⁶ B.M. Cox and W.T. Williams, J. Phys. D. Appl. Phys. **10**, L5 (1977).
- ⁴⁷ G.N. Fursey, IEEE Trans. Electr. Insul. **EI-20**, 659 (1985).
- ⁴⁸ D.W. Williams and W.T. Williams, J. Phys. D **7**, 1173 (1974).

- ⁴⁹ I. Langmuir, *Phys. Rev.* **2**, 450 (1913).
- ⁵⁰ C.D. Child, *Phys. Rev. (Series I)* **32**, 492 (1911).
- ⁵¹ S. Bhattacharjee and T. Chowdhury, *Appl. Phys. Lett.* **95**, 061501 (2009).
- ⁵² J.W. Luginsland, Y.Y. Lau, and R.M. Gilgenbach, *Phys. Rev. Lett.* **77**, 4668 (1996).
- ⁵³ Y.Y. Lau, *Phys. Rev. Lett.* **87**, 278301 (2001).
- ⁵⁴ A.M. Darr, A.M. Loveless, and A.L. Garner, *Appl. Phys. Lett.* **114**, 014103 (2019).
- ⁵⁵ W.P. Wright and P. Ferrer, *Prog. Aerosp. Sci.* **74**, 48 (2015).
- ⁵⁶ M. Martinez-Sanchez and J.E. Pollard, *J. Propuls. Power* **14**, 688 (1998).
- ⁵⁷ C. Charles, *J. Phys. D: Appl. Phys.* **42**, 163001 (2009).
- ⁵⁸ F. Iza, G.J. Kim, S.M. Lee, J.K. Lee, J.L. Walsh, Y.T. Zhang, and M.G. Kong, *Plasma Process. Polym.* **5**, 322 (2008).
- ⁵⁹ A.L. Garner, A. Caiafa, Y. Jiang, S. Klopman, C. Morton, A.S. Torres, A.M. Loveless, and V.B. Neculaes, *PLoS One* **12**, e0181214 (2017).
- ⁶⁰ J.F. Kolb, S. Kono, and K.H. Schoenbach, *Bioelectromagnetics* **27**, 172 (2006).
- ⁶¹ K.H. Schoenbach, J. Cooper, A. Garner, B. Goan, R.P. Joshi, J. Kolb, S. Katsuki, S. Kono, M. Laroussi, F. Leipold, X. Lu, C. Mallot, J. Quian, and S. Xiao, in *AIP Conf. Proc.* (AIP, 2002), pp. 111–114.
- ⁶² Y.Y. Lau, Y. Liu, and R.K. Parker, *Phys. Plasmas* **1**, 2082 (1994).
- ⁶³ K.L. Jensen, *IEEE Trans. Plasma Sci.* **46**, 1881 (2018).
- ⁶⁴ P. Zhang, Á. Valfells, L.K. Ang, J.W. Luginsland, and Y.Y. Lau, *Appl. Phys. Rev.* **4**, 011304 (2017).
- ⁶⁵ W.W. Tang, D.A. Shiffler, J.R. Harris, K.L. Jensen, K. Golby, M. LaCour, and T. Knowles, *AIP Adv.* **6**, 095007 (2016).
- ⁶⁶ J.R. Harris, K.L. Jensen, and D.A. Shiffler, *AIP Adv.* **5**, 087182 (2015).
- ⁶⁷ J. Lin, P.Y. Wong, P. Yang, Y.Y. Lau, W. Tang, and P. Zhang, *J. Appl. Phys.* **121**, 244301 (2017).

- ⁶⁸ M.A. Bilici, J.R. Haase, C.R. Boyle, D.B. Go, and R.M. Sankaran, *J. Appl. Phys.* **119**, 223301 (2016).
- ⁶⁹ A. Venkattraman and A.A. Alexeenko, *Phys. Plasmas* **19**, 123515 (2012).
- ⁷⁰ L.B. Loeb and J.M. Meek, *Mechanism of Electric Spark* (Stanford Univ. Pres., Stanford, CA, 1941).
- ⁷¹ A.M. Loveless and A.L. Garner, *IEEE Trans. Plasma Sci.* **45**, 574 (2017).
- ⁷² G. Meng, X. Gao, A.M. Loveless, C. Dong, D. Zhang, K. Wang, B. Zhu, Y. Cheng, and A.L. Garner, *Phys. Plasmas* **25**, 082116 (2018).
- ⁷³ D.B. Go and A. Venkattraman, *J. Phys. D. Appl. Phys.* **47**, 503001 (2014).
- ⁷⁴ I. V. Adamovich, M. Nishihara, I. Choi, M. Uddi, and W.R. Lempert, *Phys. Plasmas* **16**, 113505 (2009).
- ⁷⁵ A.M. Loveless, A.M. Darr, R.S. Brayfield II, J.R. Malayter, S.A. Lang, and A.L. Garner, *Trans. Am. Nucl. Soc.* **121**, 399 -401 (2019).
- ⁷⁶ A.M. Darr, C. Darr, and A.L. Garner, *Phys. Rev. Res.* (2020).
- ⁷⁷ S.D. Dynako, A.M. Loveless, and A.L. Garner, *Phys. Plasmas* **25**, 103505 (2018).
- ⁷⁸ S. Bhattacharjee, A. Vartak, and V. Mukherjee, *Appl. Phys. Lett.* **92**, 191503 (2008).
- ⁷⁹ L.K. Ang, T.J.T. Kwan, and Y.Y. Lau, *Phys. Rev. Lett.* **91**, 208303 (2003).
- ⁸⁰ L.K. Ang, Y.Y. Lau, and T.J.T. Kwan, *IEEE Trans. Plasma Sci.* **32**, 410 (2004).
- ⁸¹ L.K. Ang, W.S. Koh, Y.Y. Lau, and T.J.T. Kwan, *Phys. Plasmas* **13**, 056701 (2006).
- ⁸² R.S. Brayfield, A.J. Fairbanks, A.M. Loveless, S. Gao, A. Dhanabal, W. Li, C. Darr, W. Wu, and A.L. Garner, *J. Appl. Phys.* **125**, 203302 (2019).
- ⁸³ Keithley Instruments INC, 1 (2005).
- ⁸⁴ Keithley Instruments INC, *Model 2400 Series SourceMeter*, 2400S-900th- ed. (Cleveland, Ohio 44139, e2002).
- ⁸⁵ N.F. (Nevill F. Mott, *Electronic Processes in Ionic Crystals*, 2d ed. (Clarendon Press, Oxford, 1948).
- ⁸⁶ N. Chintala, A. Bao, G. Lou, and I. V. Adamovich, *Combust. Flame* **144**, 744 (2006).

- ⁸⁷ G. Lou, A. Bao, M. Nishihara, S. Keshav, Y.G. Utkin, J.W. Rich, W.R. Lempert, and I. V. Adamovich, Proc. Combust. Inst. **31 II**, 3327 (2007).
- ⁸⁸ J. Little, K. Takashima, M. Nishihara, I. Adamovich, and M. Samimy, AIAA J. **50**, 350 (2012).
- ⁸⁹ I. V. Adamovich and W.R. Lempert, Plasma Phys. Control. Fusion **57**, 014001 (2015).
- ⁹⁰ A.J. Wallash and L. Levit, Reliab. Testing, Charact. MEMS/MOEMS II **4980**, 87 (2003).
- ⁹¹ A.M. Loveless and A.L. Garner, Appl. Phys. Lett. **108**, 234103 (2016).
- ⁹² J.P. Verboncoeur, M.V. Alves, V. Vahedi, and C.K. Birdsall, J. Comput. Phys. **104**, 321 (1993).
- ⁹³ J.P. Verboncoeur and C.K. Birdsall, (2008).
- ⁹⁴ A.M. Darr and A.L. Garner, Appl. Phys. Lett. **115**, 054101 (2019).

VITA

Russell S. Brayfield II

Education:

Purdue University	West Lafayette, IN 47907
PhD in Agricultural and Biological Engineering Specialization in Plasma and Discharge Physics	Aug. 2020
MS in Nuclear Engineering Specialization in Plasma Diagnostics and Discharge Phenomena	Dec. 2016
BS in Nuclear Engineering (Minor: Mechanical Engineering)	May 2013

Professional Experience:

Air Force Research Lab (AFRL)	May. 2016 to Present
<i>Research Engineer in DOD Pathways Program, supervisor Dr. Michael Brown, Wright-Patterson Air Force Base, Dayton, OH</i>	
<ul style="list-style-type: none">• Designed and conducted ultrafast laser diagnostics combined with simultaneous electrical characterization of photoconductive semiconductor switch evaluation for high frequency pulsed power applications• Fabricated and designed pulsed power supplies to supply kilowatt nanosecond electrical pulses to various experiments• Interacted with Senior Executive Service member, updating them on topic and progress of research efforts within the lab• Defined parameter space for future funding efforts involving ultrafast switching for high power• Guided undergraduate intern efforts supporting various research projects in AFRL• Created computational fluid dynamics model of nanosecond discharge expansion/mixing phenomena to match Rayleigh spectroscopy observations• Developed novel diagnostics for plasma assisted ignition in SCRAMJET applications using Optical Emission, Thompson, and Rayleigh Spectroscopy• Utilized Specair software to analyze spectra obtained to resolve plasma properties• Worked directly with senior research staff to establish and test experimental procedures pertaining to ignition experiments• Evolved methods for spectral analysis using various experimental techniques and software packages	

BioElectrics and ElectroPhysics Laboratory (BEEP)	Aug. 2013 to Present
--	----------------------

Graduate Research Assistant under Dr. Allen Garner, Purdue University West Lafayette, IN

- Adapted modeling codes to study ionization coefficient for plasma breakdown physics study
- Developed nano-scale devices and evaluated using scanning electron microscopy techniques to study electron emission and plasma breakdown physics
- Designed and conducted experiments characterizing microscale and nanoscale plasma discharge devices to better understand plasma breakdown physics and plasma formation
- Developed and implemented novel plasma diagnostic techniques and designed computer simulations for plasma sterilization of produce in joint project between the BEEP Laboratory and Dr. Keener of the Purdue School of Food Science
- Worked with senior faculty in Nuclear Engineering, Aerospace Engineering, and Food Science to develop and test novel technologies and diagnostics
- Mentored and guided 7 undergraduate students and 1 graduate student in their research efforts studying plasma physics phenomena
- Modeling cold atmospheric pressure plasma interactions with lipid bilayers using various Molecular Dynamics codes, including LAMMPS and GROMACS

Dr. Martín Lopez-De-Bertodano's Research Group

May - Aug 2011 and 2012

Undergraduate Research Assistant/Fellow under Dr. Bertodano, Purdue University West Lafayette, IN

- Modeled kinematic waves in vertical two phase flow regimes using Two Fluid Interfacial Temperature (TFIT) code
- Participated in Purdue's Summer Undergraduate Research Fellowship (SURF) program (Summer 2011)
 - Developed proof of concept validation of parallel computer code for linear algebra solvers related to TFIT and investigated current parallel linear algebra solvers such as ScaLAPACK and SPIKE algorithms

Certifications:

Fundamentals of Engineering Exam (FE)

April 2013

- Passed on April 13, 2013
- Indiana State Engineering Intern License #: ET31300396

Refereed Journal Articles:

S. Adams, J. Miles, T. Ombrello, **R. Brayfield**, and J. Lefkowitz, "The effect of inter-pulse coupling on gas temperature in nanosecond-pulsed high-frequency discharges," *Journal of Physics D: Applied Physics* **52(35)**, 355203 (2019).

R. S. Brayfield, II, A. J. Fairbanks, A. M. Loveless, S. Gao, A. Dhanabal, W. Li, C. Darr, W. Wu, and A. L. Garner, "The Impact of Cathode Surface Roughness and Multiple Breakdown Events on Microscale Gas Breakdown at Atmospheric Pressure," *Journal of Applied Physics* **125**, 203302 (2019).

P. Norgard, S. Kovaleski, **R. S. Brayfield, II**, and A. L. Garner, "Non-Equilibrium High Pressure Helium Plasma Produced in the Local Electric Fields of a Piezoelectric Transformer," *IEEE Transactions on Plasma Science* **47**, 128-135 (2019).

R. S. Brayfield II, A. Jassem, M. V. Lauria, A. J. Fairbanks, K. M. Keener, and A. L. Garner, "Characterization of High Voltage Cold Atmospheric Plasma Generation in Sealed Packages as a Function of Container Material and Fill Gas," *Plasma Chemistry and Plasma Processing*, **38**, 379-395 (2018).

Conference Papers:

A. M. Loveless, A. M. Darr, **R. S. Brayfield II**, J. R. Malayter, S. A. Lang, and **A. L. Garner**, “Nanoscale Feature Implications on Electron Emission and Gas Breakdown,” *Trans. Am. Nucl. Soc.* **121**, 399-401 (2019).

Oral Presentations: *Presenter in Italics*

-
- R. S. Brayfield II**, A. M. Darr, W. Li, A. J. Fairbanks, H. Wang, *A. M. Loveless*, and **A. L. Garner**, “Nano/Micro-Meter electrode topology Effects on Electron Emission,” 22nd Annual Directed Energy Science & Technology Symposium, Student Workshop, 11 March 2020, West Point, NY, USA.
- [INVITED] *A. L. Garner*, A. M. Loveless, **R. S. Brayfield II**, A. M. Darr, J. R. Malayter, and G. Meng, “Gas Breakdown and Electron Emission for Microscale Gaps: Unified Theory and Nanofeature Effects,” Joint Meeting of the 32nd International Vacuum Nanoelectronics Conference (IVNC) and 12th International Vacuum Electron Sources Conference (IVESC), Cincinnati, OH, 13.1, 25 July 2019.
- R. Brayfield**, A. Fairbanks, A. Loveless, S. Gao, C. Darr, J. Malayter, W. Wu, and A. Garner, “Microscale Gas Breakdown Voltage Dependence on Electrode Surface,” IEEE Pulsed Power and Plasma Science Conference, 3F3, 25 June 2019.
- R. S. Brayfield II**, A. J. Fairbanks, A. M. Loveless, S. Gao, W. Li, C. Darr, J. R. Malayter, W. Wu, and A. L. Garner, “Experimental assessment of electrode effects on gas breakdown for microscale gaps,” 21st Annual Directed Energy Science & Technology Symposium, Student Workshop II, 10 April 2019, Destin, FL, USA.
- [INVITED] *A. L. Garner*, A. M. Loveless, **R. S. Brayfield II**, A. J. Fairbanks, S. D. Dyanko, S. Gao, W. Wu, R. S. Bean, and G. Meng, “Gas Breakdown at Microscale and Smaller Gaps: Theoretical Unification of Mechanisms and Experimental Assessment of Surface Roughness,” iPlasmaNanoIX, New Buffalo, MI, 27 August 2018.
- A. Fairbanks*, A. Darr, A. Vadlamani, **R. Brayfield II**, and A. Garner, “Real-time Conductivity Measurements of Mammalian Cell Suspension during Nanosecond Electric Pulse Trains,” 2018 IEEE International Power Modulator and High Voltage Conference, 04 June 2018, Jackson Lake Lodge, WY, USA, Oral 2O-1 (2018).
- A. L. Garner*, **R. S. Brayfield II**, A. J. Fairbanks, A. M. Loveless, S. Gao, R. S. Bean, Y. Xuan, and W. Wu, “Microscale Gas Breakdown and Implications to Electron Emission,” 20th Annual Directed Energy Science & Technology Symposium, High Power Microwave (HPM) Technologies, 01 March 2018, Oxnard, CA, USA.
- R. S. Brayfield II**, A. J. Fairbanks, and **A. L. Garner**, “Plasma Species Variation as a Function of Voltage for High Voltage Cold Atmospheric Pressure Plasmas in Sealed Bags,” 2017 IEEE International Conference on Plasma Sciences, Oral TU 2.5-2, 23 May 2017, Atlantic City, NJ USA.
- M. V. Lauria*, **R. S. Brayfield II**, R. G. Johnson, and A. L. Garner, “Cold Atmospheric Pressure Plasmas for Food Applications,” The Summer Undergraduate Research Fellowship (SURF) Symposium, 04 August 2016, West Lafayette, IN, AO-17, no. 11 (2016).
- R. S. Brayfield II**, A. Jasse, M. Lauria, A. J. Fairbanks, *A. L. Garner*, and K. M. Keener, “Optical Emission Spectroscopy of High Voltage, Cold Atmospheric Pressure Plasmas,” 2016 IEEE International Conference on Plasma Sciences, Oral 3E-2, 21 June 2016, Banff, Alberta, Canada.
- R. S. Brayfield II**, “Implementation and Validation of Parallel Direct Solvers for Linear Algebraic Equations Related to Nuclear Systems Simulation” Presentation and Proceedings Paper at Summer Undergraduate Research Fellowship (SURF) Symposium, West Lafayette, IN, August 2011

Teaching Experience:

Teaching Assistant Spring 2016, Spring 2015, Spring 2014
Graduate Teaching Assistant for NUCL 205 (Nuclear Instrumentation Laboratory I) and 504 (Graduate Nuclear Instrumentation Laboratory)

- Instructed lab course two to three times a week and organized course materials and lab space. Held office hours every week to assist graduate and undergraduate students

Course Grader Fall 2015, Fall 2013
Grader for NUCL 305(Nuclear Instrumentation Laboratory II)

- Graded lab reports for NUCL 305 course and coordinated grading criteria with head grader to ensure consistency. Held office hours every week to assist undergraduate students

Teaching Assistant Fall 2014
Graduate Teaching Assistant for NUCL 305 (Nuclear Instrumentation Laboratory II)

- Taught NUCL 305 lab course two to three times a week and organized course materials and lab space. Held office hours every week to assist undergraduate students

Awards and Honors:

Award for exceptional performance from AFRL RQHF Summer 2019

- Awarded for successfully completing tasks given constraints of laser availability.

Student Travel Award - IPMHVC 2018 Conference in Jackson Hole, Wyoming June 2018

- Awarded a travel grant for the annual Power Modulator and High Voltage Conference

Best Poster (Second place) - BIOEM2015 Conference in Asilomar California June 2015

- Awarded for the annual Bioelectromagnetics Society meeting based off of judging conducted during poster sessions by senior society members

Student Travel Award - BIOEM2015 Conference in Asilomar California June 2015

- Awarded a travel grant for the annual Bioelectromagnetics Society meeting based off abstract selection for paper session

Purdue University Teaching Academy Graduate Teaching Award May 2015

- Recognized for commendable dedication to students and the material taught for the Undergraduate curriculum

Professional Organizations:

IEEE Nuclear and Plasma Science Society 2014-present
Student Member

American Nuclear Society Student Affiliate 2010-2013
Sub-Committee chair 2012

- Oversaw efforts of assembling Glasstone award materials and completion of the application

General Member 2010, 2011, and 2013

- Directed Nuke Week activities and clean up
- Presented Nuclear Engineering related lessons to high school students

Relevant Skills:

- Plasma diagnostics using optical emission and absorption spectroscopy using ICCD and CCD spectroscopy equipment
- High speed imaging
- ICCD imaging
- High voltage safety training
- Purdue Radiation Training (open/sealed sources and emergency response)
- Molecular dynamics modeling experience using LAMMPS, GROMACS, and PuReMD
- Modeled various parts and assemblies using CATIA workbenches